UNIVERSITY OF SOUTHAMPTON

FACULTY OF PHYSICAL SCIENCES AND ENGINEERING

Optoelectronics Research Centre

Silicon photonic modulators for the mid-infrared

by

Milos Nedeljkovic

Thesis for the degree of Doctor of Philosophy

December 2013

UNIVERSITY OF SOUTHAMPTON

ABSTRACT

FACULTY OF PHYSICAL SCIENCES AND ENGINEERING

Optoelectronics Research Centre

Doctor of Philosophy

SILICON PHOTONIC MODULATORS FOR THE MID-INFRARED

by Milos Nedeljkovic

Mid-infrared group-IV material photonics is an emerging field, which aims to migrate techniques used for near-infrared silicon photonics to longer wavelengths, and to address applications in areas such as environmental and bio-chemical sensing, homeland security, telecommunications, medicine or astronomy.

In order to create mid-infrared photonic systems, components such as waveguides, splitters/couplers, filters, interferometers and modulators are required. Silicon-on-insulator (SOI) waveguides, which are used in the near-infrared, have high absorption at wavelengths greater than 4μm, and therefore new material platforms will be required for some parts of the mid-infrared.

In this project silicon-on-insulator waveguides operating at 3.8μm have been demonstrated with losses as low as 2.0dB/cm. Poly-Si on SOI waveguides, which can be fabricated in a commercial foundry, and germanium on silicon waveguides, which could be used throughout most of the mid-infrared, were also demonstrated at 3.8μm.

The passive components required to make a modulator in the SOI material platform were designed, fabricated and characterised. SOI MMIs were demonstrated at 3.8μm with insertion losses as low as 0.10±0.01dB, which is comparable to the best achieved near-IR silicon photonic MMI performance, and Mach-Zehnder interferometers were measured to have insertion losses of 1.3-2.2dB, and extinction ratios of up to 28dB.

These components were used to create thermo-optic modulators in SOI, which are the first group-IV waveguide integrated modulators at wavelengths above 3μm. Switching powers as low as 47mW, and a -3dB bandwidth of 23.8kHz, were achieved.

In order to build faster modulators, the free-carrier plasma dispersion effect could be employed. However, accurate equations for prediction of this effect in the mid-infrared have not been available until now. A semi-empirical approach has been used to calculate design equations relating the change in absorption coefficient and change in refractive index to change in charge carrier concentration in silicon for wavelengths in the 1.3-14μm wavelength range.

Acknowledgements

This project would not have been possible without the help of many of others. I am deeply grateful to Dr. Goran Mashanovich for his kind and friendly guidance, teaching and tireless work throughout the last few years, and to Professor Graham Reed, who has been an ideal source of advice and support whenever I have needed it. Dr. Frederic Gardes and Dr. David Thomson have patiently tolerated my endless questioning for many years, thank you for helping me with your expertise. Dr. Milan Milošević was responsible for a large part of my introduction to this field, and spent many hours and days training me in everything from simulation to polishing, and I am grateful to him for both his time and friendship. All of the other members of the Silicon Photonics group have helped me on countless occasions. Jordi Soler Penades, Dr. Xia Chen, Dr. Youfang Hu, Rob Topley, Paul Thomas, Callum Littlejohns, Scott Reynolds, Dr. Stevan Stanković, Dr. Ali Khokhar, Dr. Colin Mitchell, Dr. Renzo Loiacono, Nathan Owens and Arifa Ahmed have all helped me with things both little and large, and have made these last few years more enjoyable than I could possibly have expected. In particular I am thankful to Stevan, Ali, Colin, Scott, Callum and Jordi for the time that they spent helping me with sample fabrication and preparation.

Many of the results in this project are a result of collaborations with colleagues from other universities. I have enjoyed working with Dr. Richard Soref of the University of Massachusetts greatly, and always look forward to reading his emails, which are endlessly brimming with new ideas. The chapter on silicon free carrier absorption would not have been possible without his input. I would like to extend my thanks to Professor Gunther Roelkens, Aditya Malik and Muhammad Muneeb from the University of Gent, whose work has resulted in the Ge-on-Si waveguide and poly-Si on SOI waveguide results. I am indebted to Dr. Marc Sorel and Dr. Michael Strain for their fabrication of samples at the University of Glasgow.

A little over halfway through this project I moved, along with the rest of the group, from the University of Surrey to the University of Southampton. We were greeted with

warmth by both the staff and students, thank you for making us so welcome. I would like to thank the administrative and technical staff from both Surrey and Southampton, without whom nothing would get done.

I am grateful to the EPSRC, who have provided me with the studentship that has allowed me to pursue my work.

Above all, I would like to thank my parents Jovan and Ljiljana, my brother Nebojša, and my grandparents Baša i Ceka for their unending love and support.

Academic Thesis: Declaration Of Authorship

I, MILOS NEDELJKOVIC
declare that this thesis and the work presented in it are my own and has been generated by me as the result of my own original research.

SILICON PHOTONIC MODULATORS FOR THE MID-INFRARED

I confirm that:

1. This work was done wholly or mainly while in candidature for a research degree at this University;

2. Where any part of this thesis has previously been submitted for a degree or any other qualification at this University or any other institution, this has been clearly stated;

3. Where I have consulted the published work of others, this is always clearly attributed;

4. Where I have quoted from the work of others, the source is always given. With the exception of such quotations, this thesis is entirely my own work;

5. I have acknowledged all main sources of help;

6. Where the thesis is based on work done by myself jointly with others, I have made clear exactly what was done by others and what I have contributed myself;

7. Either none of this work has been published before submission, or parts of this work have been published as:

Journal Papers

1. Roelkens, et al. ""Silicon-based photonic integration beyond the telecommunication wavelength range," IEEE Photonics Society (IPS) Journal of Selected Topics in Quantum Electronics, (invited, accepted).
2. D-X. Xu, J. Schmid, G. T. Reed, G. Z. Mashanovich, D. J. Thomson, **M. Nedeljkovic**, X. Chen, D. Van Thourhout and S. Keyvaninia, "Silicon photonic integration platform – Have we found the sweet spot?," Journal of Selected Topics in Quantum Electronics, vol. 24, no. 4 (2013).
3. **M. Nedeljkovic**, A. Z. Khokhar, Y. Hu, X. Chan, J. Soler Penades, S. Stankovic, D. J. Thomson, F. Y. Gardes, H. M. H. Chong, G. T. Reed, and G. Z. Mashanovich, "Silicon photonic devices and platforms for the mid-infrared" *Optical Materials Express*, vol. 3, pp. 1205–1214, 2013.
4. G. Roelkens, U. Dave, A. Gassenq, N. Hattasan, C. Hu, B. Kuyken, F. Leo, A. Malik, M. Muneeb, E. Ryckeboer, Z. Hens, R. Baets, Y. Shimura, F. Gencarelli, B. Vincent, R. Loo, J. Van Campenhout, L. Cerutti, J.-B. Rodriguez, E. Tournié, X. Chen, **M. Nedeljkovic**, G. Z. Mashanovich, S. Li, N. Healy, A. C. Peacock, X. Liu, R. Osgood, and W. J. Green, "Silicon-based heterogeneous photonic integrated circuits for the mid-infrared," *Optical Materials Express*, vol. 3, 1523-1536 (2013).
5. G. T. Reed, G. Z. Mashanovich, F. Y. Gardes, **M. Nedeljkovic**, D. J. Thomson, L. Ke, P. Wilson, S-W. Chen and S. H. Hsu, "Recent breakthroughs in carrier depletion based silicon optical modulators," *Nanophotonics*, vol. 16 (2013).
6. D. J. Thomson, F. Y. Gardes, S. Liu, H. Porte, L. Zimmermann, J-M Fedeli, Y. Hu, **M. Nedeljkovic**, X. Yang, P. Petropoulos, and G. Z. Mashanovich, "High performance Mach Zehnder based silicon optical modulators," *IEEE J. Sel. Top. Quantum Electron.*, vol. 19, 3400510, 2013.
7. M. Muneeb, X. Chen, P. Verheyen, S. Pathak, A. Malik, **M. Nedeljkovic**, J. Van Campenhout, G. Z. Mashanovich, and G. Roelkens, "Demonstration of silicon-on-insulator mid-infrared spectrometers operating at 3.8μm," *Optics Express*, vol. 21, pp. 11659–11669, 2013.

8. E. Jaberansary, T. B. Masaud, M. M. Milosevic, **M. Nedeljkovic**, G. Z. Mashanovich, and H. M. H Chong, "Scattering loss estimation using 2D Fourier analysis approach to model 3D roughness on optical waveguide sidewalls," *IEEE Photonics J.,* vol. 5, p. 6601010, 2013.
9. C. Reimer, **M. Nedeljkovic**, D. J. M. Stothard, M. O. S. Esnault, C. Reardon, L. O'Faolain, M. Dunn, G. Z. Mashanovich, and T. F. Krauss, "Mid-infrared photonic crystal waveguides in SOI," *Opt. Exp.,* vol. 20 (28), pp. 29361-29368, 2012.
10. M. M. Milosevic**, M. Nedeljkovic**, T.-B. Masaud, E. Jaberansary, H. M. H. Chong, N. G. Emerson, G. T. Reed, and G. Z. Mashanovich, "Silicon waveguides and devices for the mid-infrared," *Appl. Phys. Lett.*, vol. 101, 121105, 2012.
11. **M. Nedeljkovic**, R. Soref, and G. Z. Mashanovich, "Free-carrier electro-refraction and electro-absorption modulation predictions for silicon over the 1-14μm wavelength range," *IEEE Photonics J.,* vol. 3, pp. 1171-1180, 2011.
12. G. Z. Mashanovich, M. M. Milosevic, **M. Nedeljkovic**, N. Owens, B. Xiong, E.-J. Teo, and Y. Hu, "Low loss silicon waveguides for the mid-infrared," *Opt. Express*, vol. 19, pp. 7112-7119, 2011.

Invited Papers

1. **M. Nedeljkovic**, Y. Hu, A. Khokhar, X. Chen, J. Soler Penades, S. Stankovic, C. Mitchell, G. Z. Mashanovich, "Mid-infrared silicon photonic devices for sensing applications," *5th EOS Topical Meeting on Optical Microsystems*, Capri, Italy, 12-14 September 2013.
2. G. Z. Mashanovich**, M. Nedeljkovic**, X. Chen, J. Soler Penades, G. Madalinski, M. Muneeb, G. Roelkens, H. M. H. Chong, G. T. Reed, "Group IV photonics platforms for sensing applications," PIERS 2013, Stockholm, Sweden, 12-15 August 2013.
3. G. Roelkens, B. Kuyken, F. Leo, N. Hattasan, E. Ryckeboer, M. Muneeb, C. Hu, A. Malik, Z. Hens, R. Baets, Y. Shimura, F. Gencarelli, B. Vincent, R. Loo, P. Verheyen, G. Lepage, J. Van Campenhout, L. Cerutti, J.B. Rodriguez, E. Tournié, X. Chen, **M. Nedeljkovic**, G. Z. Mashanovich, X. Liu, R. Osgood, W. M. J. Green, "Long-wavelength III-V/silicon photonic integrated circuits," *Integrated Photonics Research, Silicon and Nano-Photonics (IPR)*, Rio Grande, Puerto Rico, 14-19 July 2013
4. G. Z. Mashanovich, **M. Nedeljkovic**, X. Chen, T. M. Ben Masaud, M. Muneeb, M. Strain, M. Sorel, T. F. Krauss, G. C. Roelkens, A. C. Peacock, H. M. H. Chong, G. T. Reed, "Group IV platforms for the mid-infrared," SPIE Optics + Optoelectronics, Prague, Czech Republic, 15-18 April 2013.
5. G. Z. Mashanovich, **M. Nedeljkovic**, M. M. Milosevic, Y. Hu, T. M. Ben Masaud, E. Jaberansary, X. Chen, M. Strain, M. Sorel, A. C. Peacock, H. M. H. Chong, G. T. Reed, "Mid-infrared photonics devices in SOI," *SPIE Photonics West*, San Francisco, USA, 2-7 February 2013.
6. G. Z. Mashanovich, **M. Nedeljkovic**, M. M. Milosevic, Y. Hu, T. M. Ben Masaud, E. Jaberansary, X. Chen, M. Strain, M. Sorel, A. C. Peacock, T. F. Krauss, H. M. H. Chong, G. T. Reed, "Mid-infrared silicon photonics devices," *Photonics Global Conference 2012*, Singapore, 13-16 December 2012.
7. G. Z. Mashanovich, **M. Nedeljkovic**, M. M. Milosevic, Y. Hu, F. Y. Gardes, D. J. Thomson, T.-B. Masaud, E. Jaberansary, H. M. H. Chong, R. Soref, G. T. Reed, "Group IV photonic devices for the mid-infrared," *SPIE Photonics Europe*, Brussels, Belgium, 16-19 April 2012.
8. G. Z. Mashanovich, M. M. Milosevic, **M. Nedeljkovic**, D. Cox , V. M. N. Passaro, H. M. H. Chong, and R. Soref, "Mid-infrared silicon photonics for sensing applications," *2012 MRS Spring Meeting*, San Francisco, 9-13 April 2012.
9. G. Z. Mashanovich, M. M. Milosevic, **M. Nedeljkovic**, N. Owens, W. R. Headley, E. J. Teo, B. Xiong, P. Yang, and Y. Hu, "Mid-infrared silicon photonic devices," *Proc. SPIE*, vol. 7943, 79430Q, 2011.
10. G. Z. Mashanovich, W. Headley, M. Milosevic, N. Owens, E. J. Teo, B. Q. Xiong, P. Y. Yang, **M. Nedeljkovi**c, J. Anquita, I. Marko, and Y. Hu, "Waveguides for mid-IR group IV photonics," in Proc. *7th IEEE Group IV Photonics Conference*, Beijing, China, 1-3 September 2010, paper FD1.

Conference Papers

1. **M. Nedeljkovic**, M. M. Milošević , T. M. Ben Masaud, E. Jaberansary, C. Reimer, D. J. M. Stothard, T. F. Krauss, H. M. H. Chong, G. T. Reed, G. Z. Mashanovich, "SOI mid-infrared silicon photonics for the 3-4 um wavelength range," *OSA 96th Annual Meeting Frontiers in Optics 2012*, Rochester, New York, USA, 14-18 October 2012.
2. **M. Nedeljkovic**, M. M. Milosevic, T. M. Ben Masaud, E. Jaberansary, H. M. H. Chong, G. T. Reed, G. Z. Mashanovich, "Silicon devices for the 3-4 um wavelength range," *EOS Annual Meeting 2012*, Aberdeen, UK, 25-28 September 2012.
3. **M. Nedeljkovic**, M. M. Milosevic, D. J. Thomson, Y. Hu, F. Y. Gardes, T.-B. Masaud, E. Jaberansary, H. M. H. Chong, D. Cox, R. Soref, N. G. Emerson, G. T. Reed, and **G. Z. Mashanovich**, "Group IV photonic devices and modulation predictions for mid-infrared applications," *Photon 12*, Durham, UK, 3-6 September 2012.
4. C. Reimer, **M. Nedeljkovic**, D. J. M. Stothard, G. Z. Mashanovich, and T. F. Krauss, "Mid-infrared photonic crystal waveguides in SOI," *Group IV Photonics*, San Diego, CA, USA, 29-31 August 2012.
5. M. M. Milošević , **M. Nedeljkovic**, T. M. B. Masaud, E. Jaberansary, H. M. H. Chong, G. T. Reed, and G. Z. Mashanovich, "Submicron silicon waveguides and optical splitters for mid-infrared applications," *Group IV Photonics*, San Diego, CA, USA, 29-31 August 2012.
6. D. J. Thomson, M. Milosevic, D. C. Cox, F. Y. Gardes, **M. Nedeljkovic**, J.-M. Fedeli, G. Z. Mashanovich, and G. T. Reed, "Focused ion beam processing of active and passive silicon photonic devices," *ECIO 2012*, Barcelona, Spain, 16-20 April 2012.
7. **M. Nedeljkovic**, R. A. Soref, G. Z. Mashanovich, "Free-carrier electro-absorption and electro-refraction modulation in group IV materials at mid-infrared wavelengths" *SPIE Photonics West 2012*, San Francisco, USA, 21-26 January 2012.

Signed:
……

Date: 19/12/13

Table of contents

Abstract i
Acknowledgements iii
Declaration of authorship v
Table of contents ix
List of figures xiii

Chapter 1: Introduction **1**
1.1. Silicon Photonics 1
1.2. Mid-infrared photonics research and its applications 2
1.3. Group-IV materials as platforms for mid-IR integrated photonics 3
1.4. Thesis outline 4

Chapter 2: Literature review **7**
2.1. Non group-IV integrated optics 7
2.2. Waveguides 7
2.2.1. Planar optical waveguides 8
2.2.2. Waveguides in NIR silicon photonics 10
2.2.3. Candidate material platforms for group-IV mid-infrared photonics 12
2.3. Passive photonic components 18
2.3.1. Waveguide bends 18
2.3.2. Multimode interferometers 19
2.3.3. Mach-Zehnder interferometers 20
2.4. Modulators 22
2.4.1. Electro-optical modulation mechanisms in semiconductors 23
2.4.2. Mid-infrared modulators in literature 24
2.4.3. Silicon modulators device structures 25
2.5. Free-carrier absorption in silicon 28
2.5.1. Classical free-carrier absorption theory 29
2.5.2. Intersubband free-carrier absorption 30
2.5.3. Soref and Bennett approach for prediction of electroabsorption and electrorefraction in silicon 31
2.6. Literature review summary 33

Chapter 3: Literature review **35**
3.1. Basic operation 35
3.2. Equipment details 38
3.2.1. Quantum cascade laser 38
3.2.2. Detector 39
3.2.3. Optical fibres and fibre preparation 40
3.2.4. Polarization control 40
3.2.5. Signal processing 41

Chapter 4: Mid-IR waveguides **43**
4.1. Waveguide propagation loss measurements 43
4.2. Simulation methods 44
4.2.1. RSoft Beamprop 44
4.2.2. Photon Design Fimmwave 45
4.3. Silicon-on-insulator waveguides 45
4.3.1. Design 46
4.3.1.1. Waveguide height 46
4.3.1.2. Etch depth 48
4.3.1.3. Waveguide width 48
4.3.1.4. Mask design 51
4.3.2. Fabrication 51
4.3.3. Characterisation 56
4.4. Poly-Si on SOI waveguides 61
4.4.1. *imec* Advanced Passives fabrication process 62
4.4.2. Design of *imec* Advanced Passives waveguides 63
4.4.3. *imec* Advanced Passives waveguides experimental results 65
4.5. Germanium-on-silicon waveguides 66
4.5.1. Ge-on-Si waveguide design and fabrication 66
4.5.2. Ge-on-Si waveguide experimental characterisation 68
4.6. Mid-infrared waveguides summary 70

Chapter 5: Passive components for MIR modulation **73**
5.1. Multimode interferometers 73
5.1.1. MMI design 73
5.1.2. MMI fabrication and characterisation 76
5.2. Mach-Zehnder interferometers 78

5.2.1. MZI design 79
5.2.2. Straight-arm MZI fabrication and characterisation 83
5.2.3. Spiral-arm MZI fabrication and characterisation 85
5.3. Summary 88

Chapter 6: Silicon thermo-optic modulators for the MIR 91
6.1. MIR thermo-optic modulator design 91
6.2. Fabrication 95
6.3. Electrical characterisation equipment 96
6.4. Electrical characterisation results 97
6.5. Summary 102

Chapter 7: The plasma dispersion effect in silicon 105
7.1. The Soref and Bennett equations 106
7.2. Extending the Soref and Bennett equations into the MIR 110
7.3. Discussion: implications for MIR modulators 119

Chapter 8: Conclusions and future work 121

Appendix 131

References 133
Chapter 1 133
Chapter 2 134
Chapter 3 139
Chapter 4 139
Chapter 5 141
Chapter 6 142
Chapter 7 142
Chapter 8 143

List of figures

Fig. 1.1 Reproduced from [13]. Silicon longwave integrated chip for sensing, with spectrally broad source, and two banks of longwave sensors for detection of discrete portions of the spectrum. 4

Fig. 1.2. Reproduced from [13]. Waveguided Fourier Transform Infrared Spectrometer (FTIR), with on-chip CMOS computer. 5

Fig. 2.1. Simple planar waveguide geometry. Diagram reproduced from ref. [5]. 8

Fig. 2.2. Diagrams of silicon-on-insulator a) rib waveguide and b) strip waveguide, with overlays of typical simulated fundamental mode profiles....10

Fig. 2.3. Absorption spectra of silicon and silicon dioxide for λ=1-10μm, SiO2 data digitised from ref. [10] Si data digitised from ref. [11] and [12]. 12

Fig. 2.4. Approximate transparency windows in the 1-14μm range for some of the group-IV material MIR platforms suggested by Soref [10]. Transparency is defined here as loss <1dB/cm, and limits for the ranges are from [10]. For Ge-on-Si and GeSn-on-Si the transparency ranges extend to longer wavelengths. All transparency range values are given in table 1 of appendix 1. 13

Fig. 2.5. Intensity plot of the field in the multi-mode section of an MMI. Red areas indicate high intensity, blue indicates low intensity.. The positions of the single-fold, two-fold, and three-fold self-imaging locations have been labelled.. 19

Fig. 2.6. Diagrams of common 1 x 2 splitter/coupler structures: a) Y-splitter, b) directional coupler, c) multi-mode interferometer with tapered input and output ports. 20

Fig. 2.7. Asymmetric 1 x 1 Mach Zehnder interferometer. 21

Fig. 2.8. Spectrum of thermo-optic coefficient of silicon at 300°K, for λ=1.1-5.5μm, plotted data from ref. [42]. 24

Fig. 2.9. Schematic cross-sections of typical silicon modulators based on the plasma dispersion effect [39]. a) Carrier accumulation modulator. b) Carrier injection modulator. c) Carrier depletion modulator. 26

Fig. 2.10. Cross-section of self-aligned carrier depletion phase shifter, reproduced from [54]..27

Fig. 2.11. Band energy diagram showing intravalley free-carrier absorption. 29

Fig. 2.12. Example absorption coefficient spectra of heavily doped Si and Ge, digitised from literature. a) p-type Ge [59]. The marked features labelled A, B and C are due to direct intervalence band transitions. b) n-type Si [60]. The feature labelled A is due to interconduction band transitions of electrons. 30

Fig. 2.13. Intersubband free-carrier absorption mechanisms. a) Indirect intervalley free-carrier absorption, e.g. from the L-valley to the Γ-valley of the Ge conduction band. b) Direct intervalence band absorption. The numbered processes show photon-assisted transitions of carriers between: 1. Heavy Hole -> Light-Hole 2. Heavy-Hole -> Split-off band 3. Light-Hole-> Split-off band. 31

Fig. 2.14. Absorption spectra of doped silicon wafers reproduced from [41] for a) n-type Si, b) p-type Si. The wavelength is plotted on the horizontal axis in terms of photon energy (eV), and the vertical axis shows the absorption coefficient, α (cm^{-1}). Each figure shows a number of curves for different doping concentrations..... 33

Fig. 3.1. Block diagram of MIR optical characterisation setup, when configured for butt coupling. 35

Fig. 3.2. Block diagram of MIR optical characterisation setup, when configured for grating coupling. 36

Fig. 3.3. Labelled photograph of butt coupling alignment apparatus. 37

Fig. 3.4. Labelled photograph of grating coupler alignment apparatus. 38

Fig. 3.5. QCL output power plotted against emission wavelength, data provided by Daylight Solutions. 39

Fig. 3.6. InSb detector detectivity spectrum, reproduced from [4]. 39

Fig. 4.1. Diagram showing top view of the waveguide layout used for measurement of waveguide loss using the cut-back method. The waveguide length is varied while all other sources of loss are kept constant..... 43

Fig. 4.2. Diagram of SOI waveguide cross-section, showing dimensions to be optimised..... 46

Fig. 4.3. Single mode condition widths for SOI waveguides with different Si layer thicknesses at wavelengths between 1.5μm and 4.0μm. a) TE polarisation b) TM polarisation. 47

Fig. 4.4. Beamprop mode simulation for SOI waveguides with H=400nm, HBOX=2000nm, and in a) D=350nm, and b) D=220nm. The figures show the widths at which the 1st higher order mode (red points) can propagate. 49

Fig. 4.5. Fimmwave mode simulations for SOI waveguides with H=400nm, D=220nm and HBOX=2000nm at λ=3.8μm. a) Waveguide width vs. propagation loss, showing loss from material absorption only (red circles) and material absorption and substrate leakage (black squares). b) Total propagation loss vs. BOX thickness. 50

Fig. 4.6. Photograph of chip ready for polishing and dummy chip mounted onto chip holder and mounting block..... 54

Fig. 4.7. Chip mounted in polishing machine. 55

Fig. 4.8. Red line shows an example of an SOI waveguide spectrum measured using the QCL centered at λ=3.80μm. The black line is an order 10 polynomial that has been fitted to the experimental curve in order to filter out the high frequency components. 57

Fig. 4.9. Propagation loss measurement for SOI rib waveguide sample “SOI_A”, with H=400nm, D=350nm, W=1100nm and HBOX=2000nm. The measured propagation loss is 10.5dB/cm. 58

Fig. 4.10. Experimental propagation loss plotted against waveguide width for SOI waveguides with H=400nm and D=220nm. 59

Fig. 4.11. Cut-back loss measurement for SOI rib waveguides with H=400nm, D=220nm, W=1350nm, and H_{BOX}=2000nm. Propagation loss for chip 5 = 1.45dB/cm. 60

Fig. 4.12. Schematic diagrams of imec AP waveguide stack with a) 160nm etch into stack, b) 380nm etch into stack, and c) 220nm etch into stack. 63

Fig. 4.13. Beamprop simulation of effective indices of fundamental and 1st higher order TE modes. 1st higher order mode is found for W≥1.325µm. 64

Fig. 4.14. Cut-back loss measurement for imecAP waveguides. Measured propagation loss is 7.5dB/cm, with r^2=0.987 for the fit. 65

Fig. 4.15. SEM image of Ge-on-Si waveguide cross-section, reproduced from [23]. 67

Fig. 4.16. Ge-on-Si waveguide cut-back propagation loss measurements for λ=3.77µm, with varying waveguide dimensions. a-b): H=1µm strip waveguides, c): H=1µm rib waveguides, d-f): H=2µm rib waveguides. 68

Fig. 4.17. Propagation loss of Ge-on-Si waveguides with H=2µm and D=1.4µm plotted as a function of waveguide width. 69

Fig. 5.1. Photon Design Fimmprop simulated intensity profile of 1×2 MMI with tapered input and output ports. Red=high intensity, blue=low intensity. For modelling the device is split into five sections, which have been marked in the figure: 1. Input waveguide, 2. Input taper, 3. Multimode waveguide, 4. Output tapers, 5. Output waveguides. 74

Fig. 5.2. Insertion loss of 1×2 tapered MMI simulated using Photon Design Fimmprop, with W_{MMI}=8µm, S=4.18µm, L=21µm, and varying taper width, W_{tap}. 75

Fig. 5.3 Normalised transmission measurement of SOI MMI’s with H=400nm and D=220nm, at λ=3.8µm. The graph shows the normalized loss through different numbers of successive pairs of MMIs. The gradient of the line for best fit gives the insertion loss per MMI. 77

Fig. 5.4. Labelled SEM image of a 1×2 MMI fabricated by e-beam lithography at the University of Glasgow, based on SOI wafers with H=400nm and D=350nm. 77

Fig. 5.5. Insertion loss measurements of MMIsoi_B waveguides. Measured insertion loss is 0.25±0.02dB per MMI. The normalized transmission though each MMI chain is plotted against the number of MMIs. 78

Fig. 5.6. Labelled schematic diagram of asymmetric 1×1 Mach-Zehnder interferometer with MMI splitter and coupler. 79

Fig. 5.7. Free spectral range as a function of MZI arm length difference for an SOI waveguide with W=1300nm, H=400nm, D=220nm, and H_{BOX} =2000nm, calculated using eq. 5.9 and a simulated group index value for λ=3.77µm. 81

Fig. 5.8. Labelled diagram of a spiral waveguide, which is integrated into each arm of the spiral-arm MZI. 81

Fig. 5.9. Fimmwave simulated mode profiles of bent SOI waveguides with W=1300nm, H=400nm, D=220nm and H_{BOX}=2µm, with bend radii of a) 5µm, b) 10µm and c) 15µm. 82

Fig. 5.10. Simulated propagation loss (dB/cm) of a bending SOI waveguide, as a function of bend radius, at λ=3.8µm. The simulated waveguide had dimensions H=400nm, D=220m, W=1300nm and H_{BOX}=2µm. 82

Fig. 5.11. Cross-section of the optical mode electric field intensity parallel to the wafer. Mode profile simulated using Fimmwave. The centre of the waveguide is at the horizontal position of 2.5µm 83

Fig. 5.12. Normalized transmission through MZIsoi_A type device with 350 µm arm length difference. 84

Fig. 5.13. Experimentally measured FSR values (black squares) plotted against MZI arm length difference for MZIsoi_A type devices. The red line shows a fit of the group index to the data with eq. 5.9 (n_g=4.20), while the black line shows the predicted FSR from the simulated group index (n_g=4.03). 85

Fig. 5.14. Optical microscope image of an asymmetric spiral-arm MZI, based on SOI waveguides. 86

Fig. 5.15. Normalised transmission of asymmetric spiral-arm MZI with two spiral loops in the shorter arm and three loops in the longer arm, and W_{gap}=4µm, R_0=27.5µm, W=1.3µm. 86

Fig. 5.16. Average length of spirals with the same number of loops plotted against their average insertion loss 87

Fig. 5.17. Normalised insertion loss for different numbers of linked 90° bends of R=30µm, for SOI waveguides with H=400nm, D=220nm, HBOX=2µm, and W=1300nm. 88

Fig. 6.1. Labelled schematic cross-section diagram of thermo-optic phase shifters, with metal heaters a) directly above waveguide, and b) separated laterally from waveguide. 92

Fig. 6.2. Fimmwave simulation results showing optical absorption of devices with metal strips placed directly above the waveguides (red dots) and placed adjacent to the waveguides (black squares), with a 1µm edge to edge separation between the waveguide and metal strip. The metal strip is 100nm thick, and extends to the edge of the simulation region for both configurations. 93

Fig. 6.3. Example mask design of a spiral arm MZI, with a metal strip folded above the waveguide spiral acting as a heater. 94

Fig. 6.4. Normalised optical transmission through an asymmetric spiral arm thermo-optic modulator, plotted (black squares) against the applied DC power (W). In this case the heated spiral is 1.77mm long and the arm length difference is 96.1µm. The red curve curve shows the fitted theoretical response of an asymmetric MZI with an applied phase shift. a) Linear y-axis scale, b) transmission plotted in decibels. 98

Fig. 6.5. Switching power of straight arm MZIs (black squares) and of spiral arm MZIs with R_1=20µm (red circles) and with R_1=27.5µm (blue triangles), plotted for varying heated waveguide length. The spirals have between one (shortest) and six loops (longest). 99

Fig. 6.7. The switching power of spiral-arm MZI thermo-optic modulators with varying inner bend radius. All four devices have the same number of spiral loops, waveguide width and gap between waveguides. 101

Fig. 6.8. Normalised optical transmission for a straight-arm MZI, with a 2.25mm heater length and 10µm heater width, when an AC signal of varying frequency is applied to it. 102

Fig. 7.1. Optical absorption spectra of doped silicon with different concentrations of a) n-type and b) p-type doping. 108

Fig. 7.2. Variable names used in the numerical Kramers-Kronig integration. 110

Fig. 7.3. Change in absorption coefficient, Δα (cm-1), for different electron concentrations in the 1.3-14µm wavelength range. 111

Fig. 7.4. Change in absorption coefficient, Δα (cm-1), for different hole concentrations in the 1.3-14µm wavelength range. 111

Fig. 7.5. Change in refractive index, -Δn, for different electron concentrations in the 1.3-14µm wavelength range. 112

Fig. 7.6. Change in refractive index, -Δn, for different hole concentrations in the 1.3-14µm wavelength range. 112

Fig. 7.7. Absorption coefficient in silicon plotted as a function of electron concentration for a) λ=2µm, b) λ=7.5µm and c) λ=14µm. 113

Fig. 7.8. Absorption coefficient in silicon plotted as a function of hole concentration for a) λ=2µm, b) λ=7.5µm and c) λ=14µm. 114

Fig. 7.9. Refractive index change in silicon plotted as a function of change in electron concentration for a) λ=2µm, b) λ=7.5µm and c) λ=14µm. 114

Fig. 7.10. Refractive index change in silicon plotted as a function of change in hole concentration for a) λ=2µm, b) λ=7.5µm and c) λ=14µm. 115

Fig. 7.11. Comparison of literature data from [2], equations 7.5 and 7.6, and the fitted curves presented in this work from equation 7.3 and table 7.1, for a) holes at 1.3µm, b) holes at 1.55µm, c) electrons at 1.3µm, and d) electrons at 1.55µm. 118

Chapter 1: Introduction

Silicon photonics has attracted great research interest over the last decade for its prospects in the creation of integrated silicon photonic devices for near-infrared data communications, and in particular for use in optical interconnects. There is an opportunity to extend silicon photonics from near-infrared (NIR) wavelengths to the mid-infrared (MIR), where it would open up applications related to chemical and biological sensing, environmental monitoring and free-space communications.

This project is concerned with the development of core components of mid-infrared photonic integrated systems that are made from silicon and other materials from group-IV of the periodic table that are compatible with silicon processing.

1.1. Silicon Photonics

Research into the field of silicon photonics has been driven by the ever increasing need for bandwidth in computing and telecommunications. Copper interconnects have limitations related to loss, dispersion, crosstalk and speed [1] that arise when high interconnect bandwidth is needed over large distances. As ever higher bandwidths are required, optical technologies become cost effective at shorter distances [2]. Very long distance telecommunications links, such as those used in the internet backbone, long ago moved to optical fibre links, but shorter data links do not yet use optical components because of the higher cost, and greater interconnect density required at short distances.

The promise of silicon photonics is that using materials and fabrication methods commercially used in the fabrication of microelectronics will greatly lower this cost. Furthermore, integration of CMOS electronics and photonic components on the same

chip is possible. One goal is to use optical interconnects as a high bandwidth backbone for sending data between multiple cores on future CPU chips [3].

Near-infrared silicon photonics has been around for decades, during which time 1.55µm has emerged as the most commonly used wavelength. The field has already yielded its first commercial products, such as Active Optical Cables produced by Luxtera, Variable Optical Attenuators from Kotura, and biomarker and protein detection tools produced by Genalyte. Intel, IBM, Sun Microsystems and HP are also all conducting research into the field. Further development looks sure to accelerate. Many of the design, fabrication, and characterisation methods that have been developed during this boom in NIR silicon photonics can be exploited in MIR group-IV photonics.

1.2. Mid-infrared photonics research and its applications

The motivation for investigating wavelengths further into the mid-infrared, broadly defined here as wavelengths in the range 3-14µm, comes from the applications that are possible for photonics in this range. The fundamental transition bands of many gases lie in the 3-14µm range, so these gases have strong absorption lines that can be clearly detected through spectroscopic techniques [4]. Many chemical and biological molecules also have strong, unique, absorption bands in the mid-IR [5]. The short-wave infrared (SWIR) is defined here as the 2-3µm wavelength range, and although there are interesting applications for photonics for this range in telecommunications and nonlinear optics, it will not be considered in this project.

Optoelectronic integration of mid-IR devices could be used to create “lab-on-a-chip” type sensors, for example a small, portable FTIR spectrometer that could provide real-time sensing of a number of different gases on the same chip. The application areas for such technologies might include environmental pollution monitoring, toxic chemical detection for homeland security, industrial process control and healthcare, among many others. An exciting medical use would be for quantitative trace analysis of exhaled breath, which provides information about an individual’s health. As a non-invasive method of early disease diagnosis it would in many cases be preferable to taking a blood

test. As an example of an environmental sensing application, there have already been investigations into using mid-infrared sensors for real time subsea monitoring of hazardous pollutants that might pose a threat to global water resources [6]. Existing systems for remote mid-IR sensing are made from discrete components, e.g. [6-8], which are bulky and expensive. Compact and inexpensive sensors would find applications in a great number of application areas.

1.3. Group-IV materials as platforms for mid-IR integrated photonics

Using silicon as a mid-infrared photonic material is a logical step when the advances of telecoms wavelength devices are considered. Firstly, many of the same processing techniques and design methods can be used. In fact, since MIR waveguides must inherently be larger than NIR devices, fabrication tolerances are more relaxed. Silicon has intrinsic material losses lower than 2dB/cm from 1.2 to 6µm and from 24 to 100µm [9]. Another important benefit of the optical properties of silicon is that the charge-carrier effect, the most widely used optical modulation mechanism in silicon, is stronger at mid-infrared wavelengths [10]. This should lead to smaller modulators, which are key components of many photonic systems. Silicon and germanium also have strong third order nonlinearities [11], and at mid-infrared wavelengths two-photon absorption, which encumbers attempts to exploit silicon's nonlinearities in the NIR, falls to zero [12].

However, the migration to longer wavelengths is complicated by many obstacles that must be overcome. The easy availability and relatively low price of suitable MIR sources and detectors is the first requirement for enabling MIR research, and such equipment has only recently become available. A key reason that the telecoms wavelength range is at 1.3µm and 1.55µm is because of the low material absorption of silica fibre-optic cables in this range. At longer wavelengths this absorption becomes too large. Low-loss MIR fibre-optic cables that can be relatively easily handled are a recent development, and are now sold by Thorlabs [13], IRflex [14] and others. Indeed, this is one of the drivers that have enabled MIR photonics research in the last few years.

This hints at the fundamental challenge for MIR silicon photonics: Silicon-on-Insulator (SOI), the material platform of choice for NIR photonics, cannot be used across much of the MIR because SiO_2 has high material absorption in the 2.6-2.9µm range and beyond 3.6µm [9]. So while SOI should still be the preferred material choice wherever the material absorption is not excessive, there is a need to identify and explore other material platforms.

1.4. Thesis outline

The intention of the work making up this thesis is to develop some of the building blocks that would be needed in future for producing full mid-infrared integrated optoelectronic systems, in particular modulators, which have not yet been addressed in the literature.

Soref has discussed the prospects for mid-IR group-IV photonics in a series of papers [15, 9, 16, 17], and what such systems might look like. Figures 1.1 and 1.2 are reproduced from [15], and show top view diagrams of example gas sensing systems.

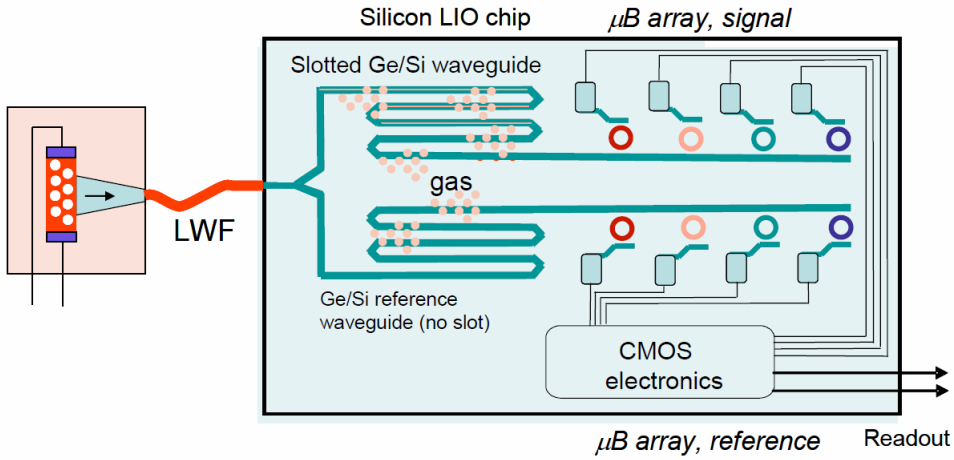

Fig. 1.1 Reproduced from [15]. Silicon longwave integrated chip for sensing, with spectrally broad source, and two banks of longwave sensors for detection of discrete portions of the spectrum.

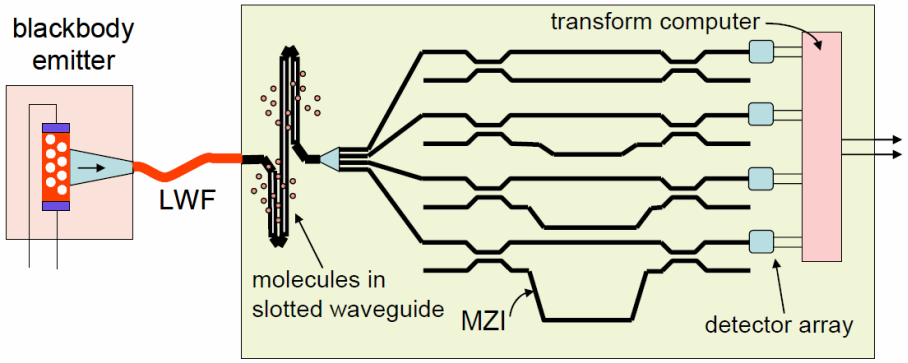

Fig. 1.2. Reproduced from [15]. Waveguided Fourier Transform Infrared Spectrometer (FTIR), with on-chip CMOS computer.

These sensors would both be capable of measuring absorption or refractive index change spectra, and both require the following building blocks.

a. Sources and detectors of light: the light source might be a tunable laser, or it could be a blackbody emitter that emits a broad wavelength range.
b. Waveguides, for routing light around the chip. As discussed in subsection 1.3, alternative waveguide platforms to SOI need to be investigated for different wavelength ranges.
c. Structures for increasing optical interaction of a guided mode with the analyte. In the above examples slot waveguides are used, in which most of the optical mode is confined to an air gap in the middle of the waveguide, but alternatively resonant structures such as ring resonators or photonic crystal cavities might be used, or slow light waveguides such as photonic crystal waveguides.
d. Splitters/couplers: These could be y-junctions, directional couplers or multimode interferometers.
e. Multiplexers/demultiplexers: Echelle gratings, arrayed waveguide gratings and angled MMIs can all be used for multiplexing or demultiplexing different wavelength components of a signal into separate waveguides. Ring resonators, as in the first example, or asymmetric Mach-Zehnder interferometers, as in the second example, can also be used.
f. Modulators: modulators are not shown in either figure, though in a sensor they might be wanted for on-chip signal processing functions. The equivalent of a lock-in amplifier could be realised in order to improve signal to noise ratios. In sensor type applications very high frequency modulation might not be needed.

However, for data communications related applications, in free-space communications or for optical fibre communications at around the 2μm wavelength, speeds on the order of 10s of GHz would be desirable.

This thesis explores three main areas of research to further the field of group-IV photonics. The first is the development and characterisation of different material platforms for waveguiding. The second is development of modulators for the mid-IR, as well as the passive optical components required to create a modulator, namely splitters/couplers and interferometers are demonstrated. The development of integrated sources and detectors is considered to be outside the scope of this project, and external sources and detectors are used for all experiments. The third area is theoretical investigation of the main modulation mechanisms of the plasma dispersion effect, the main modulation mechanism in silicon, at mid-infrared wavelengths. Existing design equations for this effect in silicon are not applicable to longer wavelength devices, therefore a semi-empirical approach is used for quantification of the size of the effect in silicon at wavelengths through the Mid-IR.

Chapter 2: Literature review

This chapter introduces the theory and state of the art regarding mid-infrared waveguides, passive and active components, and finally the plasma dispersion effect in group-IV materials.

2.1. Non group-IV integrated optics

Before presenting the state of the art for MIR group-IV material photonic components, the state of the art for non-group-IV integrated photonic components for the mid-IR should be reviewed. In the literature there have been relatively few demonstrations of non-group-IV material planar waveguides for the mid-IR. III-V material research for the mid-IR has been focused mostly towards sources and detectors. Chalcogenide glass (As_2S_3) waveguides on lithium niobate have been demonstrated with propagation loss as low as 0.33dB/cm [1], although for relatively large cross-section waveguides (width × height = 11μm × 2μm). There have been issues relating to the fabrication of many previously reported chalcogenide based waveguides, such as growth rate limitations and residual stress in deposited layers [2], as well as the vulnerability of As_2S_3 to some photoresist developers that can lead to film delamination and pinhole deformation [2], so protective layers are often necessary. There has also been investigation of selenide and telluride thick films that might be used for mid-IR planar waveguides [3], and silver halide waveguides, which were made by pressing silver halide core optical fibres, have been demonstrated [4].

None of these demonstrated waveguide platforms offers the high refractive index contrast of group-IV material platforms, which can lead to compact waveguides, and the possibility of CMOS integration for group-IV platforms is a significant attraction.

2.2. Waveguides

At the beginning of this section a few basic principles of waveguide theory that are relevant to their behaviour and design will be discussed, following which there will be a

short review of waveguides for NIR silicon photonics. Finally, there is a review of the existing literature relating to group-IV material waveguides for the mid-infrared.

2.2.1 Planar optical waveguides

Light travelling along a waveguide is a transverse electromagnetic (TEM) field, where the electric and magnetic fields are perpendicular to the direction of propagation of the field. For the field to be confined in the waveguide there must be a refractive index difference between the waveguide core and its cladding. Fig. 2.1 shows the geometry of a simple planar (slab) waveguide, which will be considered as the simplest case. The direction of propagation of the TEM field is along the z-axis.

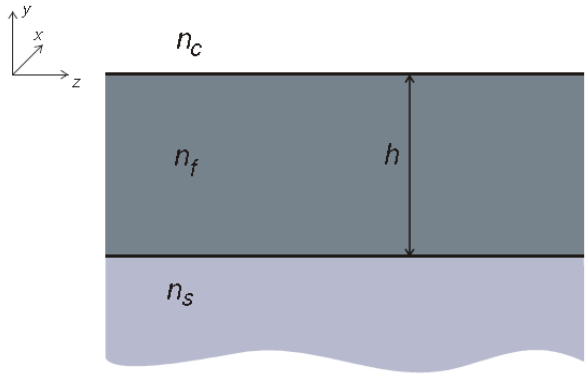

Fig. 2.1. Simple planar waveguide geometry. Diagram reproduced from ref. [5].

The following expressions can be derived from Maxwell's equations to describe the electric field and magnetic field distributions of the electromagnetic wave in the x-y plane inside a medium of uniform refractive index [5]:

$$\frac{d^2E_x(y)}{dy^2}+\left[k_0^2n^2(y)-\beta^2\right]E_x(y)=0 \qquad \text{Eq. 2.1}$$

$$\frac{d^2H_x(y)}{dy^2}+\left[k_0^2n^2(y)-\beta^2\right]H_x(y)=0 \qquad \text{Eq. 2.2}$$

where $E_x(y)$ is the distribution of the x-axis polarised electric field along the y-axis, $H_x(y)$ is the distribution of the x-axis polarised magnetic field along the y-axis, n is the refractive index of the medium, β is the propagation constant of the field, and $k_0^2=\left(2\pi/\lambda_0\right)^2=\mu_0\varepsilon_0\omega^2$. λ_0 is the free-space wavelength of the wave, ε_0 is free-space

permittivity, μ_0 is free-space permeability and ω is angular frequency. Also, $\beta = k_0 n_{eff}$, with n_{eff} being the effective index of the mode.

To solve these equations they must be combined with the boundary conditions of the waveguide region, which are found from the refractive indices of the waveguide core and cladding, the width of the waveguide core, and from continuity of both the electric and magnetic fields and their first derivatives at the material interfaces.

The details of this solution will not be discussed here, as complete consideration of the problem can be found in [5, 6]. However, for a simple slab waveguide, the result when looking at the waveguide cross-section is a sinusoidal electric field profile along the y-axis inside the waveguide core, with the field exponentially decaying in the cladding away from the core. This field outside the waveguide core is referred to as the evanescent field. Inside the core there is effectively a standing wave in the transverse direction, and for continuity at the boundaries there are only particular, discrete field distributions that satisfy the boundary conditions, which are referred to as guided modes. It can be important for a photonic circuit to only support a single mode, particularly in telecommunications where modal dispersion can distort data signals. Elsewhere in a photonic circuit, components such as multimode and Mach-Zehnder interferometers may rely on single mode propagation. The number of modes that are supported is dependent on the waveguide geometry and core and cladding refractive indices.

It is impossible to solve the wave equation for more complex waveguide configurations analytically, including for most geometries used in practice, therefore numerical methods are used, which can be implemented in a range of commercially available simulation packages.

In general, larger waveguides will support more modes. For planar integrated photonics where rectangular waveguides are used, commonly rib or strip waveguides are used, shown in figs. 2.2a and 2.2b.

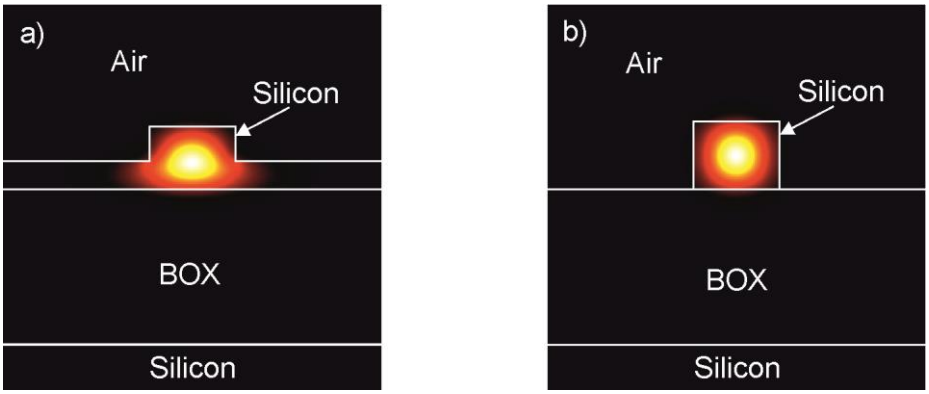

Fig. 2.2. Diagrams of silicon-on-insulator a) rib waveguide and b) strip waveguide, with overlays of typical simulated fundamental mode profiles.

To satisfy the single mode condition for TE polarised modes, the width of strip waveguides must be smaller than the width at which the first higher order mode can propagate, while for TM modes the strip height must be small enough for the waveguide to only support the fundamental mode. However in the case of rib waveguides the waveguide can be made to be larger than the single mode condition dimensions for strip waveguides, because higher order modes will propagate through the slab region of the waveguide, where the losses will be much larger, so these higher order modes will be lost [5]. Rib waveguides can therefore be larger, with dimensions that are easier to fabricate and that have greater tolerance of fabrication errors, but in strip waveguides the optical mode will be confined inside a smaller volume. Tighter confinement would be an advantage that would allow smaller waveguide bending radii, and could be exploited for nonlinear photonic applications where high optical power density is important.

2.2.2 Waveguides in NIR silicon photonics

Most waveguides currently used for NIR silicon photonics are based on Silicon-on-Insulator (SOI) material. SOI consists of a silicon wafer, on the surface of which there is first a silicon dioxide, or “buried oxide” (BOX) layer, followed by a thin silicon layer. The top silicon layer is etched to create a waveguide. A crucial aspect for waveguide behaviour, arising from the solution to the TEM wave equation, is the difference in refractive index between the core of the waveguide, in this case made of silicon

(refractive index, n=3.48 at λ=1.55μm), and of the waveguide cladding, which for SOI is an air (n=1.0) cladding on the top, and SiO_2 (n = 1.45 at λ=1.55μm) cladding on the bottom. This refractive index difference determines how well the optical mode of the waveguide is confined inside the waveguide core, which in turn determines the dimensions of the waveguide, and the minimum acceptable radius of waveguide bends.

The main factors determining the loss of a waveguide are material absorption, losses from radiation modes of the waveguide, and scattering losses from material surface roughness or imperfections in the bulk material. Material absorption is intrinsic to the materials used for the waveguide core and cladding. Radiative losses are minimised through proper design of waveguide geometry through simulation, while scattering losses for SOI in practice mostly come from sidewall roughness, which is a result of fabrication technology and processes.

At the 1.55μm wavelength propagation losses as low as 0.272±0.012dB/cm have been achieved for shallow rib waveguides based on SOI [7], while losses <5dB/cm are readily achievable [8, 9]. These low figures are a result of both low material losses for Si and SiO_2 at this wavelength, and also of mature fabrication processes. Recent years have seen the emergence of fabrication platforms in commercial facilities such as Imec (Leuven, Belgium), LETI (France), IME (Singapore) and IHP (Frankfurt, Germany), which offer multi-project wafer runs to the research community that use standardised processes with which high uniformity is achievable. More broadly, the availability of economical and high quality SOI wafers is in large part limited to two thicknesses for the silicon device layer, which are 220nm and 400nm.

Absorption spectra of Si and SiO_2, which have been digitised from [10] and [11], are shown in fig. 2.3. On each absorption spectrum it can be seen that the material absorption from both materials at 1.55μm is less than 0.05dB/cm, and therefore contributes negligibly to the overall waveguide loss at this wavelength. However, this is not the case for much of the mid-infrared wavelength range which is of interest for this project: SiO_2 has absorption loss greater than 10dB/cm in the ranges 2.6-2.9μm and for wavelengths greater than 4μm, while for Si this is true for wavelengths greater than 8μm.

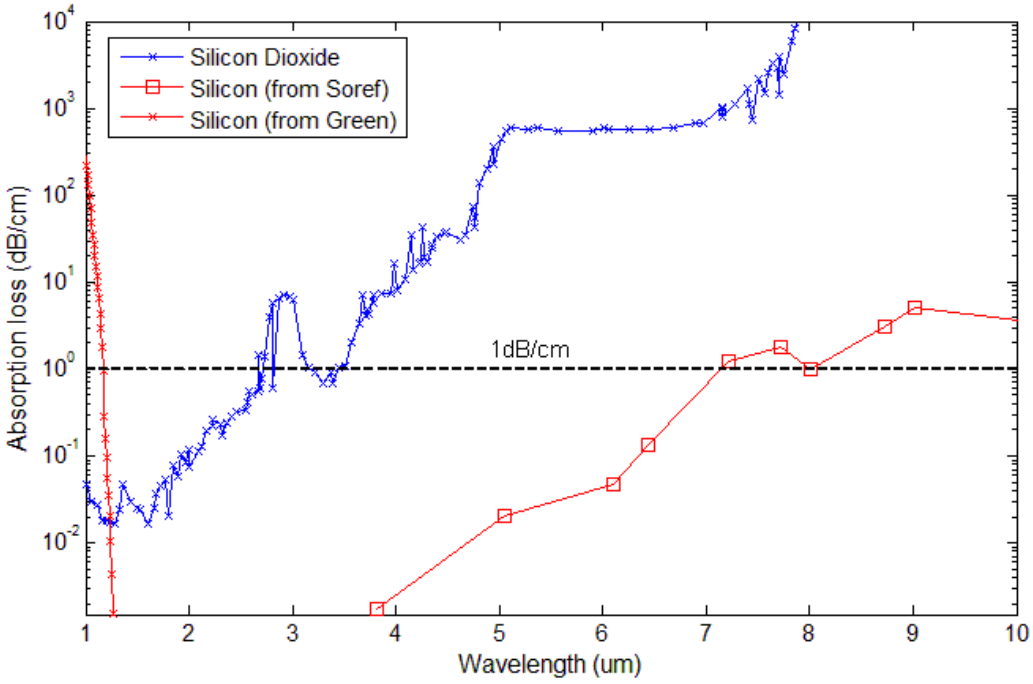

Fig. 2.3. Absorption spectra of silicon (red lines) and silicon dioxide (blue line) for λ=1-10µm, SiO_2 data digitised from ref. [10] Si data digitised from ref. [11] and [12].

In order to develop group-IV photonics for mid-IR wavelengths alternative material combinations will have to be used. It should also be noted that an important route to achieving low waveguide losses is to leverage as much as possible the fabrication processes that have been developed for NIR silicon photonics, which would also be expected to be an economical way of fabricating devices in the long term.

2.2.3 Candidate material platforms for group-IV mid-infrared photonics

Figure 2.4 shows the predicted transparency ranges of the material platforms compatible with group-IV of the periodic table that were suggested by Soref et al. [10]. The data upon which this figure is based is shown in table 1 in appendix 1.

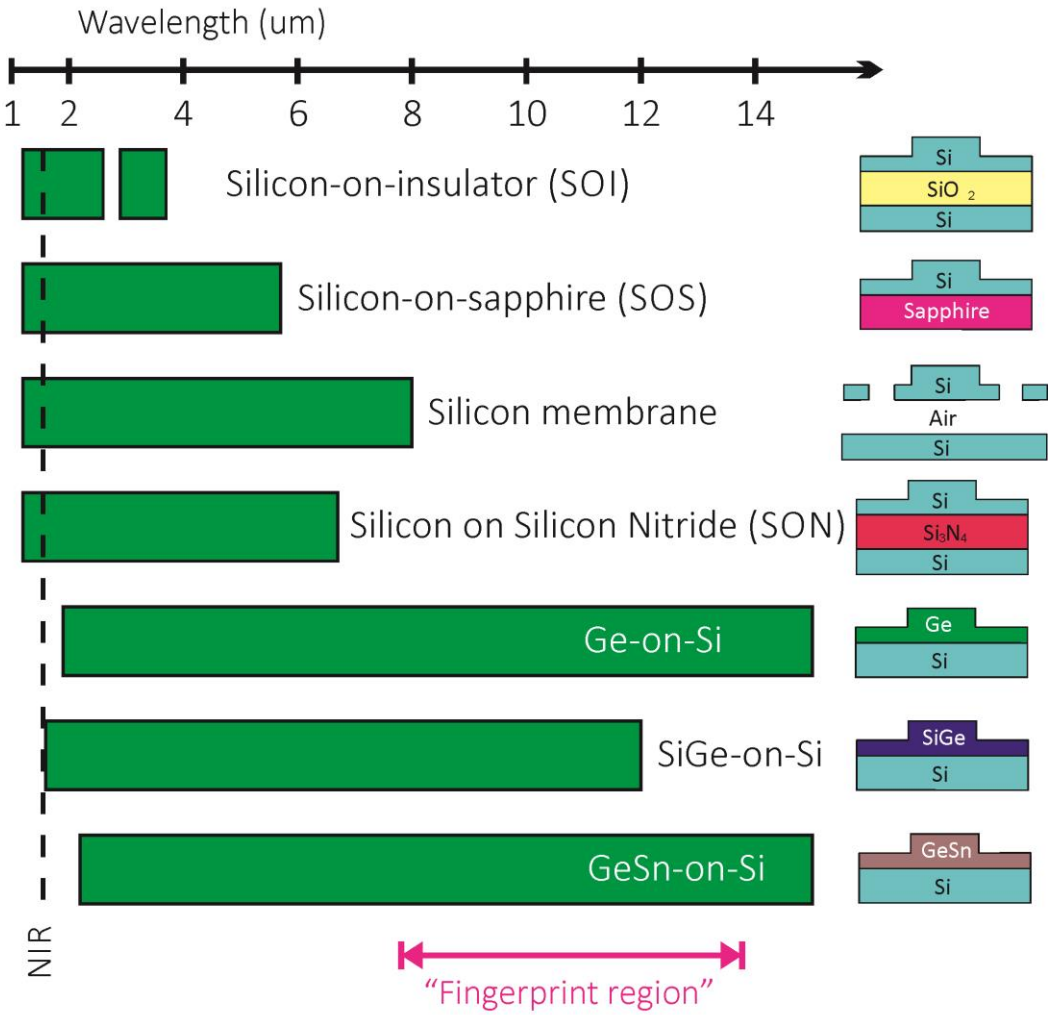

Fig. 2.4. Approximate transparency windows in the 1-14µm range for some of the group-IV material MIR platforms suggested by Soref [10]. Transparency is defined here as loss <1dB/cm, and limits for the ranges are from [10]. For Ge-on-Si and GeSn-on-Si the transparency ranges extend to longer wavelengths. All transparency range values are given in table 1 of appendix 1.

The experimental results that have been achieved to date for each of these waveguide platforms, alongside notes on some practical considerations when using each platform, are listed here. All of the results below have been reported in the years 2010-2013, which reflects the very recent emergence of the field.

- Silicon-on-insulator:

  The SOI platform was demonstrated first at 3.39µm in relatively large rib waveguides (Height x Width = 2µm x 2µm) [13], with low losses of 0.6-0.7dB/cm achieved after smoothing of sidewall roughness by thermal oxidation. The loss was also dependent on the thickness of the buried oxidation layer, as increasing

the BOX thickness from 1µm to 2µm reduced the propagation loss by ~2dB/cm, by reducing leakage to the Si substrate.

SOI strip waveguides with dimensions W x H = 1400nm x 500 were shown to have a loss of 4.6dB/cm at the wavelength 3.74µm [14]. This result represented the first demonstration that SOI waveguides can be used at, and possibly even beyond, wavelengths at which high absorption in SiO_2 sets in (>3.76µm). SOI strip waveguides with a thinner Si layer of 400nm, which is a thickness commonly used for NIR Si photonics, were shown to have a loss of 3.1dB/cm at 3.74µm and 4dB/cm at 3.84µm [15].

- Silicon-on-sapphire:

SOS waveguides have been reported at wavelengths between 3.39µm and 5.5µm [13, 16-18], with losses <2dB/cm [17] for waveguides at 5.18µm with dimensions of W x H = 1000nm x 280nm. One consideration when using SOS for photonics is that due to the hardness of sapphire it is difficult to polish the facets of a SOS chip for end fire coupling from a fibre to the waveguide. The "polishing" of SOS waveguide facets by focused ion beam milling was investigated and successfully demonstrated in [14, 19].

- Silicon-on-porous silicon:

Porous silicon has been used as a lower cladding layer for Si core waveguides in [13]. The refractive index of the porous silicon layer is dependent on its porosity, and in this case was measured to be 1.4, which is similar to that of SiO_2. The waveguides were fabricated by proton beam irradiation followed by a two-step electro-chemical etch in an HF:water:ethanol solution. This same two-step implantation process can be used to create free standing waveguides [20]. The loss of these SiPSi strip waveguides with W x H = 4 x 2µm was initially measured to be 5.6±0.2dB/cm at λ=3.39µm, and was reduced to 3.9±0.2dB/cm after thermal oxidisation for roughness reduction. Most of the loss was attributed to scattering losses due to surface roughness.

- Silicon membrane (undercut SOI):

  Silicon membrane waveguides, meaning SOI waveguides where the SiO_2 underneath the waveguides has been etched away to create an air lower cladding, can extend the wavelength range at which SOI wafers can be used. Waveguides with losses of 3.0±0.7dB/cm have been reported at λ=2.75μm [21], which is a wavelength with high SiO_2 absorption. For these waveguides two etch steps were used; the first etch step is a partial etch through the Si which defines the passive optical elements in the circuit, and in the second step holes are etched through the Si layer just outside the region of optical mode propagation. Finally, the SiO_2 underneath the waveguides is etched away in HF solution. One possible drawback to such waveguides is mechanical stability, though the authors of [21] report no related problems. Another, potentially more serious problem, is that it would be difficult to integrate active devices that require multiple layers with these waveguides.

  Multimode interferometers that are based on under-etched silicon wafers have also been reported [22] at 10.6μm, along with waveguides based on under-etched SOI wafers that were measured to have SOI losses of 11±0.7dB/cm. These devices were based on SOI wafers with 6μm thick Si top layer, 1μm thick SiO_2 layer, and 450μm thick Si susbtrate. Rib waveguides were defined on the Si top layer, after which the substrate was etched underneath the waveguides from the wafer back surface, until only 3μm of the Si substrate remained. The whole Si substrate was not removed so as to preserve mechanical stability. The resulting waveguide losses resulted from material absorption in Si (~5dB/cm at 10.6μm), from material absorption in the SiO_2 layer (~3000dB/cm at 10.6μm), and from leakage into the Si substrate.

- Silicon nitride:

  Silicon nitride (SiN_x) is transparent up to 8µm, and in 2013 two waveguide platforms utilizing silicon nitride have been demonstrated. The refractive index of SiN_x is dependent on the deposition conditions, which determines the Si to N_x ratio of the material, so that the refractive index can be anywhere in the range $1.57<n<2.76$ [23]. High stress in SiN_x can be an issue, especially when using thicker layers, so care must be taken when choosing the deposition conditions.

  In ref. [24] silicon on silicon nitride (SON) waveguides were made by first depositing SiN_x on a SOI wafer by plasma enhanced chemical vapour deposition (PECVD), before bonding a silicon substrate to this wafer using spin on glass. The silicon from the original SOI wafer was then removed by lapping the first 400µm of the Si and etching the remaining 100µm, and finally removing the SiO_2 layer using HF. After photolithography the resulting rib waveguides had a silicon core, from the original SOI wafer, and a SiN_x lower cladding. Their propagation loss for waveguide dimensions W x H = 2.25 x 2µm and 0.8µm etch depth was 5.2±0.6dB/cm for the TE mode and 5.1±0.6dB/cm for the TM mode at λ=3.39µm.

  In ref. [25] silicon nitride on silicon dioxide waveguides were fabricated by low-pressure chemical vapour deposition (LPCVD) of a 2.5µm thick SiN_x layer onto a 4 µm thick SiO_2 substrate, which was grown by wet thermal oxidation on a silicon wafer. The refractive index contrast for this material combination (n=2.1 for SiN_x in this case and n=1.4 for SiO_2) is small relative to that for SOI, so waveguides must be larger. Single mode strip waveguides with W x H = 4µm x 2.5µm were measured to have a propagation loss of 2.1dB/cm at 3.70µm. An important drawback to this platform is that it does not address the problem of high SiO_2 absorption at longer wavelengths, so its wavelength range of operation will be similar to SOI.

- Germanium-on-silicon (Ge-on-Si):

  The first demonstration of Ge-on-Si waveguides was published in 2012 [26]. To form the Ge-on-Si, 10μm of intrinsic Si was first deposited on a silicon wafer as a buffer layer, on the surface of which a 2μm thick Ge layer was grown by reduced pressure chemical vapour deposition (RP-CVD). Ref. [27] gives greater detail about the fabrication process. The waveguides were characterised at λ=5.8μm, and the propagation loss at this wavelength was 3.6dB/cm. Ge-on-Si waveguides have since been reported at λ=2.0-2.6μm [28] and at λ=5.0-5.4μm [29]. At 2.0μm the measured loss for multimode strip waveguides (W × H = 2.25μm × 1μm) was 5.4dB, falling to 2.3dB/cm at 2.6μm. The large reduction over this wavelength range is thought to be caused by material absorption in germanium due to the tail of the fundamental band edge of Ge, and material absorption of ~3dB/cm at 2.0 μm is approximately consistent with literature absorption spectra for intrinsic Ge [30]. At 5.15-5.45μm, the loss for single mode strip waveguides with dimensions W × H = 2.2μm × 2μm was 2.3-3.5dB/cm for TE polarization and 3-4dB/cm for TE polarization. This same material platform was then used to create arrayed waveguide grating (AWG) [29] and planar concave grating (PCG) [31] multiplexers for the 5μm wavelength range.

  This material platform is expected to have the widest range of operation of all those discussed so far, and this result is particularly important because it represents the first transmission measurement through planar Ge waveguides. Silicon is not the ideal substrate for Ge waveguides because it is likely to restrict the transparency window of the platform to somewhere in the range λ=8-16μm, depending on the proportion of the optical mode that travels through the Si cladding, and because there is a relatively small refractive index contrast between Ge (n=4.0) and Si, limiting photonic circuit integration density.

It is clear that in exploring different waveguide platforms the desired aim is waveguides that have a wide spectral transparency range, low propagation loss, tight optical

confinement and a simple fabrication process. Currently none of the demonstrated waveguide platforms achieve all of these aims.

There has also been some interesting published work concerning photonic component integration in the NIR. There has been some progress on monolithic integration of GeSn devices on Ge, which could result in integrated lasers and photodetectors operating at wavelengths up to 2.5µm [32]. GaSb photodtectors have also been integrated with silicon waveguide circuits using a wafer bonding approach, and photodetectors were demonstrated operating at 2.5µm [32]. Such photodetectors could operate at wavelengths up to 3.5µm. This bonding approach is costly, and to circumvent this the same authors proposed, and have made some early progress, using integration of IV-VI colloidal quantum dots on a silicon circuit [32].

2.3. Passive photonic components

Passive photonic components can perform a variety of functions in a photonic circuit, such as splitting or coupling light into different waveguides, increasing the interaction of a guided optical mode with an analyte, multiplexing/demultiplexing light, or they can be used as building blocks of active structures, such as those used for modulation.

2.3.1 Waveguide bends

Though waveguide bends are simple structures they still require careful design to ensure that they do not introduce a large loss. Bend losses inherently occur due to radiation loss of the waveguide mode into the cladding as it propagates around the bend [5]. The bend loss therefore depends largely on the confinement of the optical mode within the waveguide. A large bend radius will reduce bending loss, while a smaller bend radius allows tighter component integration on a chip.

Material platforms with a high refractive index contrast between core and cladding therefore allow for smaller bend radii, and in strip waveguides smaller bend radii are achievable than in rib waveguides due to the low lateral confinement of rib waveguides [7]. For example, for the NIR, the authors of ref. [7] suggest that to achieve low loss for both waveguides and waveguides bends, where very tight bends are required a good

approach is to use two etch steps, so that straight waveguides are etched as ribs, and bend waveguides are etched to be strips, with transition regions joining the two waveguide types.

2.3.2 Multimode interferometers

Splitters and couplers are important for guiding light around a chip, and they also form key parts of structures such as Mach-Zehnder interferometers. The Mach-Zehnder structure needs a splitter at the beginning of the device to separate light into the two arms, and a combiner at the end of the structure to do the reverse. Multi-mode interferometers (MMI) are devices that can be used for both functions. MMIs operate on the principle of self-imaging in multimode waveguides [33]. The central part of an MMI is a waveguide section that can support a large number of modes that interfere with each other. The result is that the input mode profile is replicated at various points along the length of the MMI, and at certain points in the z-direction there will be multiple images of the input mode spaced in the x-direction, as shown in fig. 2.5. Depending on the number of input and output ports an MMI can be used as a coupler, splitter or combiner [5].

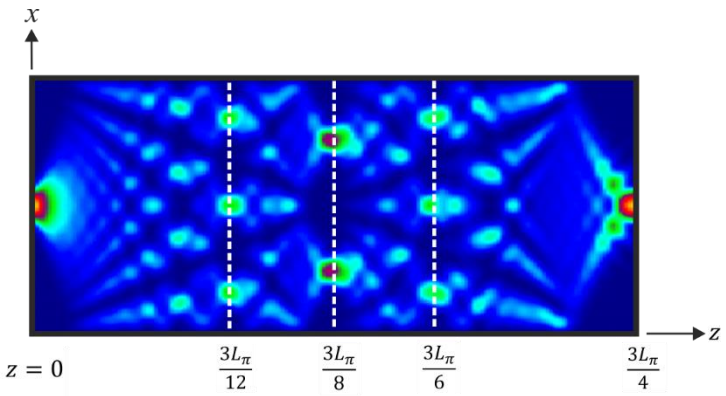

Fig. 2.5. Intensity plot of the field in the multi-mode section of an MMI. Red areas indicate high intensity, blue indicates low intensity. The positions of the single-fold, two-fold, and three-fold self-imaging locations have been labelled.

The MMI is not the only type of splitter/coupler. Directional couplers consist of two parallel waveguides that are very close to each other, where the light is coupled from one waveguide into the other (or the light from both is combined in each one) via the evanescent field. Y-junctions simply look like one waveguide splitting into two in a Y-

pattern. However, the advantages of MMI's are that they can be very short (tens of micrometers), and are tolerant of fabrication imperfections. Directional couplers can be hundreds of micrometers long [34], while Y-junctions are very sensitive to fabrication error at the tip of the split of the waveguide, which can cause large losses through scattering or uneven light splitting [35]. Fig. 2.6 shows schematic diagrams of these three splitter/coupler types.

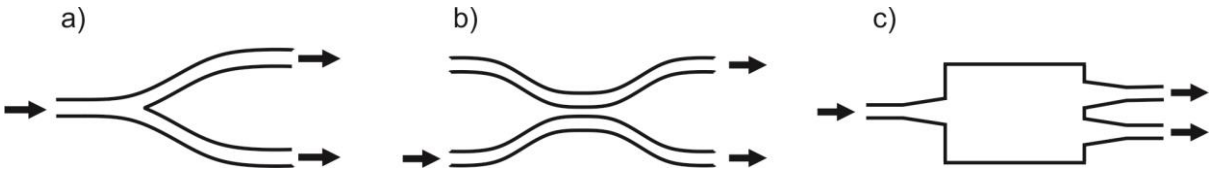

Fig. 2.6. Diagrams of common 1 x 2 splitter/coupler structures: a) Y-splitter, b) directional coupler, c) multi-mode interferometer with tapered input and output ports.

An approximation for the points at which two-fold self-imaging occurs along the MMI length is given by [33]:

$$L_{MMI} = \frac{3\pi}{8\left(\beta_0 - \beta_1\right)} \qquad \text{Eq. 2.3}$$

Where β_0 and β_1 are the propagation constants of the fundamental and first order modes in the multimode waveguide section. For a 1x2 MMI with one input and two output ports (or vice-versa) two-fold self-imaging occurs at $z = 3L_\pi/8$ where z is the distance in the direction of light propagation, and L_π is the beat length, defined in the 2D approximation as:

$$L_\pi = \frac{4 n_{eff} W_{eff}^2}{3\lambda} \qquad \text{Eq. 2.4}$$

where W_{eff} is the effective width of the waveguide (defined in [5]), n_{eff} is the effective refractive index of the multimode waveguide, and λ is the wavelength. From this theory, the length of the device is proportional to the square of its width, and is inversely proportional to the wavelength [33].

Thomson and Hu [36] explored MMI structures in which the input and output waveguides are tapered in order to reduce losses due to a modal mismatch where the narrow single mode waveguides meet the multimode section. In doing this they saw a

decrease in fabricated device losses from around 1.6dB to around 0.5dB. This is therefore a simple method to improve MMI performance. So far the lowest loss for an MMI structure for the NIR is 0.2dB/MMI, which was reported in [37]. This was achieved with a two-step etch process, where a transition in the access waveguides from a deep etch to a shallow etch reduces the mode mismatch between the access waveguide and multimode waveguide, which is similar to the tapered MMI principle.

In the MIR Milošević *et al.* reported a MMI [14] based on SOI with 500nm thick Si layer, and achieved losses of 3.6±0.2dB/MMI. This relatively high loss was assumed to be due to differences between the device's design and ultimate fabrication dimensions. Wei *et al.* [22] also reported a silicon MMI with an air lower cladding operating at 10.6µm, with a very large insertion loss of 23.0dB. This large loss was due to the MMIs being based on large Si rib waveguides which exhibited high leakage to the Si slab, and a large total device length of 15.6mm, including tapered access waveguides. The loss would be expected to be reduced by further optimisation of the waveguide geometry to reduce Si slab leakage, and a reduction of the overall length by reducing the width, and therefore length, of the multimode region.

2.3.3 Mach-Zehnder interferometers

The Mach-Zehnder interferometer is a structure where optical power is split into two arms, before it is again recombined into one waveguide. The phase of the light can be changed in one or both arms by introducing an optical path length difference or by modulating the refractive index. In this way the device acts as an interferometer. It can be used as part of a modulator structure to convert a phase change into an intensity change. A 1x1 MZI structure like the one just described is shown in fig. 2.7. There are also other configurations, including a 1x2 MZI that incorporates another splitter, such as a 2x2 MMI, into the recombiner. In this configuration changing the phase of light at the recombiner switches light from one output waveguide to the other.

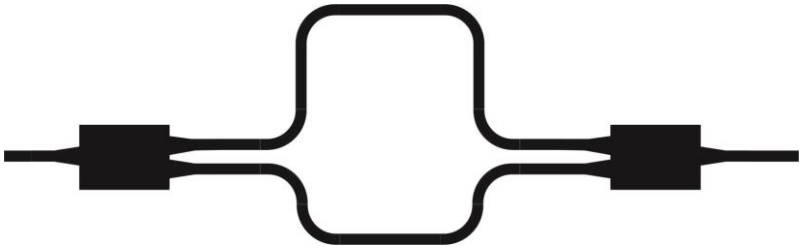

Fig. 2.7. Asymmetric 1 x 1 Mach Zehnder interferometer.

An asymmetric MZI, where one of the arms is longer than the other can also act as a wavelength filter. This behaviour is governed by these equations [5]:

$$\eta = \frac{P_o}{P_{in}} = \cos^2\left(\Delta\phi/2\right) \qquad \text{Eq. 2.5}$$

$$\Delta\phi = \frac{2\pi n_{eff}\Delta L}{\lambda} \qquad \text{Eq. 2.6}$$

Where η is the Mach-Zehnder efficiency, P_o is the output power, P_{in} is the input power, $\Delta\phi$ is the change in phase, n_{eff} is the effective refractive index of the waveguide, ΔL is the optical path length difference and λ is the wavelength. In the ideal case (as in the above equation) the extinction ratio when there is a π phase shift ($P_\eta=0 / P_\eta=1$) will be equal to zero, but optical absorption in each arm will degrade the extinction ratio.

Mach-Zehnders for the MIR have been used in the literature in the demonstration of a carrier-injection modulator operating at λ=2165nm [38], and to enable a group index measurement of photonic crystal waveguides at λ=3.8μm [39], but in both papers there was no investigation of the properties of the MZI itself.

2.4. Modulators

Optical modulators are devices in which an electrical signal is applied to create a change in an optical signal, which may be a change in phase or amplitude. Modulators are the key components for optical communication applications, and the maximum frequency of the modulator determines the data rate. The following are the key “figures of merit” for an optical modulator [40]:

- Modulation speed: the ability of a modulator to carry data at a certain rate.

- Modulation depth: the optical intensity of the OFF signal divided by that of the ON signal, which is important for long distance applications where low bit error rates are required.
- Optical bandwidth: frequency at which the modulation falls to -3dB of the maximum value.
- Insertion loss: the total optical loss of the device.
- Power consumption (power/bit): power consumption is a key metric for short reach optical interconnect applications.
- Footprint/area efficiency: the area on the chip filled by the device.

The ability of a given device to achieve high performance in any of these metrics tends to be linked, and trade-offs in the optimisation of the device need to be made.

2.4.1 Electro-optical modulation mechanisms in semiconductors

To create an electro-optical modulator a change in an electrical signal must create a change in either the absorption coefficient, $\Delta\alpha$ (electro-absorption), or refractive index, Δn (electro-refraction) of the material through which light is propagating. In fact, according to the Kramers-Kronig relations any change in absorption coefficient (imaginary part of refractive index) is accompanied by a change in the real part of the refractive index [5].

The electric-field effects most often used in semiconductor materials are the Pockels effect, the Kerr effect and the Franz-Keldysh effect. The Pockels effect is otherwise known as the linear electro-optic effect, which alters the refractive index of a material when an electric field is applied across it, in proportion to the electric field strength. The Kerr effect is a nonlinear effect in which an applied electric field produces a change in the refractive index that is proportional to the square of the electric field. The Franz-Keldysh effect produces a change in the semiconductor's band structure on application of an electric field, and therefore changes the absorption properties of the crystal, and in particular will produce a shift in the wavelength of the material's band gap.

These effects are commonly used in III-V semiconductors; lithium niobate modulators, which are very widely used in optical links for telecommunication networks, use the Pockels effect. The advantage of these effects is that they act very quickly. However,

because silicon has a centrosymmetric structure the Pockels effect disappears completely, the Kerr effect is very small in silicon, and the Franz-Keldysh effect is strong at wavelengths very near the fundamental band gap, but is greatly diminished even at the NIR telecommunication wavelengths [41].

Using the free-carrier plasma dispersion effect for modulation was proposed by Soref and Bennett in 1987 [41]. In the plasma dispersion effect the concentration of charge-carriers (electrons or holes) in the semiconductor is changed, which changes its absorption coefficient and refractive index. The details of this physical effect form a significant part of this thesis, and will be discussed at length in later sections. Over the last 25 years the plasma dispersion effect has become the dominant method of modulation in silicon modulators.

Silicon also has a large thermo-optic effect, whereby a change in the material temperature produces a change in the real part of its refractive index. The spectral dependence of the thermo-optic effect in silicon at 300°K is shown in fig. 2.8, which shows that while the effect is ~9% weaker at 3.5µm than at 1.5µm, it can be a useful modulation mechanism at least throughout the 1.3-6µm range [42].

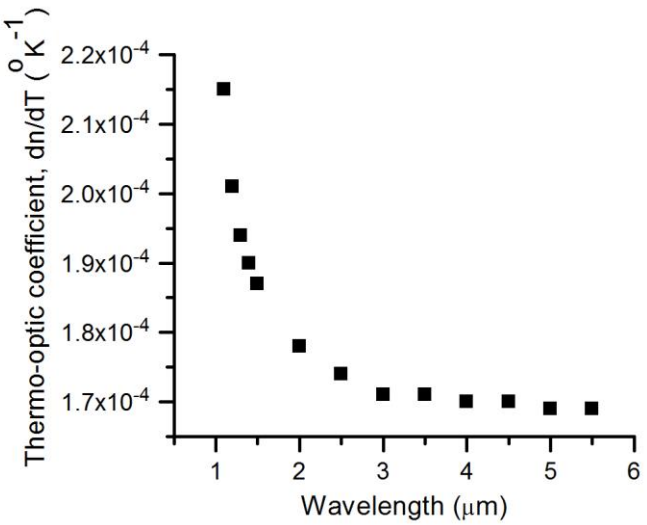

Fig. 2.8. Spectrum of thermo-optic coefficient of silicon at 300°K, for λ=1.1-5.5µm, plotted data from ref. [42].

2.4.2 Mid-infrared modulators in literature

Non-silicon modulators for the MIR have been reported, most of which are discrete structures, or large area devices. For example, a germanium plasma dispersion effect modulator utilizing a p-i-n junction for carrier injection has been reported [43] for the 8-12μm range, but was a large area normal incidence device, and was not waveguide integrated. Similarly, a spatial modulator based on vanadium dioxide thin films has been demonstrated [44], for application in imaging of missile testing, but is not part of an integrated photonic system. A MIR modulator made from lithium tantalate (LTA), and operating at wavelengths up to 4μm and at modulation frequencies of up to 1GHz, is commercially available from [45], and is also a discrete component. Direct modulation of quantum cascade lasers has also been reported by a number of authors, e.g. [46, 47], and modulation speeds have reached up to 1.4GHz [47]. However, the size and expense of such systems prohibits their use in "lab-on-a-chip" type applications. For the SWIR, there is a commercially available discrete component lithium niobate modulator, which is commercially available from PhotLine, and has a typical electro-optic bandwidth of 12GHz.

To produce a compact, integrated photonic sensor system based on a group-IV material platform it is crucial to produce modulators that can be integrated with waveguides made from group-IV materials. In the next section the configurations for waveguide integrated modulators that are used for NIR silicon photonics are reviewed.

2.4.3 Silicon modulators device structures

There are three commonly used methods of changing the concentration of charge-carriers in the core of a silicon waveguide: carrier injection, carrier accumulation and carrier depletion. Each modulator type would typically be used as a phase shifter within a component that could convert a phase change into an intensity change, such as a ring resonator or Mach-Zehnder interferometer.

- Carrier injection

Carrier injection modulators might be based on a p-i-n diode (p-type, intrinsic, n-type) structure, where the waveguide core is intrinsic silicon, as shown in fig. 2.9b. Highly

doped p++ and n++ are placed at either end of the diode, and metal electrodes contact these doped areas through vias in a layer of oxide to create Ohmic contacts. When a forward bias is applied across the electrodes charge-carriers are injected into the waveguide core. In such devices the bandwidth is limited by the minority carrier lifetime, i.e. the time taken for minority carriers to recombine, which will be a function of the separation distance between the p-type and n-type contact areas.

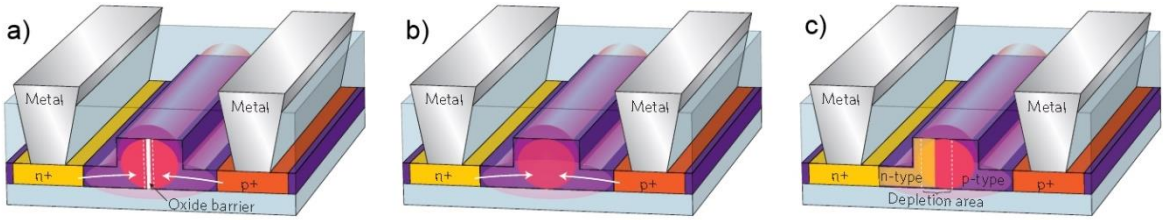

Fig. 2.9. Schematic cross-sections of typical silicon modulators based on the plasma dispersion effect [39]. a) Carrier accumulation modulator. b) Carrier injection modulator. c) Carrier depletion modulator.

In NIR Si photonics bandwidths of 10-18Gb/s have been achieved in carrier injection modulators [48, 49] using p-i-n diode structures incorporated into both MZIs and ring resonators. In order to achieve such high speeds pre-emphasis driving techniques are required, in which carriers are injected rapidly with a high current, following which a lower current is used to maintain an "ON" state. This is done by using pulses at the rising edges of the modulating signal [49]. However, complex driving circuitry is required to generate this electrical signal.

To date the only reported Si based modulator operating at wavelengths longer than the telecommunications band has been a carrier injection type modulator operating at λ=2165nm [38], which achieved bitrates up to 3Gbps with pre-emphasis techniques. The demonstrated devices were made up of phase shifters placed in the arms of an MZI, based on rib waveguides of 220nm height, 500nm width and 170nm etch depth. The device dimensions were very similar to those used at λ=1.55μm, and perhaps further optimisation could be achieved through wavelength specific device design, particularly through accurate modelling of the plasma dispersion effect at that wavelength.

- Carrier accumulation

In modulators operating on the basis of carrier accumulation, carriers are accumulated on either side of a dielectric barrier inside a waveguide core. Modulators of this type are not limited by minority carrier lifetimes, which are relatively long, and are instead limited by the device resistance and capacitance [40]. The first modulator to achieve modulation frequencies greater than 1 GHz was based on carrier accumulation [50], and later optimised to operate at up to 10Gb/s [51], although the achieved extinction ratio was only 1.3dB. A drawback of this device type, dependent on its configuration, is potentially complex fabrication processes.

- Carrier depletion

The fastest modulators that have been demonstrated for NIR Si photonics have been carrier depletion type modulators, based on PN junctions (p-type/n-type) operated in reverse bias. The waveguide core is heavily doped, and when a reverse bias is applied carriers are swept out of the waveguide core. As with accumulation type devices, bandwidth limitations are dominated by device resistance and capacitance. Carrier depletion modulators were demonstrated experimentally much later than carrier injection, because the width of the depletion region is relatively small (e.g. approximately 60nm with no voltage applied, increasing to 200nm with an applied reverse bias of 6V [8]), and before waveguides with submicron dimensions were readily achievable the overlap between the depletion region and waveguide mode was too small to create sufficient modulation.

The first carrier depletion modulator was simulated in [52], and the first experimental demonstrated was by Intel, who achieved 30Gb/s data transmission [53]. Since then many carrier depletion type modulators have been demonstrated, and speeds of 50Gb/s have been achieved by Thomson et al. [54]. Fig. 2.10 shows the schematic cross-section of the phase shifter of this device, which employs a self-aligned fabrication process to reliably define the lateral location of the depletion region.

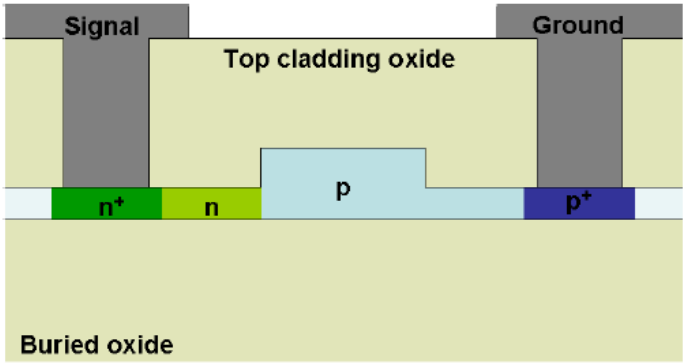

Fig. 2.10. Cross-section of self-aligned carrier depletion phase shifter, reproduced from [54].

- Thermo-optic modulators

The principal drawback to devices that utilise the thermo-optic effect for modulation is their very low bandwidth compared to plasma dispersion effect devices, due to the relatively low rate of thermal transport. Nevertheless, such devices can be simpler to fabricate, and can be useful for applications where high frequency operation is not required. For NIR thermo-optic modulators simple metal wire heaters are placed above one arm of a Mach-Zehnder interferometer [55] or above ring resonators [56], which are separated from interaction with the optical mode by a layer of SiO_2. Typical modulation speeds that have been achieved have been in the range ~5-100μs (i.e. bandwidth in the range 3.5kHz-70kHz) [55]. Densmore et al. proposed using a Mach-Zehnder interferometer with coiled spiral arms, and a heater above one arm, in order to improve the efficiency of thermo-optic modulators, and noted a reduction of over five times compared to using MZIs with straight arms (~35mW switching power for straight arms, and ~6.5mW for spiral arms) [55].

2.5. Free-carrier absorption in silicon

The free-carrier plasma dispersion effect is the most widely used modulation mechanism in NIR silicon photonics, and Soref and Bennett proposed the following expressions to describe the magnitude of electroabsorption and electrorefraction due to the effect at λ=1.55μm [41]:

$$\Delta n = \Delta n_e + \Delta n_h = -8.8\times10^{-22}\Delta N_e - 8.5\times10^{-18}\left(\Delta N_h\right)^{0.8} \qquad \text{Eq. 2.7}$$

$$\Delta\alpha = \Delta\alpha_e + \Delta\alpha_h = 8.5\times10^{-18}\Delta N_e + 6.0\times10^{-18}\Delta N_h \quad \text{Eq. 2.8}$$

Δn is the total change in refractive index, Δn_e and Δn_h are the change in refractive index due to changes in electron and hole concentrations, respectively, $\Delta\alpha$ is the total change in absorption coefficient, $\Delta\alpha_e$ and $\Delta\alpha_h$ are the changes in absorption coefficient due to changes in electron and hole concentrations, and ΔN_e and ΔN_h are the changes in electron and hole concentration. These equations are only applicable at λ=1.55µm, with similar equations available at λ=1.3µm, but it is known that there is a strong wavelength dependence of the effect. One focus of this thesis is therefore the accurate prediction of these effects at mid-infrared wavelengths in silicon, in order to enable accurate design of group-IV material mid-IR modulators. In this section the basic theory of free-carrier absorption will be introduced.

2.5.1 Classical free-carrier absorption theory

In free-carrier absorption (FCA) a photon is absorbed and a charge-carrier is excited from a low energy state within the conduction or valence band to a higher energy level within the same band, as shown in the band diagram in fig. 2.11.

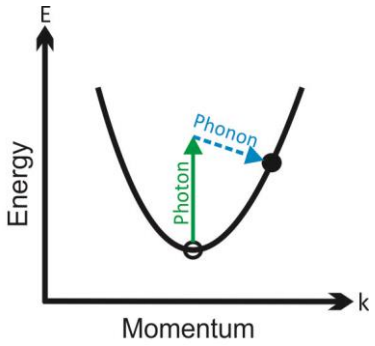

Fig. 2.11. Band energy diagram showing intravalley free-carrier absorption.

This is an indirect process for which momentum conservation is required, which is satisfied through scattering processes. Classical Drude theory provides a simple model for FCA in which free carriers in a bulk material are modelled as a plasma, with the free-carriers acting as scattering centers for the incoming photons [57]. The results are equations 2.9 and 2.10 below, where the change in absorption coefficient, $\Delta\alpha$, and refractive index, Δn, due to free-carriers is proportional to the square of the wavelength of the light [41].

$$\Delta n = -\left(\frac{e^2\lambda^2}{8\pi^2 c^2 \varepsilon_0 n}\right)\left[\frac{\Delta N_e}{m_{ce}^*} + \frac{\Delta N_h}{m_{ch}^*}\right] \quad \text{Eq. 2.9}$$

$$\Delta \alpha = \left(\frac{e^3\lambda^2}{4\pi^2 c^3 \varepsilon_0 n}\right)\left[\frac{\Delta N_e}{m_{ce}^{*\,2}\mu_e} + \frac{\Delta N_h}{m_{ch}^{*\,2}\mu_e}\right] \quad \text{Eq. 2.10}$$

ΔN_e and ΔN_h are the change in electron and hole concentration, respectively, e is the electronic charge, λ is the wavelength, c is the speed of light in a vacuum, ε_0 is the permittivity of free space, n is the refractive index of the unperturbed material, m_{ce}^* is the conductivity effective mass of electrons, $m_{ch}^*$is the conductivity effective mass of holes, μ_e is the electron mobility and μ_h is the hole mobility. It should be noted that equations 2.9 and 2.10 are a simplified form of the Drude-Lorentz equations, with a simplifying assumption that holds for the mid- and near-infrared, but not for the far-infrared [58].

According to this model both electrorefraction (ER) and electroabsorption (EA) are directly proportional to the square of the wavelength of incoming photons. While this model is useful as a first approximation of FCA it has been shown to be inaccurate when used to predict EA and ER due to carriers in Si [41, 57]. Drude theory neglects contributions to absorption provided by scattering centres other than the free-carriers themselves. Lattice scattering and impurity scattering provide more ways for momentum conservation to be satisfied, and absorption related to these effects does not share the λ^2 dependence.

2.5.2 Intersubband free-carrier absorption

Figs. 2.12a and 2.12b show examples of the absorption spectra of moderately doped n-type Si and p-type Ge.

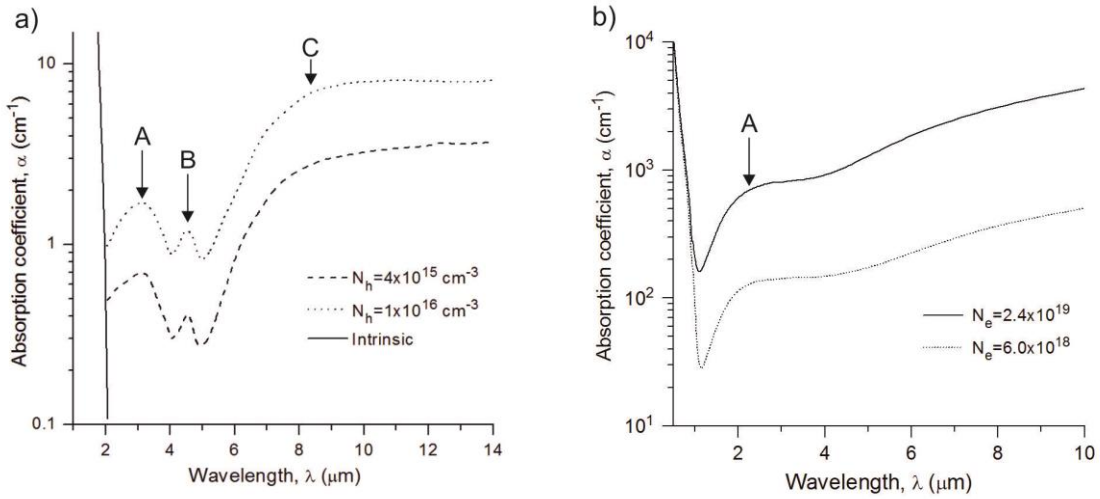

Fig. 2.12. Example absorption coefficient spectra of heavily doped Si and Ge, digitised from literature. a) p-type Ge [59]. The marked features labelled A, B and C are due to direct intervalence band transitions. b) n-type Si [60]. The feature labelled A is due to interconduction band transitions of electrons.

The "humps" that can be seen in these spectra are due to intersubband absorptions, where a carrier is raised to a higher energy level in a different valley of the same band. For example, in n-type Si the "hump" marked at position A in fig. 2.12b is likely due to a transition in the conduction band from the X-valley to the L-valley [60], similar to what is shown in fig. 2.13a. In p-type Ge there are three absorption bands due to intervalence band transitions. The bands at positions A, B and C are due to heavy-hole to light-hole (1), heavy-hole to split-off band (2) and light-hole to split-off band (3) direct transitions respectively, as marked in fig. 2.13b.

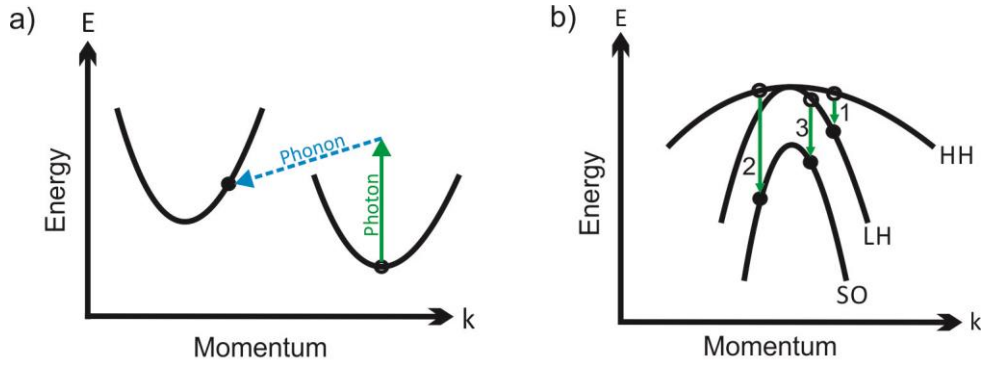

Fig. 2.13. Intersubband free-carrier absorption mechanisms. a) Indirect intervalley free-carrier absorption, e.g. from the L-valley to the Γ-valley of the Ge conduction band. b) Direct intervalence band absorption. The numbered processes show photon-assisted transitions of

carriers between: 1. Heavy Hole -> Light-Hole 2. Heavy-Hole -> Split-off band 3. Light-Hole-> Split-off band.

Absorption due to these absorption processes is dependent on the free-carrier concentrations in the material, which is demonstrated in fig. 2.12, and which shows greater absorption for higher doping concentrations. Therefore these absorption mechanisms must be part of any consideration of FCA.

2.5.3 Soref and Bennett approach for prediction of electroabsorption and electrorefraction in silicon

In their paper from 1987 Soref and Bennett [41] adopted a semi-empirical approach towards calculating the plasma dispersion effect in Si. The approach is based on the absorption spectra of doped silicon wafers, which are available in the literature, because it is difficult to directly measure changes of optical properties due to charge-carrier injection or depletion. The absorption due to charge carriers introduced by doping is assumed to be the same as that of injected free-carriers. Δα curves are found by subtracting the undoped spectrum from doped spectra, from which Δn spectra can be calculated using the Kramers-Kronig relationships which link the absorption coefficient of a material to its refractive index:

$$\Delta n(\omega) = (c/\pi) P \int_0^\infty \frac{\Delta\alpha(\omega')\, d\omega'}{\omega'^2 - \omega^2} \qquad \text{Eq. 2.11}$$

where $\hbar\omega$ is the photon energy. This can be rewritten in terms of normalized photon energy V, where $V = \hbar\omega/e$:

$$\Delta n(V) = 6.3\times10^{-6}\ P \int_0^\infty \frac{\Delta\alpha(V')\, dV'}{V'^2 - V^2} \qquad \text{Eq. 2.12}$$

P indicates that the principal part must be taken, as there is a singularity at $V' = V$. This can be calculated by numerical integration using a trapezoidal rule approximation [61]. The theory requires that the integration is carried out for all photon energies 0 to ∞, but in practice the free-carrier absorption saturates at and levels off at low energies, and at high energies the doped sample spectra meet the intrinsic spectrum (fig. 2.14).

The key advantage of this approach is that the experimental absorption spectra should include contributions from all absorption mechanisms, although it is not entirely clear to what extent the implicit assumption that ionized impurities contribute negligibly to the absorption is valid. The major drawback is that the accuracy is reliant not only on the accuracy of the experimentally measured absorption spectra, but to calculate Δn at any wavelength absorption spectra for all wavelengths are required. In practice, for silicon there are experimental spectra available for both p-type and n-type Si for the NIR and mid-IR for moderate to heavy doping, though for the far-infrared spectrum the available spectra are less complete. Figs. 2.14a and 2.14b show absorption spectra that are composites from multiple sources, which were used in the calculations in ref. [41].

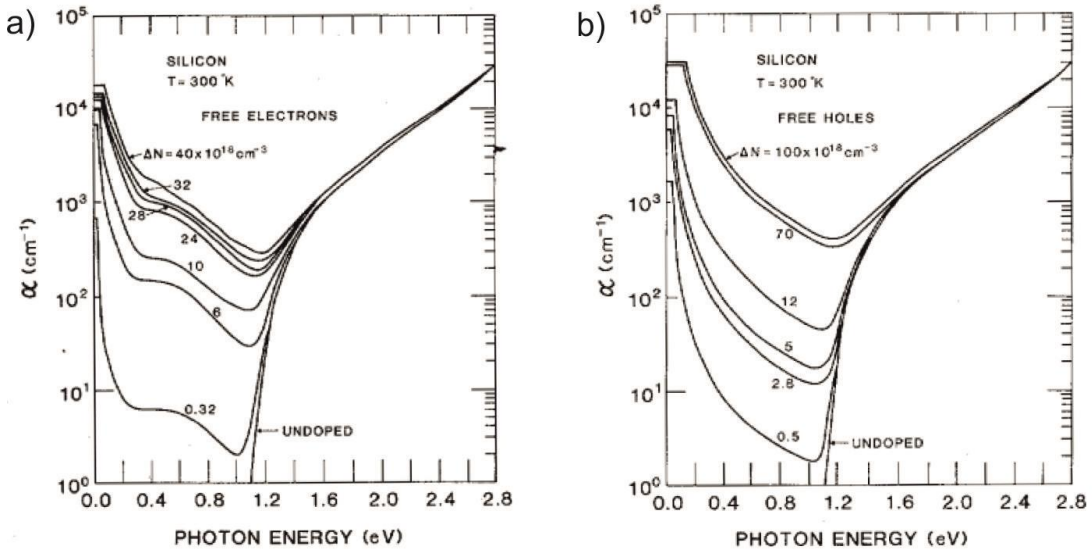

Fig. 2.14. Absorption spectra of doped silicon wafers reproduced from [41], for a) n-type Si, b) p-type Si. The wavelength is plotted on the horizontal axis in terms of photon energy (eV), and the vertical axis shows the absorption coefficient, α (cm^{-1}). Each figure shows a number of curves for different doping concentrations.

2.6. Literature review summary

In this chapter the existing literature relating to mid-IR photonic components has been explored, and the use of group-IV material platforms for realisation of these components has been justified. In order to determine which group-IV material platforms should be developed existing demonstrations of group-IV material waveguides have been reviewed. Modulation techniques in silicon and the passive components required

to create modulator devices have been discussed. Finally, it has been identified that there is a need to determine accurate equations describing the plasma dispersion effect at mid-IR wavelengths in silicon.

Chapter 3: MIR optical characterisation setup

This chapter is concerned with the assembly of an experimental setup for integrated photonic device characterisation at λ=3.8μm. An apparatus that is common to optical testing of both passive and active integrated components is described here. Additional details regarding electrical testing equipment for modulation measurements are given in chapter 6.

3.1. Basic operation

The assembly of an experimental setup capable of characterisation of waveguides and other integrated photonic devices at mid-infrared wavelengths is a non-trivial task due to relatively recent availability and high cost of all of the key optical components required. Equivalent components used in the visible and NIR in most cases cannot be used.

An experimental setup has been assembled for device testing at 3.8μm, of which block diagrams are shown here in fig. 3.1 and fig. 3.2, corresponding to butt and grating coupling configurations, respectively.

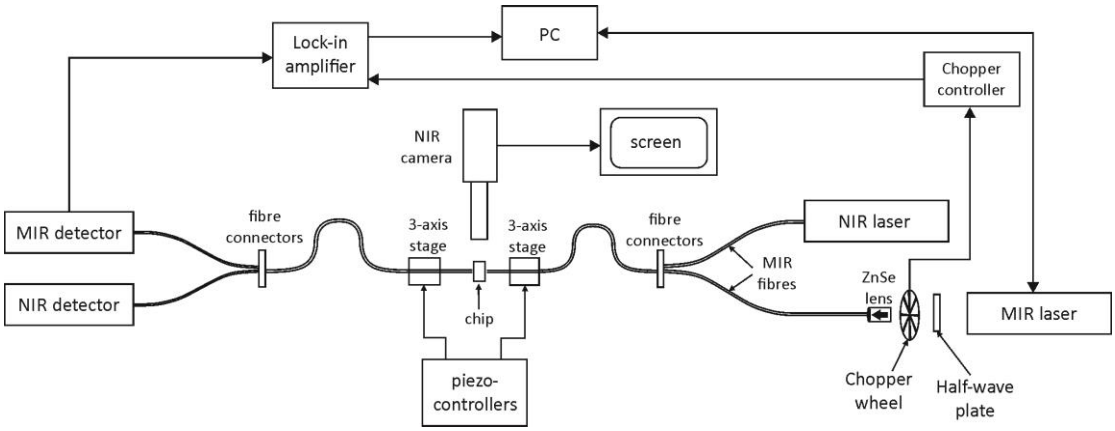

Fig. 3.1. Block diagram of MIR optical characterisation setup, when configured for butt coupling.

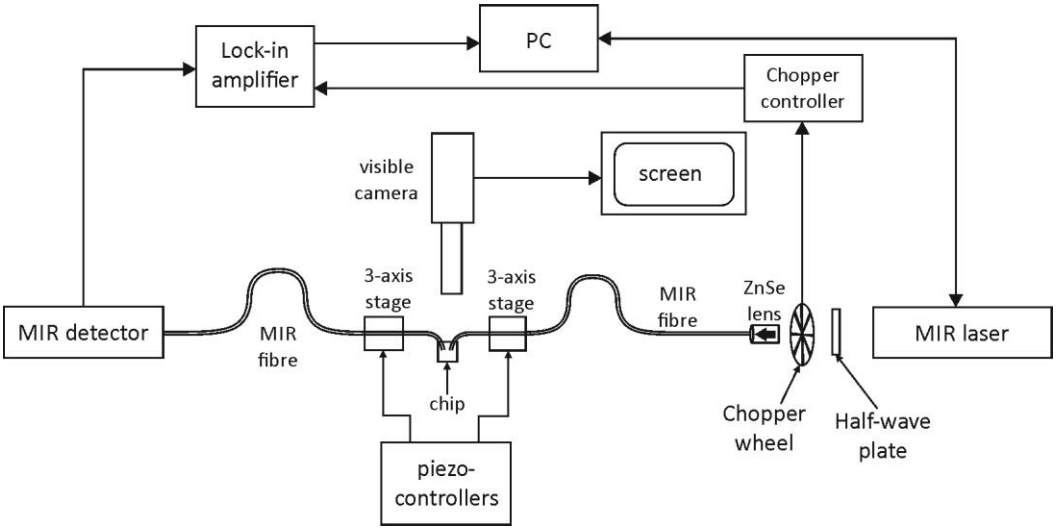

Fig. 3.2. Block diagram of MIR optical characterisation setup, when configured for grating coupling.

A tunable quantum cascade laser (QCL) operating in the wavelength range 3.72-3.90µm is used as the source. Light is coupled into optical fibres which have low optical loss in this range using a ZnSe lens (transmission range 0.5-20µm). Light is coupled from the fibres to the chip by either butt coupling, where the fibre is in the plane of the waveguides and is aligned to the waveguide facet, or by coupling via grating couplers, where the fibres are almost normal to the surface of the chip.

The sample is placed on a stage, and the optical fibres are supported by three-axis stages which can be controlled manually for rough alignment or by piezo-controllers for fine control. For butt coupling, a NIR camera with a magnifying lens tube is placed above the sample stage, and the camera output is displayed on a screen, showing a top view perspective of the sample. Fig. 3.3 is a labelled photograph showing this arrangement. Approximate alignment is first performed by visually aligning both input and output fibres with the waveguide using the camera output. To ensure light is entering the waveguide, light from a broadband NIR laser (max. 20mW optical power) is first launched into the fibre, as reflection of the NIR light at the waveguide facet can be seen by the NIR camera. In this way it is possible to see when light has entered the waveguide. To maximise the coupling efficiency the power output is read off the NIR detector, and fibre positioning is optimised using the piezo-controllers. The input into the fibre is then

switched from NIR to MIR light using fibre connectors, following which the fibre position is further adjusted for optimised MIR light coupling.

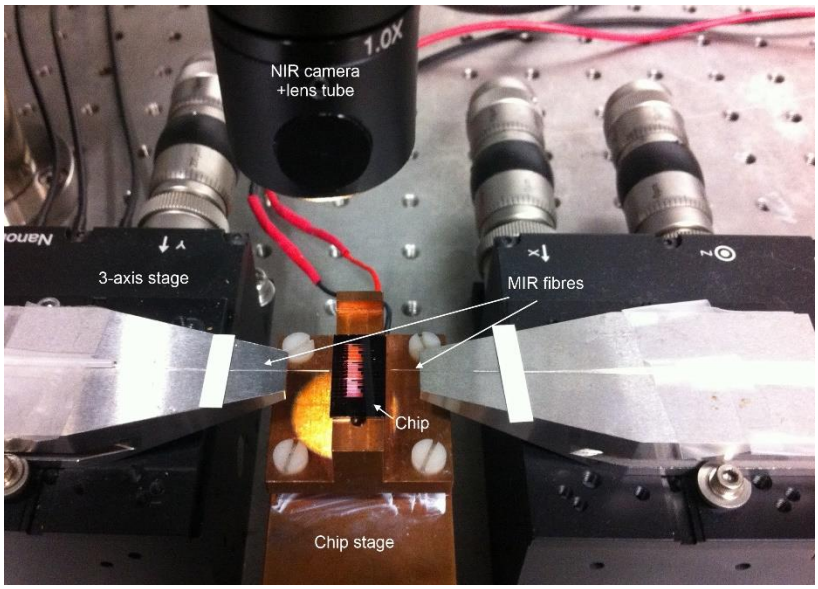

Fig. 3.3. Labelled photograph of butt coupling alignment apparatus.

For out of plane coupling a visible light camera with a magnifying lens tube is placed at approximately a 45° angle to the chip, as shown in fig. 3.4. From this angle the position of the fibre in all 3 dimensions can be determined accurately enough to perform initial alignment. Coupling via grating couplers can be more tolerant to initial misalignment than butt coupling. There is also no need to use a NIR source as alignment is carried out by monitoring the MIR signal output.

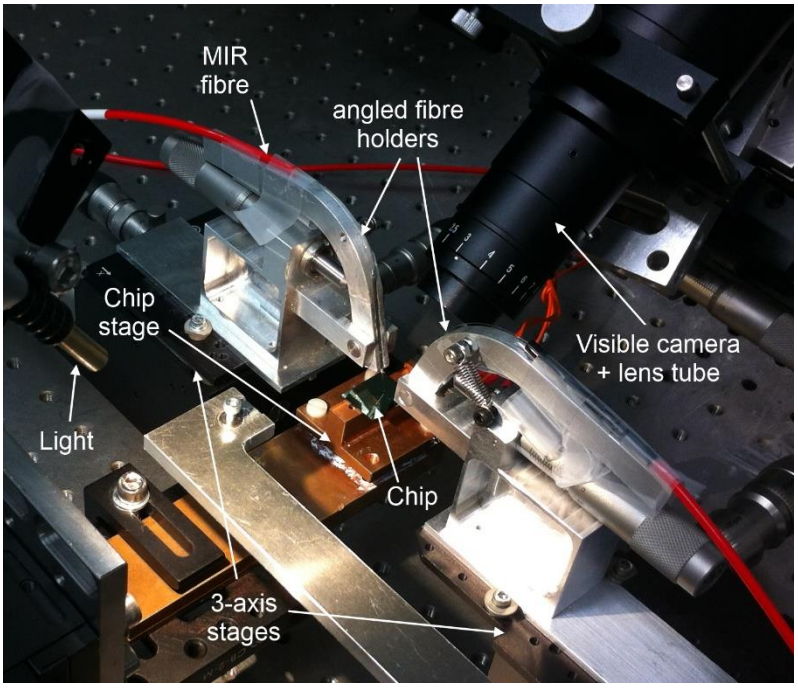

Fig. 3.4. Labelled photograph of grating coupler alignment apparatus.

Light is coupled back into a fibre, using the same methods, and this output fibre leads to a detector. The output end of this fibre is secured on a 3-axis stage in front of a mid-IR detector so that the detected power can be maximised.

3.2. Equipment details

3.2.1 Quantum cascade laser

The quantum cascade laser is custom made by Daylight Solutions [1], and operates at 3.72-3.90µm in either continuous wave (CW) or pulsed modes. The laser temperature is maintained at 21°C by a chiller, which circulates coolant (water/isopropanol mixture) through the laser casing. The maximum CW optical output power of the laser is ~150mW, at its peak wavelength of 3.80µm. The QCL optical output spectrum is shown in fig. 3.5. The nominal tuning accuracy is ±0.5cm^{-1} (±1.9nm at λ=3.8µm), and the nominal linewidth is ±0.003cm^{-1} (±11pm at λ=3.8µm). The laser is not mode-hop free, which during operation manifests as significant jitter of the laser wavelength (approx. ±1nm wavelength variation). The laser current, which determines its optical power, and

wavelength are controlled via a laser controller supplied by the manufacturer, which can in turn be controlled from a PC using a LabView [3] program.

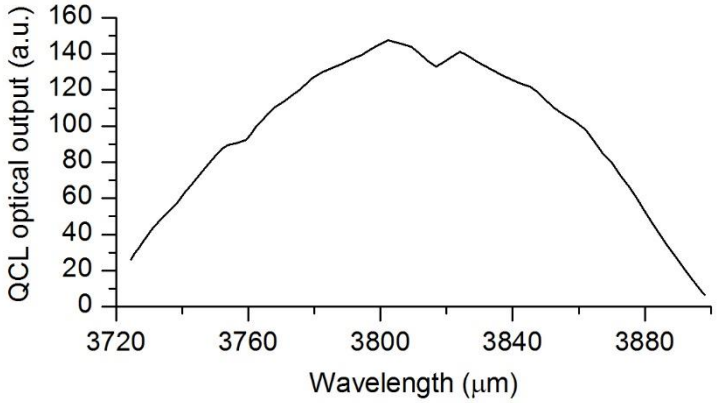

Fig. 3.5. QCL output power plotted against emission wavelength, data provided by Daylight Solutions.

In all measurements where wavelength scans of the transmission through a device is measured its transmission is normalized to that of a straight waveguide, in order to remove the wavelength dependence of the QCL output and of any other wavelength dependent features of the setup.

3.2.2 Detector

An InSb detector is used for detection of MIR light, which is model IS-1.0 from InfraRed Associates Inc., and its detectivity spectrum is shown in fig. 3.6 below.

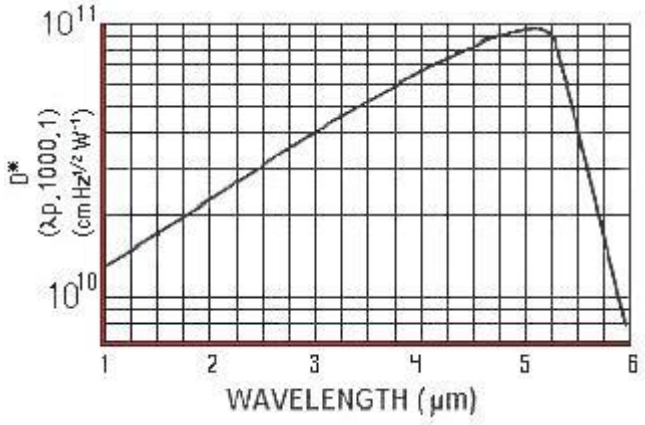

Fig. 3.6. InSb detector detectivity spectrum, reproduced from [4].

The detector is cooled by liquid nitrogen, which is poured into the detector packaging, and must be replenished every 12 hours during use. The detector bandwidth can be

calculated from its time constant τ, which according to the manufacturer is <1µs. The 3dB bandwidth is then given by $f=1/2\pi\tau$=159kHz.

3.2.3 Optical fibres and fibre preparation

The fibres used are fluoride based MIR single mode fibres from IRPhotonics [5], now part of Thorlabs [6], which are capable of supporting single mode light in the spectral range from 300nm to 4100nm. They are brittle, so great care must be taken during alignment so as not to damage them.

Before the fibres can be used they must be stripped of several cladding layers and cleaved to create a high quality facet. The stripping/cleaving process is as follows:

a. The external coating of the fibre, which is approximately 4mm in diameter, is cut away using a scalpel.
b. The next layer is a white buffer layer, 800µm in diameter. This is removed using a Miller type fibre stripper.
c. The final coating layer has a 250µm outer diameter and 125µm inner diameter. It is brittle, and before it can be stripped it is dipped in dichlormethane for ~15s. The layer can then be stripped, carefully, using Miller type fibre strippers. This reveals the bare fibre cladding (125µm diameter) and core (9µm diameter)
d. The bare fibre is cleaved using a York FK11 fibre cleaver. The fibre is secured in two clamping levers, then tension is applied to the fibre by pulling a lever which moves the two clamps apart. Finally, a lever is pulled which allows a diamond blade to move and cleave the fibre. The diamond blade and fibre holder must be clean during this process, and can both be cleaned using isopropanol.

3.2.4 Polarisation control

For many experiments it is important to be able to control the polarisation of light that is being coupled into a chip. The QCL laser emits light that is TM polarised (>100:1, TM:TE) relative to the plane of the chip when it is placed flat on a surface, but it has been mounted so that it is rotated by 90°, so that it emits TE polarised light, relative to the chip. A half-wave plate can be placed in the free space between the QCL output and the input fibre, which can be used to rotate the light beam polarisation. For example, if a 0° angle corresponds to maintaining TE polarisation, then rotating the half-wave plate by 45° rotates the light polarisation by 90°, from TE to TM polarisation. The half-wave plate is made from cadmium thiogallate ($CdGa_2S_4$), which has a material transparency range of 0.47-9.5µm. The half-wave plate is custom made by Altechna [6] to have a central wavelength of 3.8µm, and has an antireflection coating in order to minimise reflections back into the laser.

3.2.5 Signal processing

In the mid-infrared there can be a high degree of background noise stemming from thermal radiation, so signal processing methods are used to improve the signal-noise ratio. There is a chopper between the laser and lens that creates a square signal. The detector output signal first passes through a pre-amplifier, and then to a lock-in amplifier (Signal Recovery SR7265). The lock-in amplifier is also connected to the chopper, so that it can lock onto the square wave signal in the detector output. Using a lock-in amplifier in this way improves the signal to noise ratio, effectively acting as a filter for a signal at the chopper frequency.

The lock-in amplifier and QCL controller are both linked to a PC by GPIB cables, and a LabView program has been written that allows for the laser output wavelength to be scanned while recording the measured transmission from the lock-in amplifier. Labview programs provided by the manufacturers for both of the components were altered so that they could be controlled by an external script.

Chapter 4: Mid-IR waveguides

In this chapter demonstrations of three types of waveguides at the 3.8µm wavelength are presented: i) silicon-on-insulator (SOI) waveguides, which are expected to have good prospects for devices for wavelengths up to approximately 4µm, ii) poly-Si on SOI waveguides, which can be fabricated in silicon foundries alongside NIR silicon photonics components, and iii) germanium-on-silicon waveguides, which are expected to have a much wider transparency range, potentially even to λ=16µm [1].

4.1. Waveguide propagation loss measurements

For all of the presented waveguides the propagation loss is measured using the cut-back method, where waveguide structures of different lengths are defined on the same chip. By measuring the optical transmission through waveguides of different lengths, the power loss per unit waveguide length can be determined. Figure 4.1 shows an example of the mask pattern used to vary this length. This is a reliable method as it normalises the waveguides against each other, removing the influence of factors such as bend losses, coupling method and optical loss in the rest of the system.

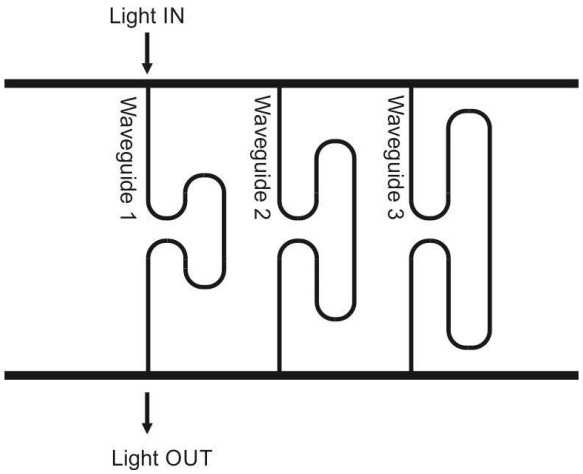

Fig. 4.1. Diagram showing top view of the waveguide layout used for measurement of waveguide loss using the cut-back method. The waveguide length is varied while all other sources of loss are kept constant.

Another way of performing this measurement would be to define entirely straight waveguides on the chip and to shorten the waveguide length by polishing the chip back. However, this can introduce error through varying end facet quality due to polishing, or a change in the experimental setup between successive measurements. The following equation can be used to calculate waveguide loss [2], when the optical transmission through two waveguides of different lengths is known:

$$\alpha = \left(\frac{1}{L_1 - L_2}\right) \ln\left(\frac{I_2}{I_1}\right) \qquad \text{Eq. 4.1}$$

Where α is the propagation loss (cm^{-1}), L_1 and L_2 are the lengths of the two waveguides (cm), and I_2 and I_1 are the measured transmissions for those lengths. With a number of measured points, a graph of normalised optical loss (dB) against propagation length (cm) can be plotted, and the gradient of the line of best fit will give an estimate of the waveguide loss in dB/cm.

4.2. Simulation methods

To aid the design and optimisation of waveguide geometry the commercial photonic simulation packages RSoft Beamprop [3] and Photon Design Fimmwave [4] were used. The simulation methods used in the two software packages are briefly introduced here. Both simulation methods are used as mode solvers, to find the eigenmodes of the waveguide, and both are commonly used for SOI waveguide simulations in the NIR (e.g. [5-9]).

4.2.1 RSoft Beamprop

Beamprop is based on the Beam Propagation Method (BPM), in which the wave equation (Eq. 2.1) is solved approximately for a particular refractive index geometry of the waveguide under a paraxial assumption, i.e limiting propagation to a small range of angles [11]. In Beamprop the BPM can be combined with either the imaginary distance method or the correlation method to find the propagation constants of the modes. The imaginary distance method is more efficient, but the correlation method is more accurate for lossy waveguides [11], and therefore the correlation method is used for the

simulations in this chapter. Inaccuracies in using Beamprop can arise due to the paraxial assumption, because it leads to errors from material platforms with high refractive index contrast. Nevertheless, the software can be conveniently used to approximate the single mode condition width for particular waveguides.

4.2.2 Photon Design Fimmwave

The Film Mode Matching (FMM) solver in Fimmwave, which is based on Sudbo's FMM method [12] has been used for many of the simulations carried out in this project, and is expected to be more accurate than Beamprop by RSoft. The FMM solver divides regions of the waveguide into rectangular homogenous sections. One dimensional (1D) mode solutions are fitted to the different sections of the waveguide, following which continuous boundary conditions are imposed to find a complex vectorial solution that satisfies Maxwell's equations at all points in the waveguide [13, 5, 12]. This method works best for rectangular waveguide geometry [13]. The drawback for using the solution in this work is that finding the number of propagating modes in a waveguide for a particular device width requires manual input, so conducting a scan of the waveguide widths for a varying parameter is much simpler using Beamprop.

4.3. Silicon-on-insulator waveguides

Although SOI waveguides have been thoroughly studied in the NIR, at longer wavelengths their design and performance has yet to be investigated carefully. Waveguide dimensions and sources of loss change with wavelength.

For experimental demonstration of mid-infrared SOI waveguides two routes to fabrication were pursued. The first was a limited fabrication run at the University of Glasgow, in collaboration with Dr. Michael Strain and Dr. Marc Sorel. The second was "in-house" chip fabrication at the University of Southampton.

4.3.1 Design

The critical dimensions to consider in the design of SOI waveguides are the Si device layer thickness (H), BOX layer thickness (H_{BOX}), Si etch depth (D), and waveguide width (W), as shown in fig. 4.2. The same variable names for waveguide width, height and etch depth will also be used to describe waveguides based in all other material platforms throughout this chapter.

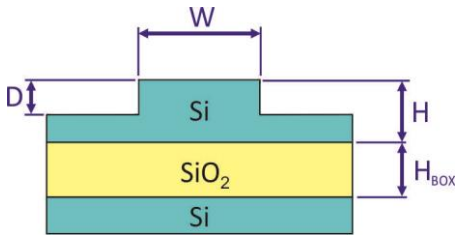

Fig. 4.2. Diagram of SOI waveguide cross-section, showing dimensions to be optimised.

4.3.1.1 Waveguide height

As was discussed in the literature review section, there are major advantages to choosing material platforms that maintain compatibility with NIR silicon photonics. Currently wafers with 220nm and 400nm thick Si layers are popular, and as a result such wafers are easily available, for example from SOITEC [14]. However, the Si thickness has a large impact on the waveguide loss and on the range of wavelengths that can be supported by the waveguides; a thin Si layer will cut-off propagation at longer wavelengths. Figures 4.3a and 4.3b show the results of simulations of SOI strip waveguides at wavelengths between 1.5μm and 4.5μm for TE and TM polarisations, for waveguides with heights of 220nm, 300nm, 400nm and 500nm. The simulation is restricted to Si layers $\leq$ 500nm, because affordable procurement of SOI wafers with greater Si layer thickness and tolerable thickness variation is difficult.

The two figures show the width at which the first higher order mode appears at different wavelengths, i.e. the width of the single mode condition. The waveguide loss at the single mode condition width has also been calculated at each wavelength, and at wavelengths where the waveguide loss is calculated to be >1dB/cm no points have been

plotted. As the waveguide loss decreases with increased width the transmission range of waveguides with each Si height is represented in this way. The simulation was performed using the RSoft Beamprop simulation software package, and took into account the material absorption of SiO_2. Data for the absorption coefficient of SiO_2 was digitised from fig. 4 of [1]. The simulation includes losses from radiation and material absorption, but does not include scattering losses from surface roughness. For the simulation a 0.04µm × 0.04µm x-y grid was used, the step between simulation wavelengths was 0.25µm across most of the range, and 0.05µm at the upper limits, and the waveguide width step was 0.025µm. The lines between simulated points do not form perfectly smooth curves due to the resolution used in the simulation, which was chosen for reasonable simulation times.

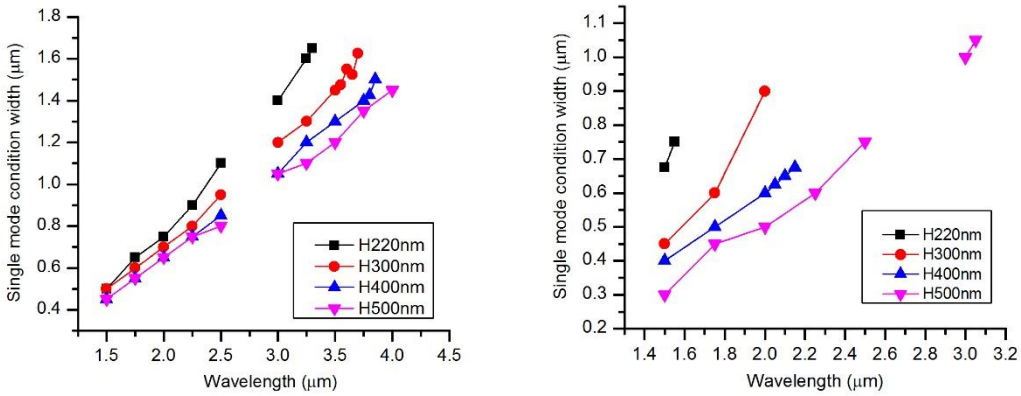

Fig. 4.3. Single mode condition widths for SOI waveguides with different Si layer thicknesses at wavelengths between 1.5µm and 4.0µm. a) TE polarisation b) TM polarisation.

For all Si thicknesses and both polarisations there is no point plotted at λ=2.75µm, where the material absorption of SiO_2 is very large. For TE polarisation the propagation loss rises above 1dB/cm at a wavelength between 3.25µm and 4.25µm for all Si thicknesses, with the H_{Si}=220nm line stopping at λ=3.30µm, and the other lines stopping at progressively longer wavelengths for greater H_{Si}. For TM polarisation with H=220nm there is only propagation in the NIR, but increasing the height greatly extends the range of low loss propagation.

As the wavelength increases the confinement of the optical mode in the waveguide core decreases, leading to increased radiation loss. While radiation loss is the dominant loss

mechanism in these simulations, the overlap of the optical mode with SiO_2 also increases, so at wavelengths where SiO_2 absorption is high this has a large effect.

It is clear that using a greater waveguide height allows transmission over a wider range of wavelengths. For compatibility with NIR silicon photonics design SOI wafers with 400nm thick Si layers will mostly be used in this work for MIR SOI components, though 500nm thick Si will also be used for the demonstration of some components.

4.3.1.2 Etch depth

In the literature review the trade-offs in choosing waveguide etch depth were discussed; namely, that using a deep etch increases lateral optical confinement, reduces minimum bend radii, therefore increasing device integration density, whereas using a shallower etch reduces the etched sidewall surface, so scattering from surface roughness is reduced. Additionally, in order to be able to integrate waveguides into a modulator structure based on the plasma dispersion effect rib waveguides need to be used.

Ultimately, the overriding consideration in choosing an etch depth for device fabrication was maintaining compatibility with existing fabrication processes and recipes at the two fabrication centres, which reduced fabrication costs through the sharing of fabrication runs and increased the likelihood of reliable and precise fabrication. For waveguides fabricated at the University of Glasgow the etch depth was 350nm, and for those fabricated at the University of Southampton the etch depth was 220nm.

4.3.1.3 Waveguide width

Increasing the width of the waveguide is expected to reduce both radiation losses and surface roughness scattering losses. In the case of scattering loss, creating a narrower waveguide where optical confinement is lower increases the interaction of the optical mode with the surface roughness. However, if the waveguide is too wide undesirable

higher order modes will be allowed to propagate, so simulations must be used to estimate where the balance between these two considerations lies.

Initial simulations for single mode condition (SMC) determination have been performed using RSoft Beamprop, and verified using Photon Design Fimmwave software. Figures 4.4a and 4.4b show the relationships between the real part of the refractive index and the waveguide width for the fundamental and first higher order modes, simulated using Beamprop, for waveguides with D=350nm and 220nm respectively. In both cases λ=3.8μm, H=400nm and H_{BOX}=2000nm. At the widths where the mode solver found no 1st order mode no points are drawn. The simulations were conducted for widths in the range 0.9μm-2.0μm. The absorption coefficient of SiO_2 was taken to be 5.3dB/cm [1] for the simulations.

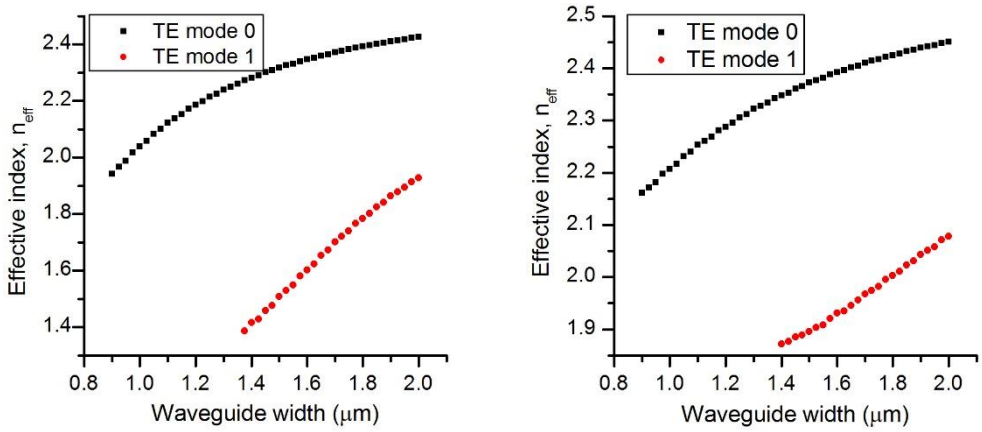

Fig. 4.4. Beamprop mode simulation for SOI waveguides with H=400nm, H_{BOX}=2000nm, and in a) D=350nm, and b) D=220nm. The figures show the widths at which the 1st higher order mode (red points) can propagate.

From fig. 4.4a it can be seen that for D=350nm the first higher order mode appears at W>1.35μm, while for the shallower 220nm etch the higher order mode appears for W>1.4μm. The simulations predict that shallower etched waveguides have a wider SMC width, agreeing with the expectation that rib waveguides can be designed to be larger for single mode propagation. Fig. 4.5a. shows the propagation loss with varying waveguide width for D=220nm waveguides that has been simulated using Fimmwave. The simulation includes losses from SiO_2 absorption and from mode leakage into the

silicon substrate, and in fig. 4.5a the losses with and without substrate leakage are shown. For the Fimmwave simulation, in order to take into account the substrate leakage, perfectly matched layers (PMLs) are placed at the boundaries of the simulation window through which leakage occurs. Due to a peculiarity of the software PMLs can only be placed at the left and right boundaries of the simulation window, therefore the waveguide definition is rotated by 90°, so that the PML layers are placed along the Si substrate and air top cladding boundaries.

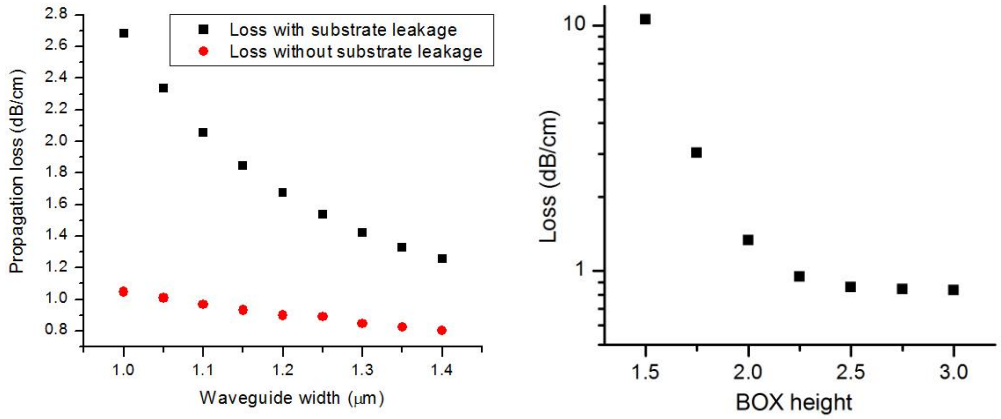

Fig. 4.5. Fimmwave mode simulations for SOI waveguides with H=400nm, D=220nm and H_{BOX}=2000nm at λ=3.8μm. a) Waveguide width vs. propagation loss, showing loss from material absorption only (red circles) and material absorption and substrate leakage (black squares). b) Total propagation loss vs. BOX thickness.

Loss due to both material absorption and substrate leakage decrease with increasing waveguide width, which indicates that in narrower waveguides a greater proportion of the optical mode propagates through the BOX layer. Additionally, when the loss of a waveguide with W=1100nm, H=400nm, H_{BOX}=2000nm and D=350nm is simulated, the loss is calculated to be 5.3dB/cm, which is significantly larger than the 2.1dB/cm simulated for a waveguide with the same dimensions but a shallower H=220nm etch depth, with most of this difference in loss being due to increased substrate leakage. In fig. 4.5b the propagation loss has been plotted as a function of BOX layer thickness, for waveguides with H=400nm, D=220nm and W=1350nm. The waveguide loss decreases rapidly with increasing BOX thickness, as substrate leakage becomes smaller with a larger insulating layer, until it approaches a steady value of 0.84dB/cm for H_{BOX}>2.5μm, which is the loss due to SiO_2 absorption. Clearly the 2μm BOX of the wafers that are used

for NIR silicon photonics at the two fabrication centres is not thick enough to completely suppress substrate leakage at λ=3.8μm.

The conclusion that is taken from the simulation results is that the waveguides should be made as wide as possible, while still satisfying the single mode condition. Because limited chip space was available for the Univ. of Glasgow fabrication run only one waveguide width could be investigated, and this was chosen conservatively to be 1100nm, so as to ensure single mode propagation even with potential simulation inaccuracies. For waveguide fabrication at the Univ. of Southampton, using the deeper 220nm etch, there was not the same limit on chip space, therefore the mask design included cut-back loss measurement sections for 1.1μm<W<1.35μm.

4.3.1.4 Mask design

The chip layout design for both waveguides and all other components discussed throughout this report was carried out using a combination of the L-edit layout design software package [15] and a set of C++ functions developed for this project for drawing generic integrated photonic components, and systems of components. The C++ functions interface to L-edit as macros that can be called from the program, where all device parameters are defined within the C++ code. By taking this approach drawing complex layouts with a large number of device dimension variations was accelerated.

4.3.2 Fabrication

The process flow for SOI waveguide fabrication at the University of Southampton is described here, and the same process flow is used for fabrication of SOI components in later chapters. Layout design was carried out by myself. Dr. Ali Khokhar converted the mask layout to e-beam file type and carried out e-beam lithography. Dr. Stevan Stanković, Dr. Colin Mitchell and Scott Reynolds performed the initial wafer clean, alignment mark writing, and silicon etching processes. Callum Littlejohns carried out wafer dicing. Polishing and final chip cleaning were carried out by myself.

i. *Layout design and conversion to e-beam file type:* The layout was designed using L-edit and proprietary software, as described above, and exported to the GDS-II file format. To prepare the design for writing by the e-beam machine BEAMER software by GenISys [16] was used to convert the file to the .V30 file type. This is a powerful software tool that can be used for simple functions such as logic and editing operations on design layers, and is also used to specify details such as e-beam resolution, spot size, spot separation, e-beam dose and proximity correction for different parts of the design. For example, a "sleeving" technique is used to specify a smaller spot size, and therefore higher resolution, at the edges of waveguide structures, in order to reduce writing time while maintaining high lithography accuracy.

ii. *Initial wafer clean:* The wafer is cleaned prior to any processing. First an RCA1 clean (NH_4OH:H_2O_2:H_2O mixture, ratio 1:1:5) is performed to remove electrostatically held particles from the wafer surface, followed by an RCA2 clean (HCl:H_2O_2:H_2O mixture, ratio 1:1:5), which etches away any metal surface contaminants. These two treatments create a thin SiO_2 layer on the Si surface, which is removed by dipping the wafer in buffered HF (1:20 HF:NH_4F) solution for 1 min.

iii. *Writing alignment marks for e-beam lithography:* For the e-beam to be able to write all parts of the layout in the correct positions relative to each other alignment marks must first be present on the chip. To do this optical lithography is first performed which defines cells, with alignment marks in the corners, across a whole wafer. S1813 positive photoresist is first spun onto the wafer, then optical lithography using a contact mask aligner is performed. After exposure MF319 (non-metal containing) developer is used to develop the exposed photoresist, and excess photoresist is washed off in DI water. Finally the silicon is etched in an ICP (Inductively Coupled Plasma) etcher to a depth of approximately 300nm, so that there is still a layer of Si remaining. It is not etched all the way through in order to prevent underetching of the Si in any possible subsequent SiO_2 etching steps, which could cause a collapse and loss in fidelity

of the alignment mark patterns. The ICP silicon etch uses SF_6 (25sccm), C_4F_8 (45sccm) chemistry, at a pressure of 15mTorr and 15°C temperature. After etching all remaining photoresist is cleaned off using a fumic nitric acid (FNA) clean, and DI water rinse.

iv. *Electron-beam lithography:* ZEP 520A photoresist is spun onto the wafer at 6000rpm, which creates a 265nm thick photoresist layer. Following spinning the wafer is baked at 180°C for 3 minutes. The wafer is written in the JEOL JBX-9300FS e-beam machine. A typical writing time is 15 minutes for a 3cm x 2cm chip filled with waveguide structures. After lithography the wafer is submerged in ZEDN50 developer for 2 minutes, and the sample is rinsed in IPA and blow dried with N_2.

v. *Silicon etching:* The silicon is etched in the ICP using the same recipe as for the alignment mark etch, described above. After etching the remaining ZEP photoresist is removed from the wafer using the FNA strip and clean process.

vi. *Chip dicing:* After lithography and etching steps are complete the wafer is diced into chips using the LoadPoint MicoAce Series 3 dicing machine. Dicing a wafer offers much greater control compared to cleaving the wafer. Before dicing a layer of protective S1813 photoresist is spun onto the wafer, and the wafer back surface is affixed onto a sheet of plastic with one adhesive side. This is then secured into a wafer supporting ring, which holds the wafer when it is placed in the dicer.

vii. *Chip polishing:* If grating couplers are defined on the chip then dicing is the last processing step, but if butt coupling is used then the chip end facets must be cleaved or polished. Cleaving is fast and can produce good quality facets, but is very unreliable, and the whole chip may even be damaged. Polishing can be time consuming and there can be inconsistency between waveguide facets on the same chip, but is often the best preparation method when grating couplers for a particular material platform and wavelength have not yet been developed.

Polishing is performed by lapping with rotating abrasive discs against the chip edge, thus smoothing the chip facet. A Metaserv 2000 Grinder/Polisher machine is used for this polishing.

For protection while polishing a protective layer should be applied to the chip surface, for example a thick photoresist layer could be spun onto the chip. For this project Buehler mounting wax has been used for this purpose. Both the chip and the wax must be heated, as the wax begins to melt at approximately 80°C, and is quite liquid at temperatures above 110°C. The sample is placed on a hot plate set to this temperature, and wax is melted, then applied to the chip surface using a toothpick, or some similar implement. It is important for the wax to be spread evenly across the surface of the chip, otherwise parts of the wax can break off and cause damage to the chip facets while polishing. The wax can be removed after polishing by submerging the sample in acetone for 2 minutes.

The chip back surface is affixed using the same wax and wax application process onto a metal block that has been specifically machined to act as a support during polishing. When the wax is cooled it acts as a strong adhesive between the chip and support. A piece of "dummy" silicon wafer is similarly attached to the opposite side of the support, to act as a balance. The photograph labelled Fig. 4.6 shows a labelled example of what the chip holder looks like with a test chip and "dummy" chip attached:

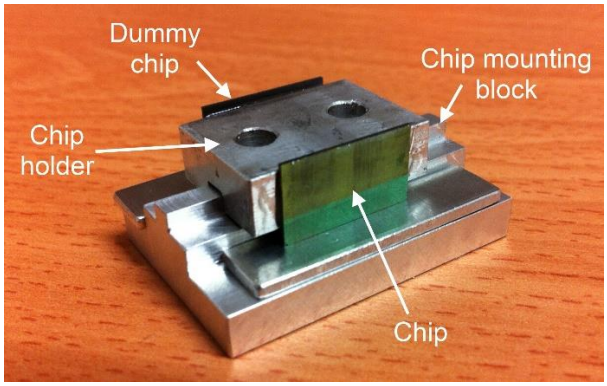

Fig. 4.6. Photograph of chip ready for polishing and dummy chip mounted onto chip holder and mounting block

The edges of the test chip and "dummy" chip must be parallel to each other for even polishing, and there should be the same overhang past the chip holder edge for both.

The purpose of this is to support the chip so that it is perpendicular to the abrasive discs. An abrasive disc is fastened to the surface of the polishing wheel, and the sample holding arm is lowered into place just above the surface of the wheel. The chip holder and chip are placed into one of the holes in the sample holding arm so that the chip facet to be polished is perpendicular to the abrasive disc surface, and so that the chip face is facing the direction of the oncoming disc while the wheel is spinning. A sprung rod is pushed down onto the top of the chip holder to hold the chip firmly in place.

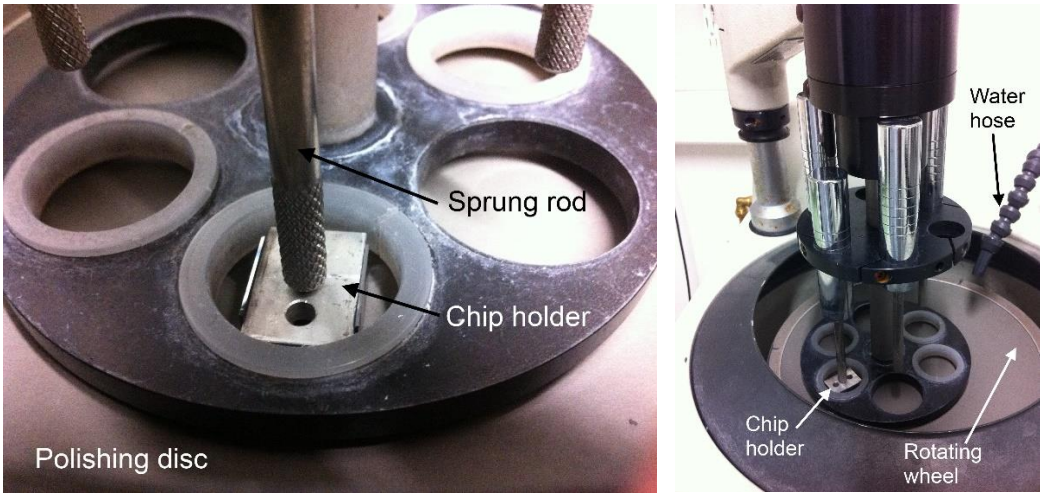

Fig. 4.7. Chip mounted in polishing machine.

When the chip has been secured in place the rotating wheel can be switched on. The wheel is set to spin at 50rpm, which is the slowest setting possible. A supply of water pours onto the surface of the polishing disc throughout polishing to serve as a lubricant. The abrasive discs that are used are silicon carbide for the rougher polishing, and AlO_2 for smoother polishing. Progressively smoother discs are used throughout polishing.

The devices that were fabricated at the University of Glasgow followed a similar process flow. E-beam lithography was again used for pattern definition. Here a Hydrogen

Silsesquioxane (HSQ) negative tone photoresist was used. The sample was etched using an ICP etcher, also with $SF_6\backslash C_4H_3$ chemistry, with the HSQ photoresist acting as a hard mask. The etch depth was controlled using an interferometric monitor. The HSQ mask was removed after etching by dipping the sample in Hydrofluoric acid (HF). Finally, the sample was mechanically scribed and cleaved to provide access to the waveguide facets.

4.3.3 Characterisation

Both types of fabricated SOI waveguides were characterised using the MIR setup described in chapter 3, in the 3725-3899nm wavelength range. For convenience, in this section the waveguides fabricated at the University of Glasgow will be referred to as type SOI_A, and those from the University of Southampton as type SOI_B.

Type SOI_A were designed to be characterised by butt coupling to the chips, and all waveguides were terminated by 10μm wide waveguides that were connected to the single mode waveguide sections by 1.25mm long linear tapers. Type SOI_B chips were designed with grating couplers with the following dimensions, which were designed by Dr. Xia Chen: grating period = 1.96μm, duty cycle = 50%, grating coupler length = 50μm, grating coupler width = 20μm, and taper length = 1mm.

Typical measured transmission when aligned to the waveguides by both butt coupling and grating coupling was approximately 20-30dB greater than the measured transmission when misaligned, which left little doubt that the fibres had been properly aligned. Fig. 4.8 shows a typical unprocessed spectrum of measured transmission through a SOI waveguide, in this case for type SOI_B waveguides with W=1350nm.

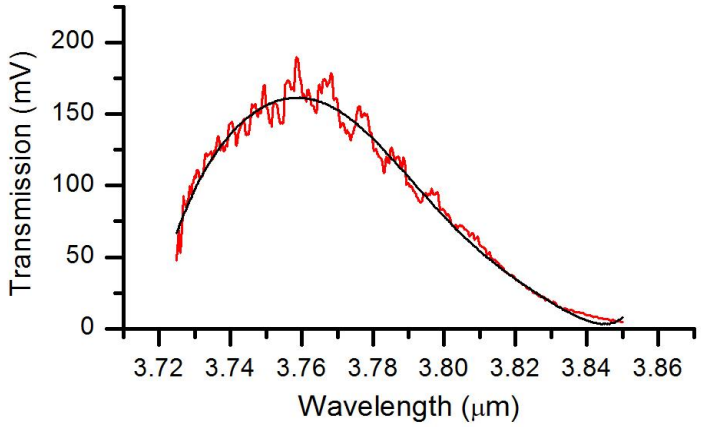

Fig. 4.8. Red line shows an example of an SOI waveguide spectrum measured using the QCL centered at λ=3.80μm. The black line is an order 10 polynomial that has been fitted to the experimental curve in order to filter out the high frequency components.

The figure is a typical example of the measured waveguide transmission spectrum in the range 3725-3850nm. Peak transmission is typically between 3740-3780nm, although peak laser output is at 3800nm. This is predominantly due to the fibre transmission spectrum, and is a characteristic of the experimental setup, such that reliable measurements at λ>3850nm are very difficult. There are also often quasi-periodic structures in the spectrum, that it is thought correspond to Fabry-Perot type resonances in various reflective cavities in the setup, for example between the laser output and fibre input. The laser output itself is another source of noise in the spectrum. The actual output wavelength of the laser is subject to jitter, and because the laser does not have "mode-hop free" behaviour there are small jumps in the laser wavelength during a scan. In order to circumvent this noise in the spectrum when calculating waveguide propagation losses, smoothing is used. This smoothing takes the form of fitting a high order polynomial (greater than order 10) to the spectrum, which reliably removes high frequency spectral components.

Figure 4.9 shows cut-back loss measurements for type SOI_A waveguides with W=1100nm. The transmission through the waveguides (shown on the y-axis) has been normalised relative to the transmission measured through the shortest waveguide, so as to remove the effects of coupling losses.

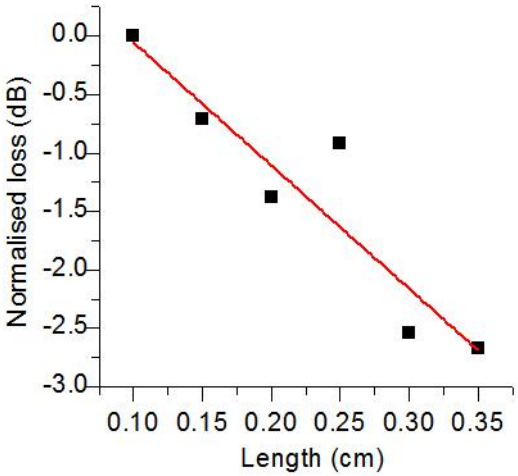

Fig. 4.9. Propagation loss measurement for SOI rib waveguide sample "SOI_A", with H=400nm, D=350nm, W=1100nm and H_{BOX}=2000nm. The measured propagation loss is 10.5dB/cm.

The experimental loss in the SOI_A sample was 10.5dB/cm, which is large compared to small SOI rib waveguides in the NIR. This is likely due to the conservative waveguide width that was chosen, and could be reduced by increasing the waveguide width nearer to the SMC width. The measurements on SOI_B samples corroborate this assessment.

For the SOI_B fabrication run there were not the same tight restrictions on chip space, therefore waveguides with widths between 1.1µm and 1.35µm were fabricated, and multiple chips with identical structures were made. Fig. 4.10. shows propagation loss measurements for SOI_B waveguides plotted against waveguide width.

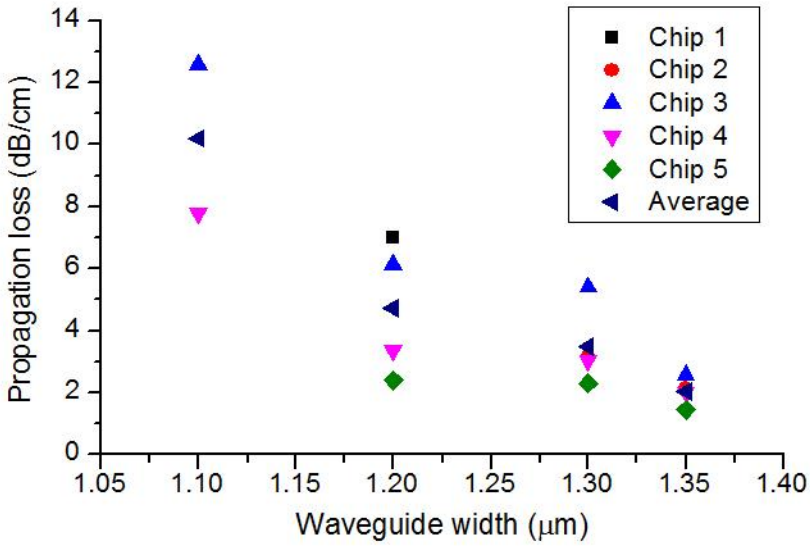

Fig. 4.10. Experimental propagation loss plotted against waveguide width for SOI waveguides with H=400nm and D=220nm.

It is clear from fig. 4.10 that the propagation loss increases dramatically with decreasing waveguide width. The average loss measured for waveguides with W=1.35µm, after 4 chip measurements, was 2.0dB/cm, with the lowest measured loss being 1.45dB/cm, for which the cut-back loss measurement is shown in fig. 4.11. For waveguides with W=1.1µm, the average propagation loss was 10.2dB/cm, which is similar to the 10.5dB/cm loss of the SOI_A waveguides that had the same width. It is also notable in fig. 4.10 that there is a large variation in the measured propagation losses for equivalent structures. It is thought that this is largely due to contamination of the wafer during fabrication, which introduced random defects into the defined structures.

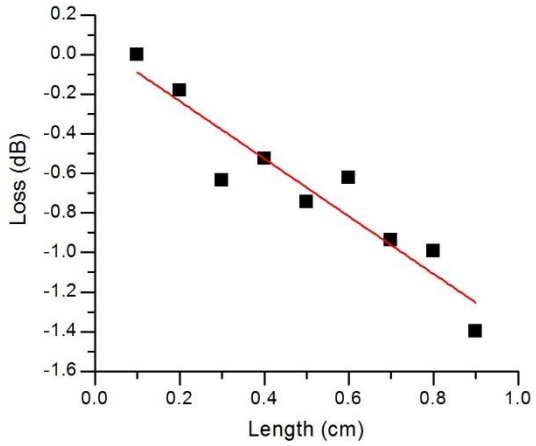

Fig. 4.11. Cut-back loss measurement for SOI rib waveguides with H=400nm, D=220nm, W=1350nm, and H_{BOX}=2000nm. Propagation loss for chip 5 = 1.45dB/cm.

It is useful to investigate what the sources of loss at this wavelength are. The Fimmwave simulations shown in fig. 4.5a predict much smaller losses, particularly in narrower waveguides, while neglecting loss due to scattering at the silicon/air interface. Together with the strong width dependence of the loss, this suggests that in narrower waveguides there is greater interaction of the optical mode with sidewall roughness, and therefore that scattering is the dominant loss mechanism. In comparing waveguide behaviour to that at another wavelength the contribution of scattering to the loss can be estimated. This same material platform (H=400nm, D=220nm, H_{BOX}=2µm) and identical fabrication method have been used to measure the loss of waveguides operating at λ=1.55µm by Dr. F. Gardes, Dr. Y. Hu, Dr. D. Thomson, Dr. A. Khokhar and Dr. S. Stanković. Single mode waveguides with W=450nm were measured to have losses of 5.4dB/cm. Fimmwave simulations that take into account the literature data for SiO_2 absorption predict that material absorption in the BOX layer and leakage to the Si substrate for W=1350nm waveguides account for 1.4dB/cm of the loss at λ=3.8µm, so that 0.6dB/cm stems from other sources (when total average loss =2.0dB/cm). Roughness scattering typically follows the λ^{-4} dependence of Rayleigh scattering, although it has been noted in the literature [17] that this dependence can change when a large proportion of a waveguide mode lies outside the waveguide core. Accurate modelling of scattering loss is complex [2] and can be computationally very demanding [18], therefore a detailed calculation of the scattering is considered to be outside the scope of this project. With a λ^{-4} dependence, assuming that all scattering occurs at the waveguide sidewalls, that an

equal proportion of the waveguide mode interacts with the sidewall roughness in each case, and that all loss at λ=1.55µm is due to scattering loss, working from the 5.4dB/cm loss figure at λ=1.55µm, the scattering loss at 3.8µm would be expected to be only ~0.15dB/cm. However, the assumption that an equal proportion of the waveguide mode interacts with the sidewalls in both cases is unsubstantiated, and the measurement accuracy is insufficient to determine accurately how large the loss due to scattering is. It is clear that increasing the wavelength can result in a significant reduction of waveguide loss. The simulations that were conducted also suggest that the waveguide loss could be further reduced by increasing the BOX thickness to >2.5µm.

4.4. Poly-Si on SOI waveguides

A second type of waveguides that has been investigated is a variant of SOI waveguides that is available through the *imec* (Leuven, Belgium) "Advanced Passives" process, which is a part of a pilot CMOS fabrication line, where a multi project wafer run service, intended for telecoms wavelength silicon photonics, is available to external researchers.

In this fabrication process components that use 220nm Si layer thickness can be combined with 400nm thick Si components, where this extra thickness is added by depositing poly-silicon onto the wafer surface. In NIR silicon photonics this is useful because it allows for compact, efficient devices that are based on 220nm Si to be combined with components such as couplers that are more efficient with 400nm thick Si [19]. This degree of flexibility in the platform potentially allows for MIR and NIR photonic components to be integrated on the same highly repeatable and commercially available material platform.

4.4.1 *imec* Advanced Passives fabrication process

The *imec* Advanced Passives fabrication process follows the steps listed here [20]:

i. The initial SOI wafer has a 220nm crystalline silicon (c-Si) layer on top of a 2000nm thick BOX layer.
ii. 5nm of thermal oxide is grown on the Si surface. This will serve as a protective layer for the c-Si in a subsequent a-Si etching step.
iii. 160nm of amorphous silicon (a-Si) is deposited by low-pressure chemical vapour deposition (LPCVD).
iv. 10nm of SiO_2 and 70nm of SiN is deposited on the a-Si surface by plasma processes, in order to serve as a hard mask for silicon etching, and also as a stop layer during chemical-mechanical planarization of the wafer surface.
v. The wafer is annealed at 560°C, converting a-Si into poly-crystalline silicon (p-Si).
vi. Waveguides are patterned by UV lithography (193nm), with a positive photo-resist.
vii. Waveguides are etched using halogen-based dry etch processes. At this stage there are three different etch steps available for waveguides that will be 380nm high, which are shown in fig. 4.12:
    I. 160nm etch into the stack. This etch stops at the 5nm thick SiO_2 layer.
    II. Two-step etch for etch completely through to the BOX layer. The first etch is the same as for option I, and following removal of the 5nm SiO_2 layer the second etch removes the c-Si layer.
    III. 220nm etch into the stack: this is also a 2-step etch process like option II, but the second etch is only a partial etch through the c-Si layer.

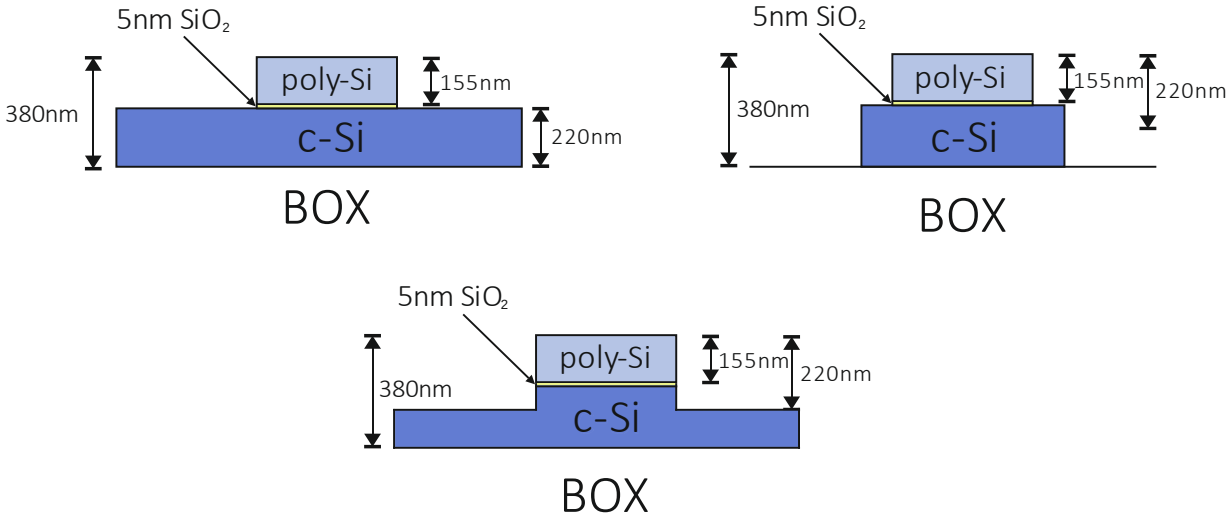

Fig. 4.12. Schematic diagrams of imec AP waveguide stack with a) 160nm etch into stack, b) 380nm etch into stack, and c) 220nm etch into stack.

viii. Remaining photoresist is stripped from the wafer, and SiO_2 is deposited across it. Chemical mechanical planarization is performed to flatten the wafer surface, stopping at the SiN layer, which remains on un-etched areas. In this way the etched areas are filled in with SiO_2. The SiN is stripped using hot phosphoric acid.

ix. Finally, a 1µm thick layer of SiO_2 is deposited to form the top cladding of the waveguides.

4.4.2 Design of *imec* Advanced Passives waveguides

For the design of waveguides compatible with this material platform there are only two degrees of freedom available: the etch depth and the waveguide width. In order to balance the requirements of low loss and small bend radius option III, in which a 220nm deep etch is applied to the 380nm high stack, has been chosen. A full etch through the stack would produce waveguides with high optical confinement, and therefore a smaller achievable bend radius, but at the possible cost of greater loss, sue to scattering at the sidewalls. Using only a partial etch reduces the size of the etched sidewall, and therefore reduces the scattering loss. Conversely, if a shallow etch is used the bend radius will be greater, and will increase the footprint of devices on the chip. Because of the high cost of device fabrication, it is important to minimise the footprint of structures. Additionally,

this is the same etch depth that is used for the c-Si 400nm high SOI waveguides fabricated at Southampton.

According to information provided by *imec* the refractive index of the p-Si can be assumed to be the same as for c-Si, so in the waveguide design there can be assumed to be a negligible difference between a fully crystalline waveguide core and the *imecAP* waveguide stack. As with the SOI waveguides, simulations have been performed to determine the greatest waveguide width at which the waveguide can safely be expected to support only the fundamental TE mode. There is only a very small difference between the SOI waveguide and *imecAP* waveguide heights, with the other significant difference being that a 1µm thick SiO_2 overlayer is deposited over the waveguides at the end of the process. Fig. 4.13 shows the real parts of the effective refractive indices of the fundamental and 1st higher order modes with varying waveguide width for *imecAP* waveguides with H=380nm, D=220nm and H_{BOX}=2000nm.

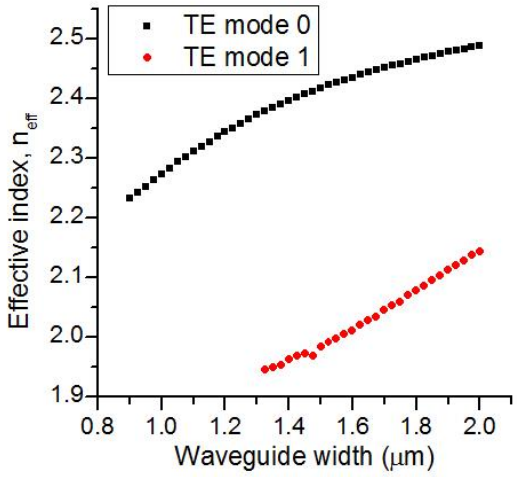

Fig. 4.13. Beamprop simulation of effective indices of fundamental and 1st higher order TE modes. 1st higher order mode is found for W≥1.325µm.

The first higher order mode appears for W≥1.325µm, which is smaller than for the very similar case simulated for SOI waveguides, which did not have the SiO_2 overlayer. As with SOI_A waveguides chip space on the fabrication run was very limited, so only one width was investigated. This width was again chosen to be 1.1µm in order to be sure of single mode operation. The simulations predict a loss of 3.1dB/cm for these waveguides,

and there is only a 0.22dB/cm increase in losses with the addition of the SiO_2 top cladding layer.

4.4.3 *imec* Advanced Passives waveguides experimental results

The poly-Si on Si waveguides were prepared for characterisation by facet polishing, as described in the SOI waveguide section, and light was coupled into the chip by butt coupling. Fig. 4.14 shows a part of the experimental cut-back loss measurement results for imecAP waveguides with H=380nm, D=220nm, W=1.1µm and H_{BOX}=2µm.

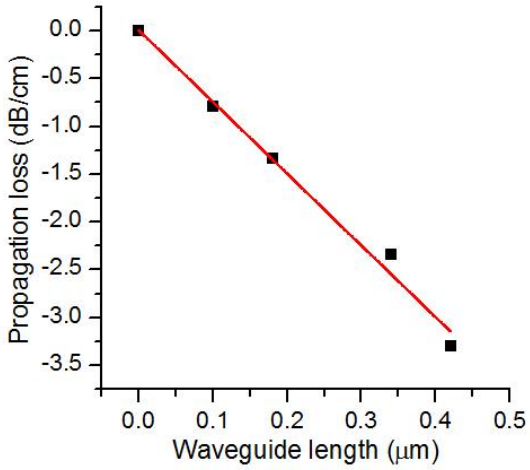

Fig. 4.14. Cut-back loss measurement for imecAP waveguides. Measured propagation loss is 7.5dB/cm, with r^2=0.987 for the fit.

The loss was measured on three identical chips as 7.5dB/cm, 7.6dB/cm and 7.6dB/cm. As with SOI waveguides, the large loss compared to simulation is attributed to scattering at both sidewalls and at scattering centres in the poly-Si layer.

Loss measurements have recently been reported at 3.76µm for poly-Si on Si waveguides that were fabricated in the same fabrication run, which have D=160nm and W=1350nm [20]. The loss was measured to be 5.3dB/cm, which suggests that the loss of the poly-Si on SOI waveguides presented in this chapter could be reduced by increasing the waveguide width. Strip waveguides based on crystalline silicon with H=400nm, W=1350nm, H_{BOX} = 2000nm and with no top oxide cladding were also fabricated in the same production run, and their loss was measured to be 3.1dB/cm. In simulations the

authors found that greater substrate leakage was expected for the crystalline silicon waveguides than the poly-Si on SOI waveguides, and as both waveguide types were fabricated using the same lithography and etch processes the sidewall roughness should be the same for both cases. The conclusion is therefore that a large proportion of the waveguide loss of poly-Si on SOI waveguides can be attributed to volume scattering in the poly-Si layer.

4.5. Germanium-on-silicon waveguides

The potential of germanium-on-silicon (Ge-on-Si) waveguides to be used throughout a large part of the mid-infrared wavelength region was discussed briefly in the literature review chapter. The first demonstration of Ge-on-Si integrated waveguides has only been recently reported [21], in which Ge-on-Si waveguides were fabricated by first deposition of a Si buffer layer on an Si wafer, followed by RP-CVD growth of a 2μm thick Ge layer, and were characterised at λ=5.8μm.

4.5.1 Ge-on-Si waveguide design and fabrication

For this project Ge-on-Si waveguides have been fabricated and characterised at λ=3.8μm, in collaboration with the University of Gent. Germanium on silicon wafers were made at imec, Belgium, by atmospheric Chemical Vapor Deposition (CVD) of Ge on an n-type Si (001) wafer with 200mm diameter, as described in [22]. Layers 1μm and 2μm thick were deposited. Because there is a 4.2% mismatch in the lattice constants of Si and Ge there is a high threading dislocation density (TDD) at the Si/Ge interface. The TDD is reduced by annealing the wafer at 850°C for 3 minutes [23], following which the TDD is reduced to approximately $10^7 cm^{-2}$ in the 2μm thick layer and $10^8 cm^{-2}$ in the 1μm layer [22].

Lithography was carried out at the University of Gent. During the etch a Ti/Cr metal mask was used. The mask pattern was defined by i-line contact lithography, followed by a lift-off process to remove excess metal. The Ge was etched by dry-etching in a CF_2/O_2 plasma. The remaining metal was removed by dipping samples in HF.

The design of the waveguides was limited, due to the deposited Ge layer thicknesses, to waveguides with H=1µm and H=2µm. Simulations that were conducted at the University of Gent, and confirmed using Fimmwave, concluded that Ge-on-Si with H=1µm would support single mode propagation in both strip and rib waveguides, whereas with H=2µm rib waveguides would have to be designed to ensure single mode propagation. Table 4.1 shows the waveguide dimensions of all of the samples that were measured. All of these waveguide geometries are expected from simulations to support only the fundamental TE and TM modes.

Table 4.1 – Ge-on-Si waveguide sample parameters

Sample	Ge_1	Ge_2	Ge_3
Waveguide height (µm)	1.0	1.0	2.0
Rib/strip	Strip	Rib	Rib
Etch depth (µm)	1.0	0.7	1.4
Waveguide widths (µm)	2.0, 2.25	2.25	1.0, 1.25, 1.50

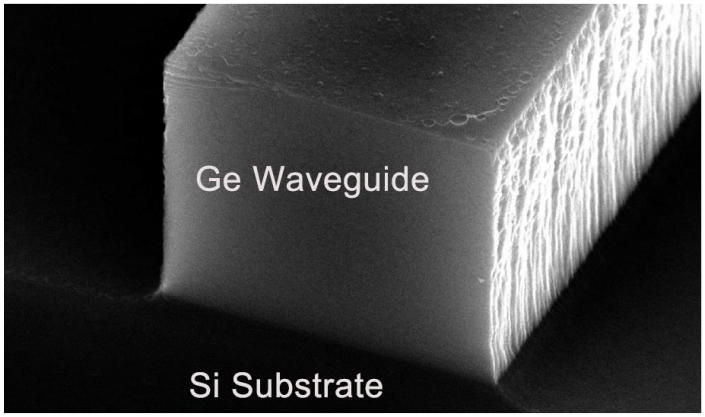

Fig. 4.15. SEM image of cleaved Ge-on-Si waveguide cross-section, reproduced from [24].

4.5.2 Ge-on-Si waveguide experimental characterisation

Light was coupled to and from the chips by butt coupling, and the waveguides tapered out to a 10µm width at the facets. To prepare the samples for measurement the samples were polished using the same process as described earlier in this chapter for SOI waveguide preparation. The propagation loss of each sample was measured using the cut-back method, and the results for each sample are shown in fig. 4.16.

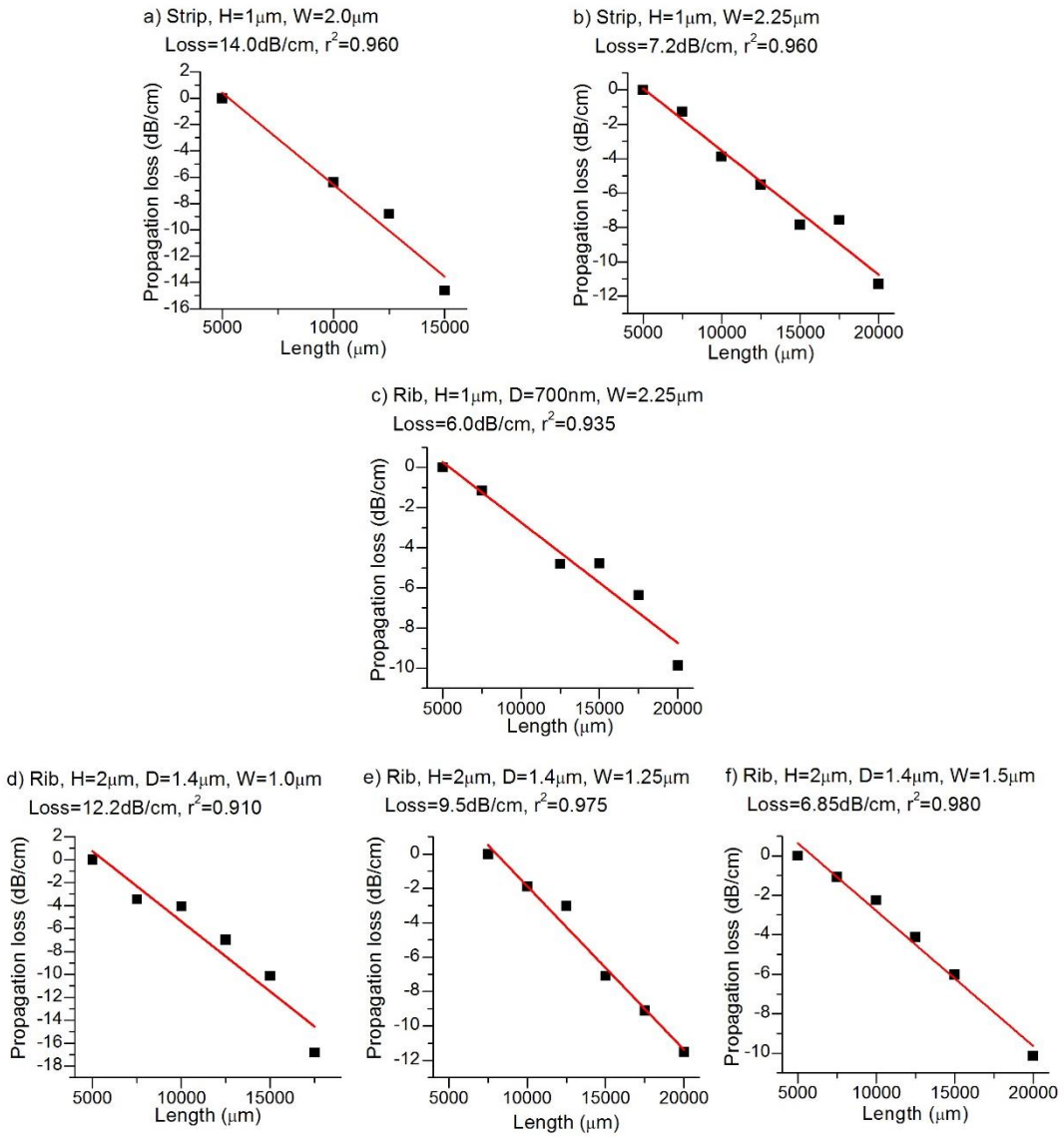

Fig. 4.16. Ge-on-Si waveguide cut-back propagation loss measurements for λ=3.77µm, with varying waveguide dimensions. a-b): H=1µm strip waveguides, c): H=1µm rib waveguides, d-f): H=2µm rib waveguides.

For each combination of waveguide height and etch depth, where different waveguide widths are available, the widest waveguides exhibit the lowest loss, as predicted. Fig. 4.17 shows the loss dependence on the width for 2µm high rib waveguides at λ=3.77µm.

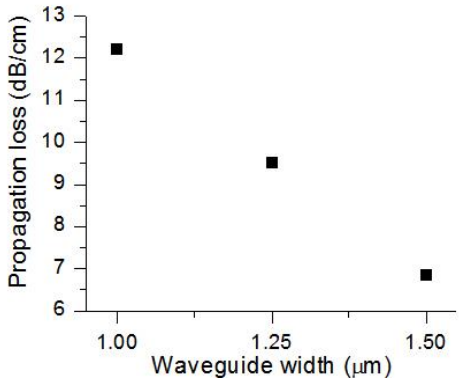

Fig. 4.17. Propagation loss of Ge-on-Si waveguides with H=2µm and D=1.4µm plotted as a function of waveguide width.

For each combination of waveguide height and etch depth the lowest propagation loss is in the range 6.0-7.2dB/cm. The 1µm high rib waveguides were measured to have a lower loss than the otherwise equivalent strip waveguides, which suggests that decreasing the etch depth reduces the sidewall roughness scattering losses. It is unclear what the dominant source of losses for these waveguides is. Fimmwave simulations predicted no loss from mode leakage to either the Si substrate or Ge slab. Si and Ge should both have negligible material absorption at 3.8µm, although it is possible that Ge material defects at the Ge/Si interface contribute to the loss. It is probable that the dominant loss mechanism is sidewall roughness scattering, which would be consistent with the large decrease in measured loss with increased waveguide width. Additionally, it can be seen from the SEM image in fig. 4.15 that the waveguide profile is not perfectly rectangular, and some roughness can be seen on the sidewalls. Improvement of the etch recipe could result in lower losses, as could using processes for roughness reduction.

The loss of waveguides fabricated using the same material fabrication methods has also been measured at 5.15-5.45µm in [24]. The loss of strip waveguides with W × H = 2.2µm × 2µm was 2.3-3.5dB/cm for TE polarization. This is considerably lower than has been

measured for waveguides at 3.8µm in this chapter. This is large difference likely due to the λ^{-4} dependence of Rayleigh scattering, which would mean that losses from both Ge material defects and sidewall roughness would be expected to decrease. Further investigation is required to determine which source of scattering is dominant.

4.6. Mid-infrared waveguides summary

In this chapter it has been shown that single mode SOI waveguides with submicron height supporting TE polarisation can have losses of 2.0dB/cm at λ=3.8µm, which is just below the wavelength at which silica absorption in the BOX layer is expected to introduce unacceptably high losses. This loss is smaller than single mode telecoms wavelength SOI waveguides fabricated in the same material platform and using identical fabrication methods. This is likely because the sidewall scattering decreases strongly with increasing wavelength, which suggests that in mid-IR waveguides based in any material platform the fabrication requirements will be significantly relaxed when compared to NIR waveguides, particularly at even longer wavelengths. The main sources of loss in these waveguides are a mixture of SiO_2 absorption from the BOX layer, leakage to the Si substrate through the BOX, and sidewall scattering. The loss could be reduced further by using a thicker BOX layer. These experimental results also suggest that the SOI material platform is likely to be very popular for MIR photonics at most wavelengths up to 4µm, due to the commercial availability of high quality SOI wafers, and due to mature silicon processing technologies.

Poly-Si on SOI rib waveguides have also been fabricated in a commercial foundry more often used for NIR silicon photonics, and their loss has been measured to be 7.6dB/cm, which is similar to the loss of SOI waveguides with the same width. The loss of these waveguides could be reduced by increasing their width while maintaining single mode propagation. Recently reported measurements [20] suggest that significant losses stem from the scattering in the poly-Si material. Nevertheless, waveguides have been demonstrated in this material platform having losses of only 3.1dB/cm [20], therefore this is a viable material platform, which allows fabrication of adjacent NIR and MIR structures. Furthermore, these results suggest that the poly-Si material could be used as

a low loss waveguide core material that might offer the benefits of cheap and flexible fabrication, and its losses could be expected to reduce at slightly longer wavelengths.

Ge-on-Si is a highly promising waveguide platform that could be used throughout a large part of the MIR wavelength range, and they Ge-on-Si waveguides have been demonstrated with losses of 6.0dB/cm at λ=3.8μm. The effect of varying the waveguide height, width and etch depth was explored experimentally. It is currently unclear what proportion of the measured loss stems from sidewall scattering due to rough etching, is due to bulk Ge material loss, or is the result of leakage to the substrate. It is expected that the loss could be reduced by optimising the etching process.

Chapter 5: Passive components for MIR modulation

In order to build a modulator based on either the thermo-optic effect or the plasma dispersion effect a structure is required to convert a refractive index change into an amplitude change. Two options for such components are the ring resonator and the Mach-Zehnder interferometer. Ring resonators are widely used, compact devices, but it has been shown in a previous work [1] that with the Quantum Cascade Laser operating at λ=3.8μm it is difficult to accurately interrogate fine spectral features, such as the narrow peaks of a high quality factor ring resonator response. Mach-Zehnder interferometers exhibit a sinusoidal spectral response, which can, depending on the free spectral range, be more accurately measured with lower effective spectral resolution.

In this chapter, the asymmetric 1×1 Mach-Zehnder interferometer (MZI) which uses 1×2 multimode interferometers (MMIs) as the splitter and coupler will be investigated.

5.1. Multimode interferometers

In the literature review the basic theory of MMIs was discussed, and a literature search of NIR MMI devices showed that the MMI can be a compact, robust device, and that low loss devices could be made through fabrication with only one etch step, by using tapered input and output ports. The device that is investigated here is therefore the 1×2 MMI with tapered input and output ports.

5.1.1. MMI design

By looking back at equation 2.4 in chapter 2, it can be seen that the position of the two-fold self-imaging location for an MMI along the axis of propagation, and therefore the length of a 1×2 MMI, is proportional to the square of the MMI width, and is inversely proportional to the operating wavelength. Therefore for a small footprint the device

should be as narrow as possible, and for a given MMI width the device can be shortened by increasing the wavelength.

During design of MMI devices equations 2.3 and 2.4 from the literature review were used to find a first approximation of the device length, and the Photon Design Fimmprop [2] software package was used for 3D simulation of the devices to refine the accuracy, as it has been shown to be an effective tool for realising efficient devices [3]. In Fimmprop the device is split up into several sections along its length, as shown in fig. 5.1, and the Fimmwave mode solver, described in the chapter 4, is used initially to find the modes supported by each section. Joins are defined between adjacent sections, in which the overlaps between the modes are calculated. A scattering matrix is then calculated which gives the coupling coefficient between each input mode and each output mode, as well as the backward scattering from reflections to other input modes. Finally, the field profile corresponding to each input is generated based on the scattering matrix. Fig. 5.1 shows an example of a simulated field profile for an MMI, on which the dimensions of this device that can be varied have been labelled.

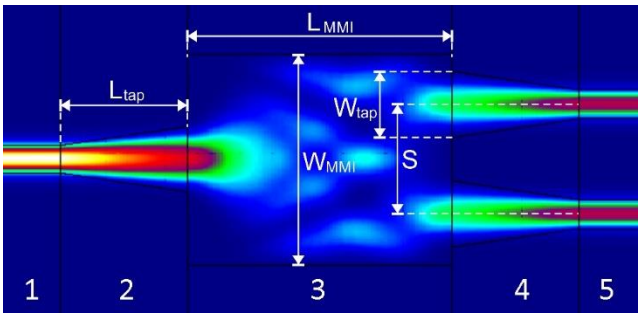

Fig. 5.1. Photon Design Fimmprop simulated intensity profile of 1×2 MMI with tapered input and output ports. Red=high intensity, blue=low intensity. For modelling the device is split into five sections, which have been marked in the figure: 1. Input waveguide, 2. Input taper, 3. Multimode waveguide, 4. Output tapers, 5. Output waveguides.

Three devices were designed, which were compatible with SOI waveguides with H=400nm and D=220nm, H=400nm and D=350nm, and with poly-Si on SOI waveguides with H=380nm and D=220nm, which will be referred to throughout the remainder of this chapter as “MMIsoi_A”, “MMIsoi_B” and “MMIsoi_poly”.

The MMIsoi_A device was designed for the same material platform as the SOI rib waveguides, fabricated at Southampton, which were shown in chapter 4. The silicon

height was 400nm, etch depth was 220nm, BOX thickness was 2000nm, and the width of approach waveguides was 1.3µm. The design approach that was followed was the same as that in [3]. As a starting point the width W_{MMI} was chosen to be 8µm, as a compromise between minimising this width, and therefore the MMI length, while making it wide enough for tapered output ports to connect to its end. Initial estimates of the self-imaging locations were chosen using the analytical equations, and inspecting the resultant field intensity profile to estimate the output port separation. Simulations were used to further optimise the design. First the length L_{MMI} was chosen using simulations by finding the peak in total transmission through the device for varying L_{MMI}. Following this the separation, S, of the output tapers was optimised, also simulating S versus the total transmission. The width of the tapers, W_{tap}, was optimised with the chosen L_{MMI} and S, and fig. 5.2 shows the results from this simulation.

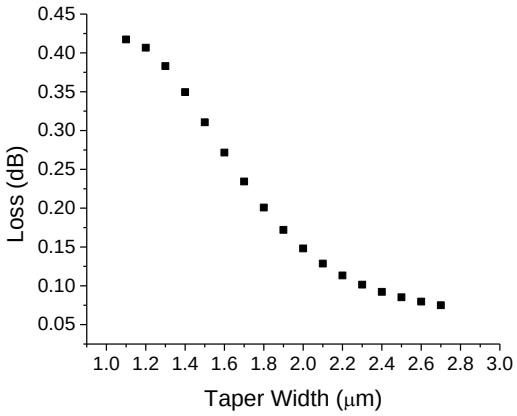

Fig. 5.2. Insertion loss of 1×2 tapered MMI simulated using Photon Design Fimmprop, with W_{MMI}=8µm, S=4.18µm, L=21µm, and varying taper width, W_{tap}.

It is clear that by increasing the taper width the simulated insertion loss of the device first decreases significantly, before plateauing as the width approaches 2.8µm, which is behaviour that is consistent with [3]. Based on the simulation results the dimensions of the device were chosen to be W_{MMI} = 8µm, L_{MMI} = 21.0µm, S = 4.18µm, W_{tap} = 2.6 µm, L_{tap} = 20µm. The access waveguide width was 1.3µm. The simulated loss including SiO_2 material absorption for such MMIs was 0.12dB/cm at λ=3.74µm, which is near to the maximum transmission wavelength of the experimental setup. As a comparison, between the basic MMI theory and these simulations, equation 2.4 from chapter 2

predicted that the first two-fold self-imaging location would be at L= 21.7µm, which differs from the simulated value by only 0.7µm. These devices will be referred to throughout the remainder of the chapter as “MMIsoi_A”.

MMIsoi_B devices were fabricated to have the same dimensions, but with access waveguide width of 1.1µm in this case. The simulation predicted a 0.19dB loss at 3.74µm for this design, which was the result of the change in etch depth.

MMIsoi_poly devices were designed using the same simulation process to be compatible with the poly-Si on SOI waveguides that were presented in the waveguides chapter, based on rib waveguides with 380nm height, 220nm etch depth into the material stack, access waveguide width of 1100nm, BOX thickness of 2µm, and a 1µm thick SiO_2 top cladding. The designed dimensions were W_{MMI} = 8µm, L_{MMI} = 21.0µm, S = 4.18µm, W_{tap} = 2.6µm, L_{tap} = 20µm, and the predicted loss was 0.21db at 3.74µm.

5.1.2. MMI fabrication and characterisation

MMIs were fabricated at the University of Southampton using the same SOI material platform and fabrication methods as were used for the demonstration of waveguides. The chips were designed for coupling via grating couplers. The insertion loss was measured by chaining different numbers of pairs of MMIs together, and plotting a linear line of best fit between the measured optical transmissions, as is shown in fig. 5.3. The shortest chain had a single pair of MMIs, and the longest had 18 MMIs. In fig. 5.4 the optical transmissions have been normalized to the structure with the greatest transmission, which was the waveguide with two MMIs.

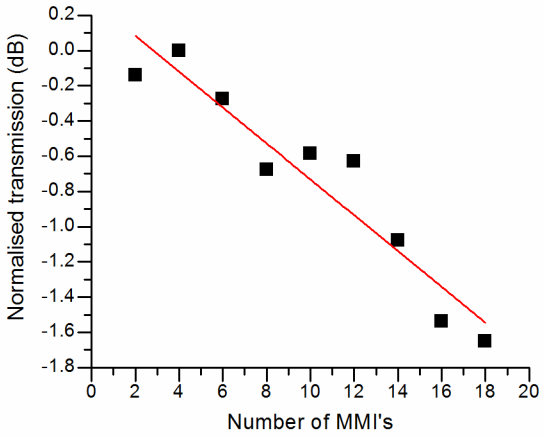

Fig. 5.3 Normalised transmission measurement of SOI MMI's with H=400nm and D=220nm, at λ=3.8μm. The graph shows the normalized loss through different numbers of successive pairs of MMIs. The gradient of the line for best fit gives the insertion loss per MMI.

The insertion loss for MMIsoi_A devices was measured to be 0.10±0.01dB per MMI at 3.8μm. This figure is similar to the simulated loss figure of 0.12dB, and compares favourably to the best published results for NIR MMIs, even those with multiple etch steps [4].

MMIsoi_B devices were fabricated in the same run as the SOI waveguides that were fabricated at Glasgow. Fig. 5.4 is an example of an SEM image of one of the fabricated devices

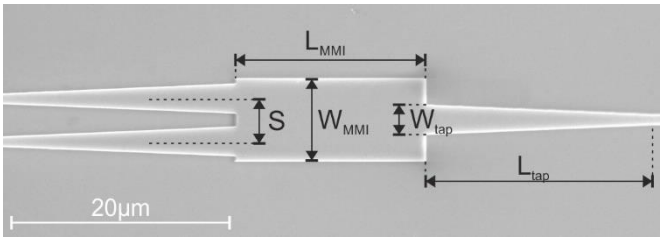

Fig. 5.4. Labelled SEM image of a 1× 2 MMI fabricated by e-beam lithography at the University of Glasgow, based on SOI wafers with H=400nm and D=350nm.

The chips were designed for butt coupling, and the insertion loss measurement method was the same as that for MMIsoi_A devices. Normalized transmission loss measurements for MMIsoi_B devices are shown in fig. 5.5. The measured transmission loss at λ=3.74μm was measured to be 0.25±0.02dB per MMI.

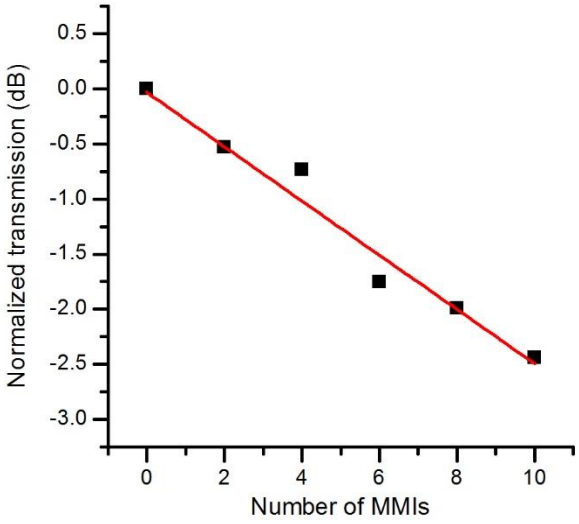

Fig. 5.5. Insertion loss measurements of MMIsoi_B waveguides. Measured insertion loss is 0.25±0.02dB per MMI. The normalized transmission though each MMI chain is plotted against the number of MMIs.

MMIsoi_poly devices were fabricated in the same run as the poly-Si on SOI waveguides presented in chapter 4. As with MMIsoi_B devices, they were designed for butt coupling, and the approach waveguides were 1.1µm wide. The insertion loss per MMI was measured to be 0.37±0.08dB, which is approximately 0.16dB larger than expected from simulations. The source of this difference is likely due to the higher loss of the poly-Si material that these devices are based on.

For MMIs based in all three material platforms the insertion loss was <0.4dB/MMI, which demonstrates that this design approach is valid at mid-infrared wavelengths, and furthermore, Mach-Zehnder interferometers for the 3.8µm wavelength range can be designed with low insertion loss splitters and couplers.

5.2. Mach-Zehnder interferometers

The asymmetric 1×1 Mach-Zehnder interferometer (MZI) with one input and one output is investigated here for later use as part of a thermo-optic modulator. The device is asymmetric, so that it can be more easily characterised. The device is measured in two configurations: the first is a conventional device where the arms of the MZI are straight waveguides, like the one shown in the schematic diagram fig. 5.6, and the second has

spiral shaped arms. The spiral-armed design is explored here because it has been shown to be more power efficient for thermo-optic modulators in the NIR [5], but it has also been used as a way to wrap a large length of waveguide into a small area for molecular sensing applications [6].

5.2.1. MZI design

In the literature review these expressions were given for the efficiency and phase change of an ideal asymmetric 1×1 MZI:

$$\eta = \frac{P_o}{P_{in}} = \cos^2\left(\Delta\phi/2\right) \qquad \text{Eq. 5.1}$$

$$\Delta\phi = \frac{2\pi n_{eff}\Delta L}{\lambda} \qquad \text{Eq. 5.2}$$

Where η is the Mach-Zehnder efficiency, P_o is the output power, P_{in} is the input power, $\Delta\phi$ is the change in phase, n_{eff} is the effective refractive index of the waveguide, ΔL is the optical path length difference between the two arms, and λ is the wavelength. In this case for the design of MZIs the waveguides have already been determined, and MMIs that have been investigated are to be used for the splitters and couplers, leaving the relationship between free-spectral range (the wavelength separation of successive peaks) and the path length difference to be determined.

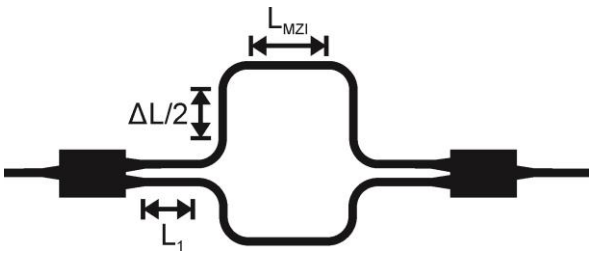

Fig. 5.6. Labelled schematic diagram of asymmetric 1×1 Mach-Zehnder interferometer with MMI splitter and coupler.

An expression for free-spectral range (FSR) can be derived, with equations 5.1 and 5.2 as the starting point, in the following way.

For one transmission peak in the asymmetric 1×1 MZI response:

$$\phi = \frac{2\pi n_g \Delta \mathrm{L}}{\lambda} \quad \text{Eq. 5.3}$$

where n_g is the group index. The adjacent transmission peak in the spectral response is separated by a phase change of 2π, as peaks in the function $y = cos^2(x/2)$ occur when x is a multiple of 2π:

$$\phi - 2\pi = \frac{2\pi n_{eff} \Delta \mathrm{L}}{\lambda + FSR} \quad \text{Eq. 5.4}$$

Eq. 5.3 is then substituted for ϕ in eq. 5.4:

$$\frac{2\pi n_g \Delta \mathrm{L}}{\lambda} - 2\pi = \frac{2\pi n_g \Delta \mathrm{L}}{\lambda + FSR} \quad \text{Eq. 5.5}$$

$$\frac{n_{eff} \Delta \mathrm{L}}{\lambda} - 1 = \frac{n_g \Delta \mathrm{L}}{\lambda + FSR} \quad \text{Eq. 5.6}$$

$$n_g \Delta \mathrm{L}(\lambda + FSR) - \lambda(\lambda + FSR) = n_g \Delta \mathrm{L} \quad \text{Eq. 5.7}$$

$$FSR n_g \Delta \mathrm{L} - \lambda^2 - FSR\lambda = 0 \quad \text{Eq. 5.8}$$

$$\therefore FSR = \frac{\lambda^2}{n_g \Delta \mathrm{L} - \lambda} \quad \text{Eq. 5.9}$$

Hence for a MZI based on SOI waveguides with W=1.1μm, H=400nm, D=220nm and H_{BOX}=2000nm, the group index is simulated using Fimmwave to be 4.03 at λ=3.77μm. Using these values with equation 5.9, the curve in fig. 5.7 is obtained. A larger FSR requires a larger path length difference, and from eq. 5.9, in order to achieve the same FSR the path length difference is approximately proportional to λ^2, since for most practical devices $n_g \Delta L \gg \lambda$.

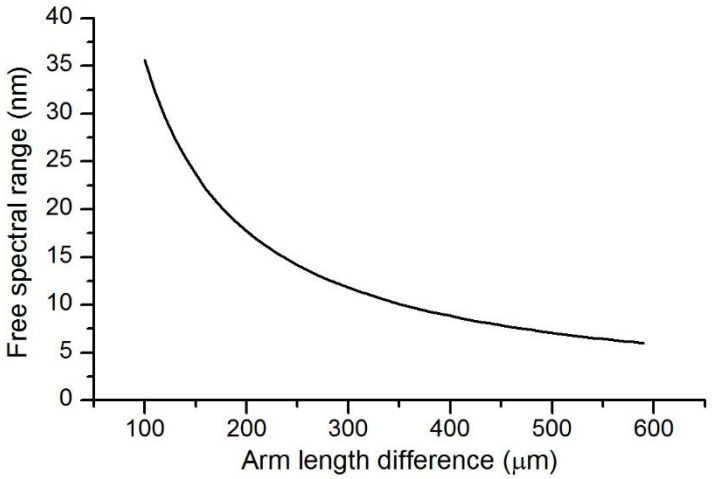

Fig. 5.7. Free spectral range as a function of MZI arm length difference for an SOI waveguide with W=1300nm, H=400nm, D=220nm, and H_{BOX} =2000nm, calculated using eq. 5.9 and a simulated group index value for λ=3.77μm.

Fig. 5.8 shows a labelled diagram of the type of spiral that is placed in each arm of the spiral-arm MZI. The figure shows the spiral dimensions that can be varied, each of which have an effect on its total length: the waveguide width (W), the width of the gap separating waveguides (W_{gap}), and the radius of the inner bends of the spiral (R_0). The number of "loops" of the spiral (N) is defined by the number of full circles that the waveguide passes around, beginning from the centre of spiral, and ending when the waveguide leaves the spiral. The spiral shown in fig. 5.8 is for N=1.

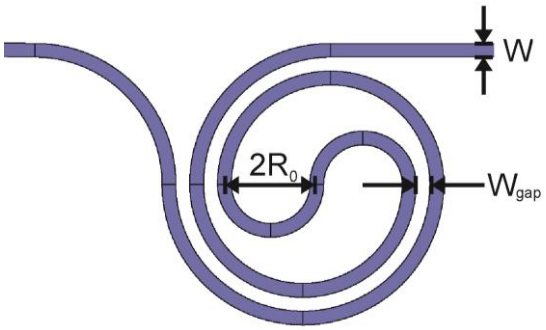

Fig. 5.8. Labelled diagram of a spiral waveguide, which is integrated into each arm of the spiral-arm MZI.

R_0 is the smallest bend radius used in the spiral, and should be large enough not to introduce too much bending loss, while being small enough such that the waveguide can

still be folded into a compact area. Fig. 5.9 shows the simulated mode profiles of bent waveguides with bending radii of a) 5µm, b) 10µm and c) 15µm.

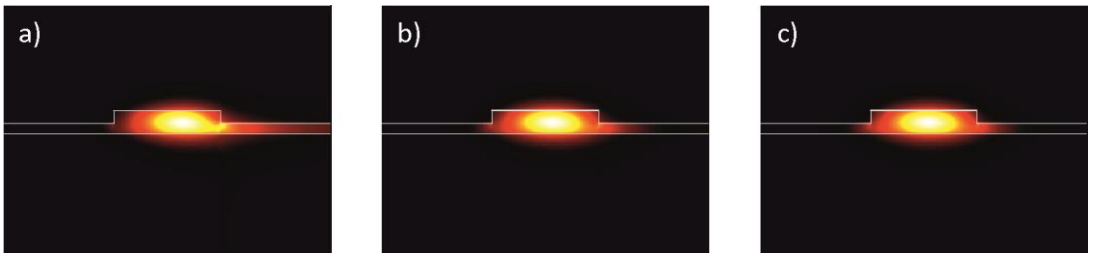

Fig. 5.9. Fimmwave simulated mode profiles of bent SOI waveguides with W=1300nm, H=400nm, D=220nm and H_{BOX}=2µm, with bend radii of a) 5µm, b) 10µm and c) 15µm.

The simulation does not include loss from substrate leakage or from scattering loss, but does include leakage into the silicon slab. In fig. 5.9 it is clear that with a tight bend radius there is leakage into the slab, and also that mode interaction with sidewalls increases, so roughness scattering losses can be expected to increase significantly. Fig. 5.10 shows the simulated propagation loss of bent waveguides of different bending radii, for SOI waveguides with H=400nm, D=220m, W=1300nm and H_{BOX}=2µm. Waveguides with bending radii smaller than approximately 22.5µm exhibit greater loss than straight waveguides.

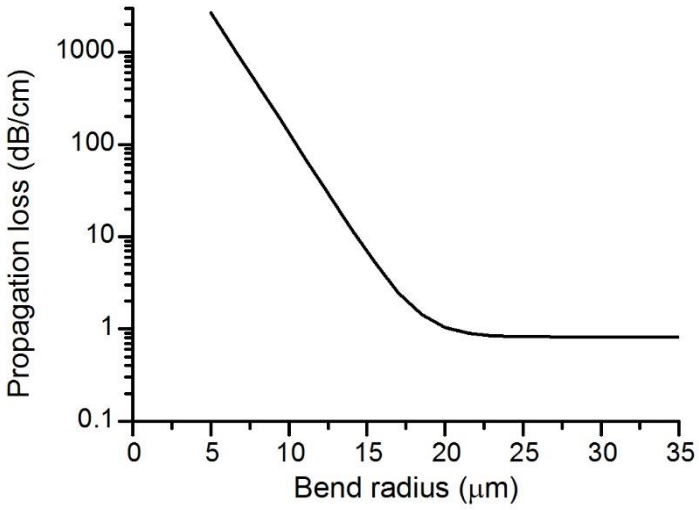

Fig. 5.10. Simulated propagation loss (dB/cm) of a bending SOI waveguide, as a function of bend radius, at λ=3.8µm. The simulated waveguide had dimensions H=400nm, D=220m, W=1300nm and H_{BOX}=2µm.

The gap between waveguides in the spiral, W_{gap}, should be large enough so that the modes from waveguides in adjacent loops of the spiral do not interact with each other. Fig. 5.11 shows simulated mode intensity across the waveguide concentration at the widest point of the mode profile, for the same SOI waveguides. From the figure it can be concluded that the mode intensity is negligible 2µm away from the waveguide centre in either direction. In the designed devices the centre to centre separation of the waveguides will therefore be 4.3µm, and the edge to edge separation will be 3µm.

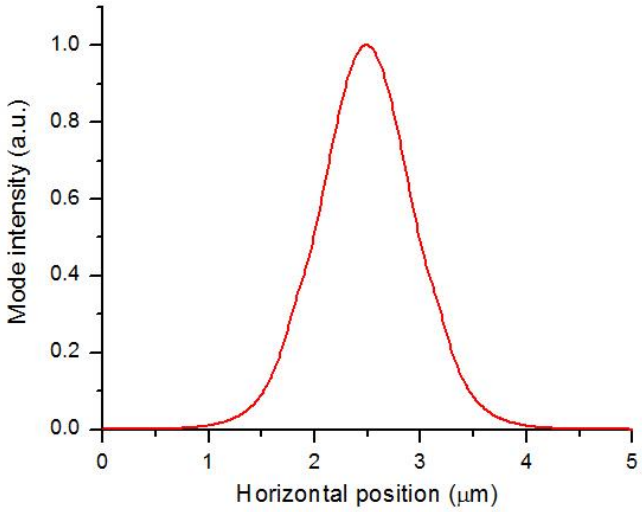

Fig. 5.11. Cross-section of the optical mode electric field intensity parallel to the wafer. Mode profile simulated using Fimmwave. The centre of the waveguide is at the horizontal position of 2.5µm.

Asymmetric MZIs have been designed in which the spiral in one arm has "N" loops, and the spiral in the other arm has "N+1" loops, so that there is a length difference between the two arms. In total 24 structures were designed, in which the number of loops in the shorter arm was varied between 1 and 6, and the inner bend radius was varied between 20µm and 42.5µm.

5.2.2. Straight-arm MZI fabrication and characterisation

MZIs were fabricated at the University of Glasgow that were based on SOI waveguides with W=1100nm, H=400nm, D=350nm and H_{BOX}=2000nm, and devices based on this platform will be referred to as MZIsoi_A. Devices were also fabricated at the University of Southampton, which were later used for thermo-optic modulation. These devices

were based on waveguides with W=1300nm, H=400nm, D=220nm and H_{BOX}=2000nm, and will be referred to as MZIsoi_B.

MZIsoi_A devices were designed with L_1=100μm, L_{MZI}=100μm, bend radius R=75μm and ΔL=250-450μm. Fig. 5.12 shows the spectrum of the MZI with ΔL=300μm. The measured insertion loss over this wavelength range is 1.6-2.4dB, the extinction ratio is up to 25dB, and the FSR is 11.2nm.

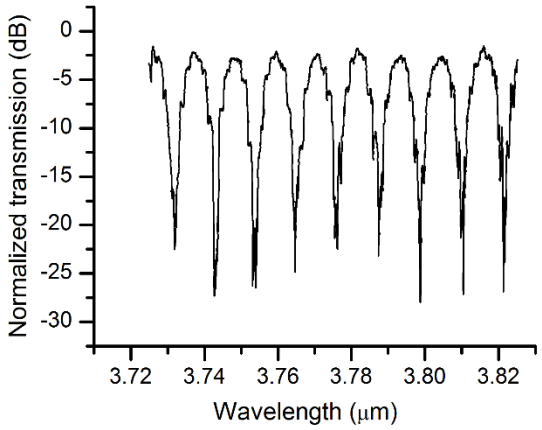

Fig. 5.12. Normalized transmission through MZIsoi_A type device with 350 μm arm length difference.

In fig. 5.13 the measured free-spectral range values at λ=3750nm for each ΔL have been plotted. A curve of the form of eq. 5.9 has been fitted to the data in order to extract from experimental measurements a value for the group index.

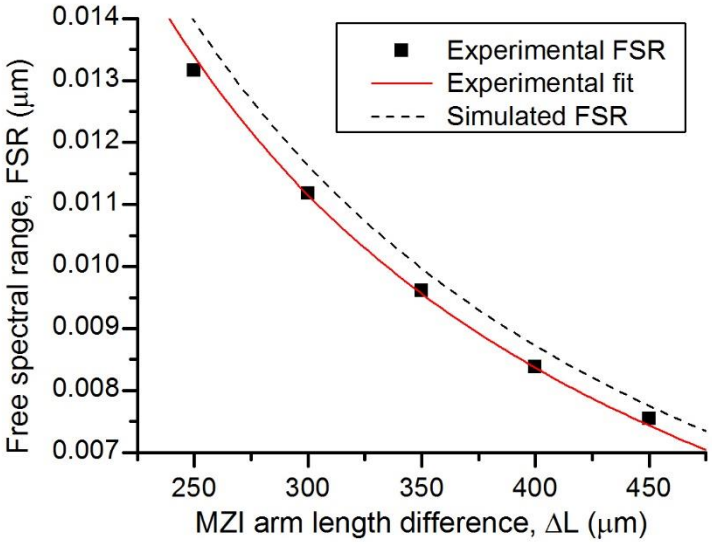

Fig. 5.13. Experimentally measured FSR values (black squares) plotted against MZI arm length difference for MZIsoi_A type devices. The red line shows a fit of the group index to the data with eq. 5.9 (n_g=4.20), while the black line shows the predicted FSR from the simulated group index (n_g=4.03).

The fitted group index value is 4.20, which is slightly larger than the simulated value of 4.03. Curves calculated using both values are plotted alongside the experimental values in fig. 5.13. The difference in simulated and fitted FSR values is on the order of ~0.5nm. Despite this slight discrepancy, it is clear that the modelling techniques for MZI devices that have been used are valid at the MIR wavelengths that are being investigated.

MZIsoi_B devices were designed with the dimensions L_1=100μm, L_{MZI}=2250-4500μm, R=60μm and ΔL=300μm. For these devices the average insertion loss over the 3725-3800nm range was 1.34-2.16dB, and the average extinction ratio was in the range 19.3-22.6dB, with the highest measured extinction ratio being 28.2dB.

5.2.3. Spiral-arm MZI fabrication and characterisation

Spiral-arm MZIs were fabricated in the same way as MZIsoi_B devices, and were based on the same waveguides. Fig. 5.14 shows an optical microscope image of one of the fabricated structures.

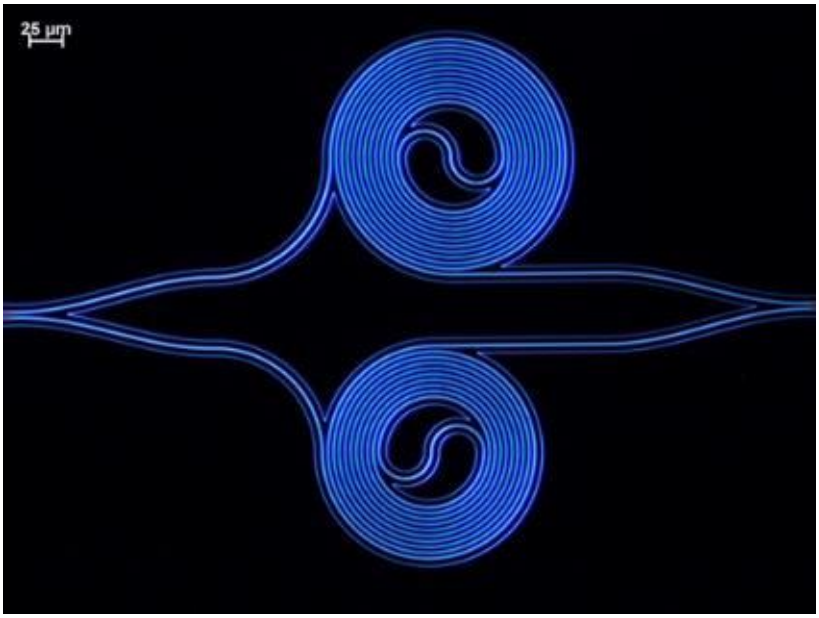

Fig. 5.14. Optical microscope image of an asymmetric spiral-arm MZI, based on SOI waveguides.

Fig. 5.15 shows the normalised wavelength response of a spiral-arm MZI with 2 spiral loops, R_0=27.5µm, W_{gap}=4µm and W=1.3µm. The average insertion loss of this device is 3.7dB, its average extinction ratio is 11.7dB, and the maximum extinction ratio is 21.0dB.

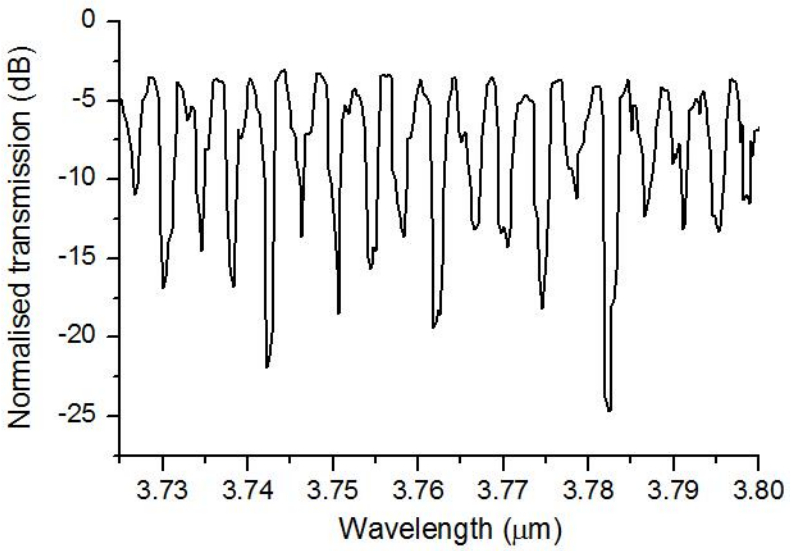

Fig. 5.15. Normalised transmission of asymmetric spiral-arm MZI with two spiral loops in the shorter arm and three loops in the longer arm, and W_{gap}=4µm, R_0=27.5µm, W=1.3µm.

This was the best overall performance of the 24 spiral-arm MZI structures that were fabricated and tested. The large variation in the extinction ratio over the measured spectrum is thought to be due to the mode-hopping behaviour of the laser. Since the

FSR is much smaller for these devices than for the straight-arm MZIs, the laser wavelength instability results in a smaller likelihood of measuring the lowest point of a particular valley. The 24 devices had R_0 of 20μm, 27.5μm, 35μm or 42.5μm, and between 1 and 6 spiral loops. For all of these devices, the insertion loss was 3.1-9.2dB, the average extinction ratio was 4.8-11.8dB, and the maximum extinction ratio was 7.9-21.0dB. The issue of high fabrication defect density that arose for waveguides fabricated at the University of Southampton in chapter 4 is a problem for the analysis of the results of these structures. As a result there are no clear correlations in the data between extinction ratio and spiral inner bend radius, overall spiral length or number of spiral loops. For the insertion loss, a weak correlation can be found between insertion loss and total spiral length. Fig. 5.15 shows the average length of spirals of devices with the same number of loops plotted against the average insertion loss for those structures. The average loss per unit length of these spiral waveguides is then calculated to be 4.8±2.3dB/cm, which is most likely slightly larger than the insertion loss of straight waveguides of the same width, which is 3.5dB/cm. This could be an indication that the bending in the spiral waveguides introduces some excess loss.

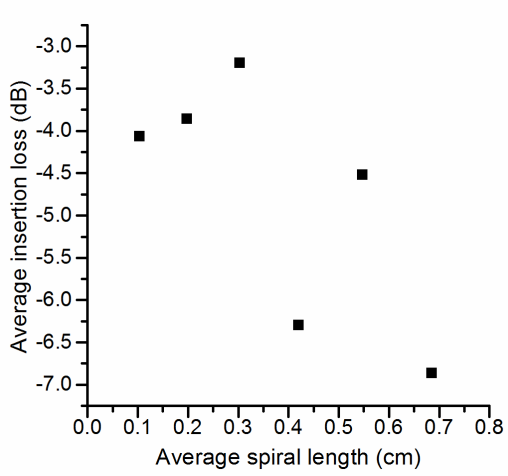

Fig. 5.16. Average length of spirals with the same number of loops plotted against their average insertion loss.

The insertion losses of all of the measured spiral-arm MZIs are larger than the insertion losses of straight-arm MZIs based on the same waveguides and MMIs. The sources of this excess loss could be the S-bends that are used in the spiral MZIs, or more likely from loss in the inner loops of the spirals, where the bend radii are smallest. The bend loss of

R=30µm bends for 1300nm wide waveguides has been measured experimentally, by measuring the transmission through waveguides with different numbers of connected 90° bends. The result is plotted in fig. 5.17.

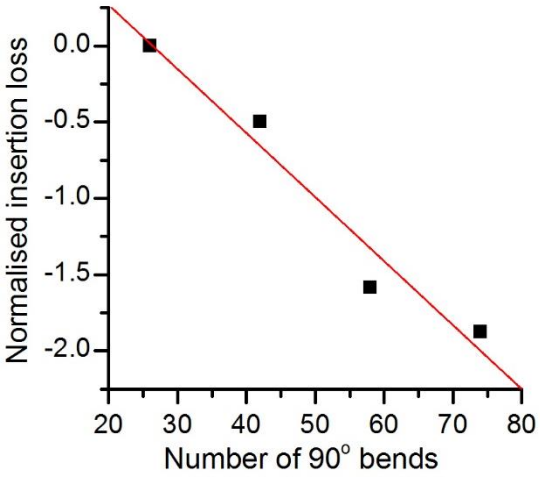

Fig. 5.17. Normalised insertion loss for different numbers of linked 90° bends of R=30µm, for SOI waveguides with H=400nm, D=220nm, H_{BOX}=2µm, and W=1300nm.

The bend loss was measured to be 0.042±0.006dB/90° bend, which is equivalent to a loss of 8.9dB/cm. The loss is larger than the loss of straight waveguides (3.5dB/cm), and is significantly larger than the simulated loss of bend waveguides with this radius (0.8dB/cm, excluding substrate leakage). It is therefore likely that for the inner bends used in the spiral, the smallest of which was R_0=20µm, the bend loss was also larger than the simulated values (1.0dB/cm, excluding substrate leakage), and might explain a large part of the greater insertion loss in the spiral-arm waveguides.

5.3. Summary

In this chapter the passive components required as the building blocks of a modulator were experimentally demonstrated. Mach-Zehnder interferometers were investigated as components that could convert a phase change into an intensity change, and multimode interferometers were investigated for splitting light into the two arms of the MZI, and for coupling light back into a single waveguide.

Compact SOI based 1×2 multimode interferometers have been demonstrated experimentally at λ=3.74µm with very low insertion losses of only 0.1±0.01dB, which rivals the best reported losses for NIR MMIs. Low loss MMIs based on the poly-Si on SOI

waveguide platform were also demonstrated experimentally, which exhibited a small loss penalty compared to crystalline Si waveguides. Aside from their use in MZIs, splitters/couplers are crucial parts of many photonic systems, and they could be applied for other functions in sensing systems. This result also demonstrates that the simulation methods used for MMI design work as well in the MIR as they do in the NIR, and that the same method can be used for the design of MMIs for other wavelengths and other material platforms.

Conventional MZIs were demonstrated which had insertion losses of 1.3-2.2dB, and extinction ratios as large as 28.2dB. MZIs can be used not only for modulation but also in sensing: for example SOI MZIs have been used for creating on chip Fourier transform infrared spectrometers (FTIR) [7], therefore the demonstration of these devices is an important part of building a library of photonic components.

Spirals are an efficient way of folding a long waveguide into a compact area, therefore MZIs with spiral waveguides in each arm were also demonstrated in order to both shrink the footprint of conventional MZIs for increased photonic circuit density, and as a method of achieving higher efficiency thermal modulators, which is discussed in chapter 6. They were measured as having insertion losses as low as 3.1dB, and average extinction ratios as large as 11.8dB. The greater insertion loss and reduced extinction ratio compared to the straight-arm MZI are likely the result of bending losses in the spiral waveguide. The move towards longer wavelengths limits the spiral density in two ways; the minimum bending radius is larger at longer wavelengths, and because the spacing between adjacent loops of the spiral must be large enough such that the evanescent fields of the optical modes in the two waveguides do not interfere with each other, the spacing between adjacent spiral loops must be larger.

Chapter 6: Silicon thermo-optic modulators for the MIR

In this chapter thermo-optic modulators based on SOI waveguides operating at the wavelength of λ=3.8μm are demonstrated. The literature review of NIR modulators showed that thermo-optic modulators can be expected to be orders of magnitude slower than those that are based on the plasma dispersion effect. Slow modulators based on the thermo-optic effect might nevertheless find applications for improving the signal to noise ratio in MIR sensing systems. For experimental characterisation setups in the MIR a combination of a chopper and lock-in amplifier operating at 10^2-10^4Hz are used to increase the operating frequency of the system to where the frequency dependent noise might be smaller. A thermo-optic modulator could fulfil the function of a chopper in the on-chip equivalent of such a system. The modulators investigated in this chapter are based on waveguides that were presented in chapter 4, and on the passive optical components that were shown in chapter 5. Their design, fabrication and characterisation are discussed here.

6.1. MIR thermo-optic modulator design

The principle underlying silicon thermo-optic modulators operating at NIR wavelengths was introduced in chapter 2. Typically a metal wire heater is placed above one arm of a Mach-Zehnder interferometer, or above a ring resonator, and the temperature change creates a change in the refractive index of silicon and in the effective index of the optical mode. The metal heater is separated from the optical mode by a layer of SiO_2, as metals typically exhibit extremely high optical absorption. The MZI or ring resonator converts this phase change into an intensity change in the device output. In this work, the MZIs with both straight and spiral arms that were demonstrated in chapter 5 are used as the passive components that form the basis of the thermal modulator. The SiO_2 thickness and wire heater patterns for straight arm MZI and spiral arm MZI configurations need to be designed.

Fig. 6.1 shows two possible placements for the metal heaters for straight arm MZIs, on the surface of the silica isolating layer, where in both cases the heaters run parallel to the waveguide for the length of the MZI arm. The metal heater can be placed directly above the waveguide (fig. 6.1a) or slightly laterally separated from it (fig 6.1b).

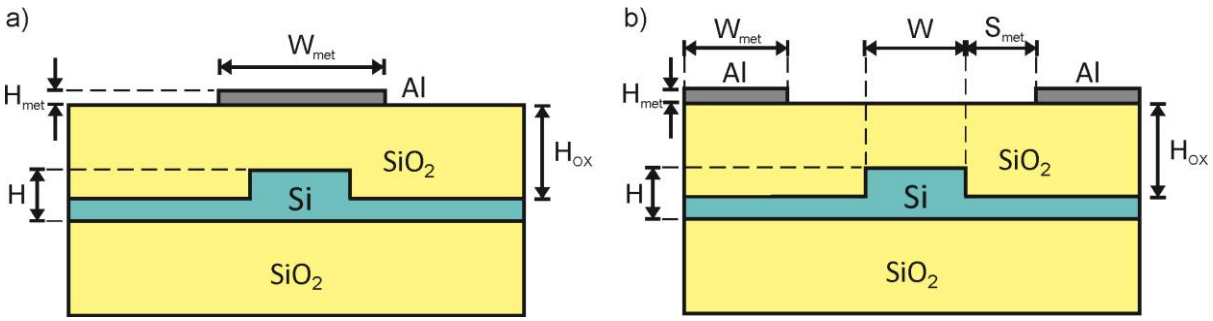

Fig. 6.1. Labelled schematic cross-section diagram of thermo-optic phase shifters, with metal heaters a) directly above waveguide, and b) separated laterally from waveguide.

The lateral placement offers increased isolation of the metal from the optical mode, but at the cost of distance of the heaters from the waveguide, which means that, because the heat will dissipate away from the heater in all directions, to heat the waveguide to the same temperature greater thermal power will be required. It is important to know for both cases what thickness of silica top cladding would result in negligible excess optical loss.

The dependence of the optical loss due to metal material absorption with varying silica layer thickness has been simulated using Fimmwave. In the simulations the following dimensions have been used, which match the dimensions of the SOI waveguides that were used for the MZI measurements in chapter 5: H=400nm, D=220nm, W=1300nm, and H_{BOX}=2000nm. For the simulations and fabrication the metal was chosen to be aluminium, for which the absorption coefficient at λ=3.8μm according to [1] is $1.3\times10^{6}cm^{-1}$. Aluminium was chosen because it is commonly used as an electrode material, and the deposition and etching recipes had already been well characterised. The simulation results are shown in fig. 6.2. Note that the simulations included SiO_2 loss, but did not include contributions to loss from substrate leakage or roughness scattering, which should not affect the conclusion of this investigation.

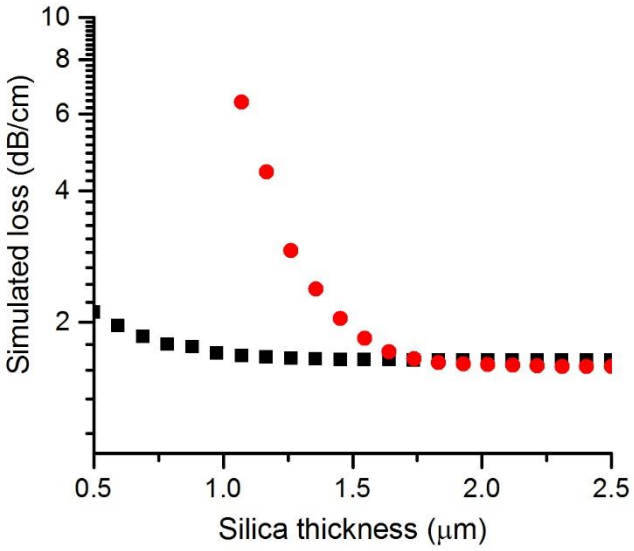

Fig. 6.2. Fimmwave simulation results showing optical absorption of devices with metal strips placed directly above the waveguides (red dots) and placed adjacent to the waveguides (black squares), with a 1μm edge to edge separation between the waveguide and metal strip. The metal strip is 100nm thick, and extends to the edge of the simulation region for both configurations.

For both metal configurations the simulated loss shrinks as the silica thickness is increased, until it reaches a steady state where all loss is due to SiO_2 absorption. The simulations predict that a significantly thinner silica layer can be used when the metal heater is placed adjacent to the waveguides instead of above it, without incurring significant loss from metal absorption. When the metal is placed directly above a waveguide, the metal absorption becomes negligible for approximately H_{OX}>2μm.

Fig. 6.3 shows an example of a mask design of a spiral arm MZI, with a heater placed above one of the arms, following the heater folding scheme that has been used for NIR thermo-optic modulators in [2]. The heater is folded so that it passes back and forth multiple times directly above the spiral waveguide, and therefore the silica top cladding for this design should be at least 2μm thick.

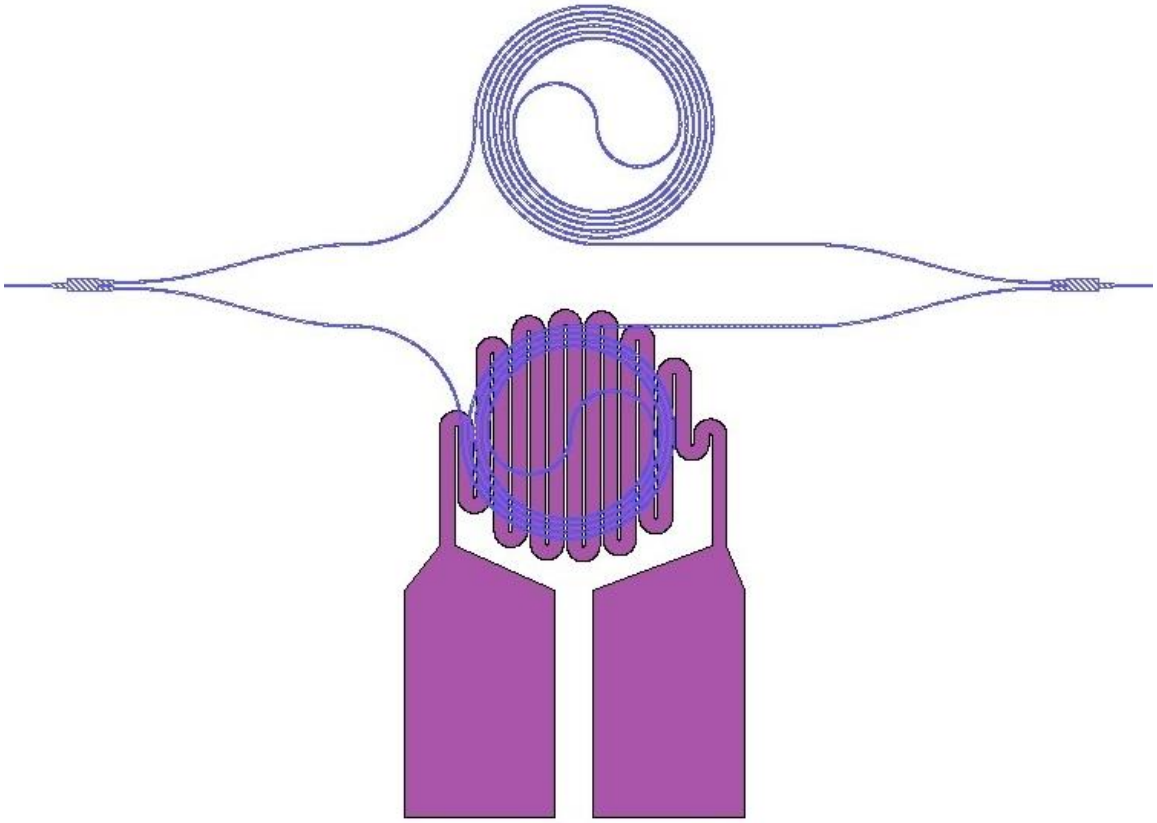

Fig. 6.3. Example mask design of a spiral arm MZI, with a metal strip folded above the waveguide spiral acting as a heater.

As designs of both straight and spiral MZIs were fabricated on the same chip, H_{OX}=2µm was used for all modulator designs. For straight arm modulators the metal was separated laterally from the waveguide by S_{met}=1µm, as a conservative design choice in order to ensure that functioning devices could be demonstrated even in the possible case of error in the simulations or if the metal absorption coefficient differed significantly in practice from the literature value used in simulations. Aluminium was used as the heater material, and the heater width was chosen to be 10µm and 15µm, and the heater thickness was varied between 80nm and 140nm. The probe pads were both 100µm wide and separated by a 25µm gap, so as to accommodate the electrical probe dimensions.

6.2. Fabrication

Fabrication of the waveguide layer of the devices was carried out as described in section 3.3.2, and at this stage the wafer was diced up into chips. The mask design included alignment marks that could be used for chip level optical alignment in addition to those that are essential for e-beam lithography, so that the metal layer could be aligned to the waveguide layer. Scott Reynolds carried out SiO_2 deposition, metal sputtering was performed by myself, all metal lithography steps were performed by Dr. Colin Mitchell, Dr. Stevan Stanković performed metal etching, and final sample cleaning was carried out by me.

i. A 2µm thick layer of SiO_2 was deposited by PECVD (Oxford Instruments system 100LS) using $SiH_4/N_2O/N_2$ gases with flow rates of 4.2sccm/350sccm/80sccm at a temperature of 350°C, a pressure of 1000mT and RF power of 20W. This deposition took 30 minutes.

ii. Following this the aluminium layer was deposited using the Leybold Helios system for metal sputtering. The sputterer deposits aluminium at a rate of 0.245nm/s, which was determined from calibration.

iii. A layer of AZ5214 positive photoresist was then spun onto the chips, and the chip was then baked on a hot-plate at 110°C for 50s. Optical lithography was performed by standard hard contact lithography using a MJB4 mask aligner.

iv. After exposure the samples were developed using MF319 developer for approximately 30 seconds, and rinsed in DI water.

v. The metal was etched to create the heater pattern using an Oxford Instruments SYS 380 ICP, which is used as a dedicated machine for metal processing. The etch was based on HBr/Cl_2 chemistry, with respective flow rates of 40.0sccm and 10.2sccm. The RF power was 40W, the temperature was 15°C, the pressure was 5mTorr, the DC bias was 193V, and the etching time was 90s.

vi. Finally, the remaining resist was removed by submerging the samples in first acetone, then IPA, and finally DI water, before blowing water off the chip surfaces with an N_2 gun, and placing the samples on a hotplate at 110°C for 2 minutes to evaporate water traces. An exposure to an O_2 plasma for 5

minutes in the PVA Tepla 300 asher was used to remove any remaining photoresist.

6.3. Electrical characterisation equipment

For optical testing the same equipment and experimental methods that were described in chapter 3 were used for characterisation of these chips, which were fabricated with grating couplers to assist with coupling light on and off the chip. Additional equipment was required in order to characterise the electrical and electro-optical performance of the device through the application of DC and AC electrical signals to the heaters. For both DC and AC measurements an electrical probe (Picoprobe 40A-GSG-100-DS) was used to contact the pads. The probe tips were spaced 200µm apart. The probe was held by an arm with a 3-axis stage at its base, which enabled accurate positioning of the probe. The probe was in all cases lowered to make a firm contact with the metal pads on the chip before optical alignment, as when the probe contacts the chip it usually results in a movement of the chip that would disturb any previous optical alignment.

For DC characterisation an Agilent E3640A DC power supply was used, which could supply up to a 20V signal. The power supply was connected by GPIB cable to the PC that also controls the QCL laser controller and lock-in amplifier, and a custom LabView program was written for simultaneous control of all instruments, in order that scans of DC voltage plotted against measured optical power could be recorded automatically.

For AC characterisation a TTi TGA1241 waveform generator was used to generate a square wave. For these measurements the mechanical chopper was removed from the optical path, and instead the modulated optical signal effectively served as a chopper. The signal generator also supplied a trigger signal at the modulation frequency to the lock-in amplifier, which then filtered out signals from the MIR detector that were at other frequencies. When aligning to the chip, initial optical alignment was carried out with the chopper still in the system, as for the testing of passive components, and after initial alignment the chopper was switched off and replaced by the AC signal. As with the DC power supply, the AC waveform generator was connected to the PC by a GPIB cable, and a LabView program was written to control the instrument, thus enabling

frequency scans of the optical output to be recorded. The operation frequencies of the modulator for this application were well below the high frequency cut-offs of both the InSb detector and the lock-in amplifier.

6.4. Electrical characterisation results

Unfortunately, it was impossible to measure the insertion loss of the fabricated devices after the SiO_2 layer had been deposited. Because the silica layer was deposited onto individual chips after dicing, the SiO_2 thickness was smaller closer to the edge of the chips than in the middle. This was visible by eye from colour variation across the chip surface, which is the result of a varying path length difference (due to varying SiO_2 thickness) for interference between light reflected from the upper and lower boundaries of the thin SiO_2 film that produces variation in the wavelengths at which constructive interference occurs. In the design normalisation structures were placed close to the edge of the chip, while MZIs were mostly towards the chip centre. As a consequence significantly smaller coupling efficiencies were observed for the normalisation structures than for MZI structures, therefore the only available valid insertion loss measurements were for passive MZIs, before SiO_2 deposition.

Of the electrical measurements, the DC response of the devices was characterised first. After lowering the probe into contact with the contact pads of a heater and optical alignment to the device, a voltage was applied across the two probe tips to verify that there was current flow. An automatic scan of applied DC power versus optical transmission was then performed. The LabView control program logged the voltage and current applied to the device, from which the applied electrical power could be calculated. Fig. 6.4 shows the output from such a scan, which was performed on an asymmetric spiral-arm modulator with a heated spiral arm length, L_H, of 1.77mm and an arm length difference, ΔL, of 96.1µm.

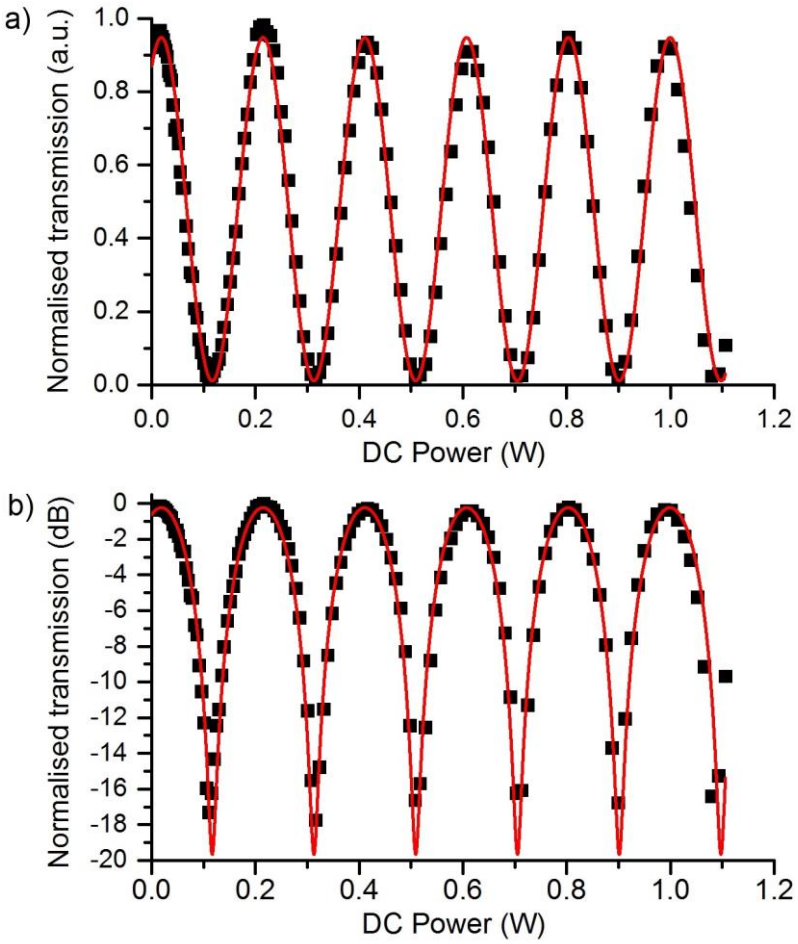

Fig. 6.4. Normalised optical transmission through an asymmetric spiral arm thermo-optic modulator, plotted (black squares) against the applied DC power (W). In this case the heated spiral is 1.77mm long and the arm length difference is 96.1µm. The red curve curve shows the fitted theoretical response of an asymmetric MZI with an applied phase shift. a) Linear y-axis scale, b) transmission plotted in decibels.

The refractive index change of the Si waveguide is proportional to the temperature change, and the temperature of the device can be expected to be proportional to the thermal power generated by the heater. The response of an MZI to an applied phase change, when there is loss in the arms of the device is governed by equation 6.1 [3].

$$\eta = \frac{P_o}{P_{in}} = \frac{1}{4}\left[\tau_1^2 + \tau_2^2 + 2\tau_1\tau_2\cos(\Delta\phi)\right] \qquad \text{Eq. 6.1}$$

Where $\Delta\phi$ is the phase change, and $\tau_i^2 = exp(-\alpha_i L_i)$ for arm i, and α_i is the absorption coefficient in arm i and L_i is the length of arm i. A function of the form has been fitted to the measured data (blue dots) in fig. 6.4, and has been plotted on the figure.

The extinction ratios of the fabricated devices were calculated from the measured DC response curves. For the straight arm MZIs the average extinction ratio was 24.1dB, and the greatest measured extinction ratio was 30.5dB. For spiral arm MZIs the average was 10.9dB and the maximum was 17.8dB. These results are approximately consistent with the extinction ratios measured from spectral scans of the passive devices. That there is no degradation of the extinction ratio is an indication that significant added loss has not been introduced due to the presence of the silica layer or metal heaters. The power required for a π-phase shift, which results in a transition from an optical "1" at the output to a "0", has been extracted from the measured DC scans by fitting curves of the form of eq. 6.1, and calculating the switching power from the fitted parameters. Fig. 6.5 shows the results of switching power measurements for straight arm MZIs with 15µm wide heating strips of varying length, and S_{met}=1µm, plotted alongside the switching powers for spiral arm MZIs, with 10µm wide heating strips separated by 2µm gaps, above spirals with an inner bend radius of 20µm and 27.5µm, and varying lengths.

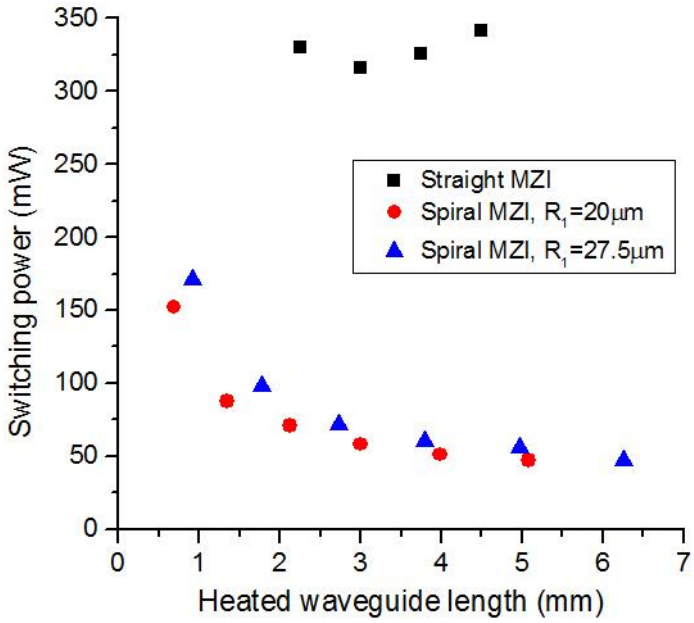

Fig. 6.5. Switching power of straight arm MZIs (black squares) and of spiral arm MZIs with R_1=20µm (red circles) and with R_1=27.5µm (blue triangles), plotted for varying heated waveguide length. The spirals have between one (shortest) and six loops (longest).

Fig. 6.5 demonstrates that the switching power of straight arm MZIs remains approximately constant as the length of heated waveguide is increased, whereas for

spiral arm MZIs the switching power can be reduced by increasing the heated waveguide length. The switching powers overall are also significantly larger for straight-arm MZIs in this case than for spiral arm-MZIs. This can be attributed largely to the lateral separation of the heating wires in the straight-arm MZI case, and there is evidence of this in the difference in the switching powers of devices with W_{met}=10µm and W_{met}=15µm. Two devices with W_{met}=10µm, having L=2250µm and L=3000µm exhibited switching powers of 245mW and 248mW respectively, while devices with W_{met}=15µm exhibited switching powers of 317mW and 318mW for the same lengths. The larger switching power for the wider heaters is due to the average position of the heaters being further away from the waveguide, so that a greater proportion of the generated heat is dissipated away from the waveguide. It is expected that reducing the thickness of the SiO_2 isolating layer or placing a single heating strip directly above the waveguide would significantly reduce the switching power of these devices.

In the case of spiral arm MZIs, their efficiency could be improved by increasing the spatial overlap between the heating wire and the spiral waveguide. It can be seen in fig. 6.3 that there is a large area at the centre of the spiral where the heater is placed above etched silicon, and power used for heating this area is wasted. Fig. 6.6 also shows that the switching powers of devices with a 20µm spiral inner bend radius are smaller than those with a 27.5µm radius, and fig. 6.7 confirms this trend with switching power measurements of devices with different bend radii, but the same number of spiral loops. Even with a large inner bend radius the device efficiency could be improved by using a different heater design in which the heater does not pass over the central area of the spiral.

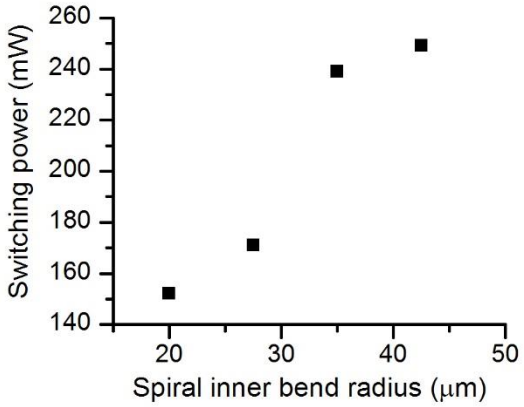

Fig. 6.7. The switching power of spiral-arm MZI thermo-optic modulators with varying inner bend radius. All four devices have the same number of spiral loops, waveguide width and gap between waveguides.

The bandwidth of the devices was determined by measuring the optical transmission of the devices when a square wave of sufficient magnitude to induce a π-phase shift and of varying frequency was applied to the device. Because the thermal power generated by the heaters is proportional to the magnitude of the electrical power applied to the heaters, in order to generate an optical signal with the applied frequency a DC offset must be applied to the electrical signal. Otherwise the optical signal would have double the frequency of the trigger signal that is passed to the lock-in amplifier, which would filter out this optical signal. For this measurement the mechanical chopper was removed from the optical path, and was in effect replaced by the on-chip modulator. The lock-in amplifier measured the amplitude of the square wave signal received by the detector, and the signal generator that applied the AC signal to the modulator also passed a reference signal to the lock-in amplifier, so that only signals at the modulation frequency were measured. Scans were performed through a LabView controlled script, which varied the AC square wave frequency and simultaneously recorded the magnitude of the lock-in amplifier output. Fig. 6.8 shows an example of results from an AC scan, where optical transmission, normalised to the maximum transmission measured during the scan, has been plotted against frequency for a straight-arm MZI with a 2.25mm long heater and 10μm wide heating strips.

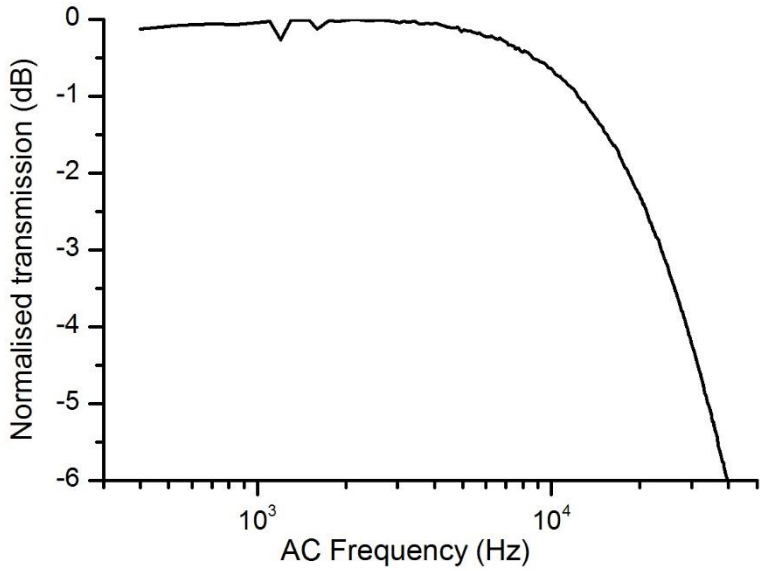

Fig. 6.8. Normalised optical transmission for a straight-arm MZI, with a 2.25mm heater length and 10µm heater width, when an AC signal of varying frequency is applied to it.

The -3dB bandwidth of the measurement shown in fig. 6.8 is 23.8kHz. Across the devices of both straight-arm and spiral-arm types, and with varying heater widths, there was relatively little variation in the measured bandwidths, which were between 17.8kHz and 23.8kHz, and no clear trend was discernible from the data, regardless of straight-arm or spiral-arm configuration. The authors of ref. [2], who achieved a -3dB frequency cut-off of ~25kHz for spiral devices in the NIR also noted that lateral heat diffusion has little effect on the frequency response, and predicted that reducing the BOX thickness would improve the switching speed, by improving heat diffusion away from the device. However, the 2µm thick BOX used for these MIR devices is already at a minimum acceptable thickness for suppressing substrate leakage, and in fact, as was discussed in chapter 4, increasing the BOX thickness would be desirable to improve waveguide losses.

6.5. Summary

The thermo-optic modulators presented in this chapter are the first demonstrations of optical modulation in silicon based modulators beyond 3µm. Devices with modulation frequencies up to 23.8kHz have been demonstrated, which is similar to speeds achieved in NIR devices of the same type. These speeds are not fast enough for data

communications or related applications, but could be useful for integrated sensing systems. The demonstrated devices were based on MZIs of two types, those with straight arms and those with spiral arms. The straight-arm MZIs were shown in the previous chapter to have lower insertion losses when used as passive devices, and to exhibit higher extinction ratios in both optical and electrical testing. The spiral-armed devices however, were demonstrated to require lower power for modulation, due to the increased length of waveguide per unit heated volume in this configuration. The lowest measured switching power for straight-arm MZIs was 245mW, and for spiral-arm MZIs was 47mW, which is still higher than the switching power for straight arm MZIs in the NIR [2]. There are a few factors that result in increased switching powers in the MIR. Firstly, the thermo-optic coefficient in silicon is approximately 8% weaker at λ=3.8μm than at 1.55μm. Secondly, the SiO_2 layer that is deposited on the chip surface to isolate the waveguide mode from loss at the metal heaters must be thicker at longer wavelengths, due to the larger mode size. For the straight-arm MZIs that have been demonstrated here the power consumption could be reduced by reducing the SiO_2 cladding thickness, and by placing the heaters directly above the waveguide, instead of separating them laterally. Finally, for spiral-arm MZIs the radius of the bends of the spiral must be larger at longer wavelengths to maintain low insertion loss, therefore there must be a reduced length of waveguide per unit heated volume. The power efficiency of both device types can be improved, but it can be reasonably expected that the power consumption of thermo-optic modulators in the MIR will ultimately be larger than for similar devices in the NIR. Across the measured devices only relatively small variation in the frequency response was observed, which suggests that lateral heat diffusion is not the limiting factor of the modulation frequency. Reducing the BOX layer thickness may increase the device bandwidth, but in the MIR this would increase an unacceptable penalty in terms of waveguide loss due to substrate leakage.

Silicon thermo-optic modulators for the MIR therefore appear to be capable of attaining similar speeds to similar NIR modulators, but there is a penalty as power consumption must increase with increasing wavelength. The device architecture that has been used for the device in this chapter could be applied with minor modifications to most material platforms where silicon is used as the waveguide core material, and the thermo-optic

effect could also be applied to germanium waveguides, where the effect is even stronger than in silicon [4]. The modulation bandwidth that has been achieved is expected to be sufficient for on-chip signal processing functions. However, faster operation may be required for some communications related applications, for which modulators exploiting the free-carrier plasma dispersion effect would be needed.

Chapter 7: The plasma dispersion effect in silicon - calculating design equations for the MIR

In chapter 6 silicon modulators based on the thermo-optic effect, operating in the MIR were demonstrated. While relatively simple to fabricate, ultimately such devices are limited to modulation frequencies on the order of 10s of kHz. For applications where faster modulation is essential devices based on the free-carrier plasma dispersion effect will be required. In the literature review device types based on this effect were briefly introduced, and it was stated that the design equations commonly used to quantify the magnitude of the effect in silicon are only applicable at the most frequently used telecommunications wavelengths. This chapter is therefore concerned with the development of such equations for wavelengths throughout the NIR and MIR, here defined as 1.3-14μm, so that in future designers of silicon modulators for the MIR might have all of the required tools. Above approximately 7μm the absorption of intrinsic silicon will likely be too large for use as a waveguide core material, but it could still be used as a cladding material, and equations for the 7-14μm range may prove useful for some applications. This absorption above 7μm is partly due to absorption by impurities in the silicon, and partly due to multiphonon absorption processes, which result when multiple phonons interact simultaneously to form an electric dipole moment with which an optical electric field can interact [1].

In chapter 2 simple Drude theory was introduced as a basic estimate of the plasma dispersion effect, and after a review of available literature it was concluded that in practice it is an insufficiently accurate method for the calculation of the electroabsorption and electrorefraction effects due to charge carriers. The equations of Soref and Bennett [2] for λ=1.3μm and 1.55μm have become a standard and accurate tool for the design of NIR modulators, therefore their approach is used here to calculate expression for change in absorption coefficient, Δα, and change in refractive index, Δn, as a function of the change in electron concentration ΔN_e and hole concentration ΔN_h for wavelengths between 1.3μm and 14μm. The literature absorption spectra should

take into account all of the free-carrier related absorption processes that were described in chapter 2. In the first part of this chapter the details of this method will be introduced, which will be followed by the results of the calculations for MIR wavelengths, and by a discussion of the consequences of these results for plasma dispersion based devices in the MIR.

7.1 The Soref and Bennett equations

The Soref and Bennett (SB) equations for change in free-carrier absorption with the injection of electrons and holes were calculated by surveying the literature to find existing optical absorption spectra for silicon samples with different levels of doping [2]. The effect of doping is to introduce either electrons or holes into the silicon sample depending on the type of doping. In their approach SB assume that charge carriers introduced into a silicon wafer through doping are equivalent to charge carriers introduced into a device through injection. Table 7.1 below shows a list of each literature source and the wavelength range for which it supplies absorption spectra.

Table 7.1. List of literature sources for absorption spectra data. All experimental data were measured at 300°K.

Photon energy range (Wavelength range)	**Data source**	**Notes**
0.001eV – ~0.1eV (1.24mm – ~12.4μm)	Schumann *et al.* [3] and Walles and Boija [4].	Balkanski and Besson [5] note saturation of α from 50-87μm, and Randal and Rawcliffe [6] observe a flat spectrum from 100μm to 500μm. Schumann theoretical data, passing through Walles and Boija's data points, provide an α vs ΔN curve at 87μm, which is used to determine saturation level.
~0.1eV – 0.6eV (~12.4μm – 2.06μm)	*n*-type: Spitzer and Fan [7] *p*-type: None	For both *n* and *p* type silicon Schmid's [8] data for 0.6eV- 1.5eV are extrapolated over this range. For *n*-type Si, the spectral shape of Spitzer and Fan's data is used. For *p*-type Si, a λ^2 extrapolation of Schmid's data is used.
0.6eV – 1.5eV (2.06μm – 0.83 μm)	Schmid [8] experimental spectra.	Schmid measured *n* and *p* type spectra for samples with impurity concentrations in the 10^{18}-10^{20} range.
1.5eV – 2.8eV (0.83 μm – 443nm)	Dash and Newman [9].	Dash and Newman provided the spectrum of intrinsic silicon. The doped curves were extrapolated to join the undoped spectrum in this range.

These data were collected to construct composite curves for change in absorption with different concentrations of electrons and holes, and the resultant composite curves from [2] were shown in chapter 2. These curves have been digitized, and are plotted in figs. 7.1a and 7.1b.

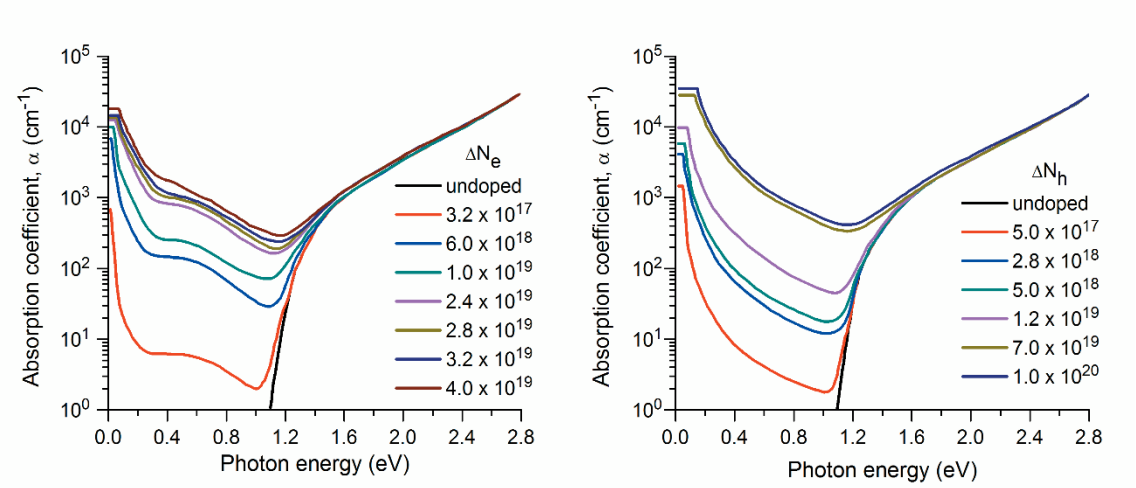

Fig. 7.1. Optical absorption spectra of doped silicon with different concentrations of a) n-type and b) p-type doping.

A basic description of the behaviour of silicon free-carrier dependent absorption is that for holes the curves approximately follow a $\alpha \propto \lambda^2$ in the NIR and MIR (~0.1-0.9eV). At wavelengths lower than the fundamental gap (1.24eV), the absorption is dominated by the fundamental absorption, and all of the doped silicon absorption curves meet the intrinsic silicon curve. In the far-infrared (~<0.1eV), there is a saturation of the absorption, and it can be assumed that the absorption levels off in this range. This saturation occurs because at long wavelengths the energy of incoming photons becomes smaller than the energy of the phonons required to assist in the indirect absorption processes. N-type silicon follows similar behaviour, with the difference that there is an absorption band, due to inter-conduction band absorption, in the NIR and MIR, which was discussed in chapter 2.

To obtain an expression for the change in absorption with change in electron or hole concentration at a particular wavelength, the undoped sample absorption spectrum can be subtracted from each of the doped spectra. Using x-y lines the change in absorption coefficient is plotted against the carrier concentration. A line of best fit can then be drawn, with the equation of the line giving the numerical relationship.

The same absorption spectra are used to calculate the relationship between carrier concentration and refractive index change. The analysis is based on the Kramers-Kronig coupling between the real and imaginary parts of the refractive index of a material (i.e.

the real part of the refractive index, Δn, and the absorption coefficient, $\Delta\propto$), as described by equation 7.1.

$$\Delta n(\omega) = (c/\pi)\, P \int_0^\infty \frac{\Delta\propto(\omega')d\omega'}{\omega'^2 - \omega^2} \qquad \text{Eq. 7.1}$$

Where $\hbar\omega$ is the photon energy. *P* indicates that to evaluate the integral it is necessary to use contour integration because there is a singularity at $\omega' = \omega$. This can be rewritten in terms of the normalized photon energy, *V*, which is defined as $V = \hbar\omega/e$, where *e* is the electronic charge.

$$\Delta n(V) = 6.3 \times 10^{-6} cm \cdot \mathrm{V}\, P \int_0^\infty \frac{\Delta\propto(V')dV'}{V'^2 - V^2} \qquad \text{Eq. 7.2}$$

However, using a trapezoid-rule approximation to perform the integration numerically avoids the singularity [10].

I. First, the absorption spectra are digitised, to create a set of points with co-ordinates $(\alpha_m\ ,\ V_m)$, for m=1 to M, where M is the total number of digitised points.

II. To find the change in absorption coefficient the undoped data is subtracted from each of the doped data points, to create a set of points with co-ordinates $(\Delta\alpha_m\ ,\ V_m)$, for m=1 to M, where M is the total number of digitised points.

III. A set of data points $(a(i)\ ,\ V'(i))$ is calculated for i=1 to M-1, where each point is the linearly interpolated midpoint between successive $(\Delta\alpha_m\ ,\ V_m)$ points. $\delta(i)$ is also calculated, where it is the difference in photon energy between successive $(\Delta\alpha_m\ ,\ V_m)$ points, as in fig. 7.2.

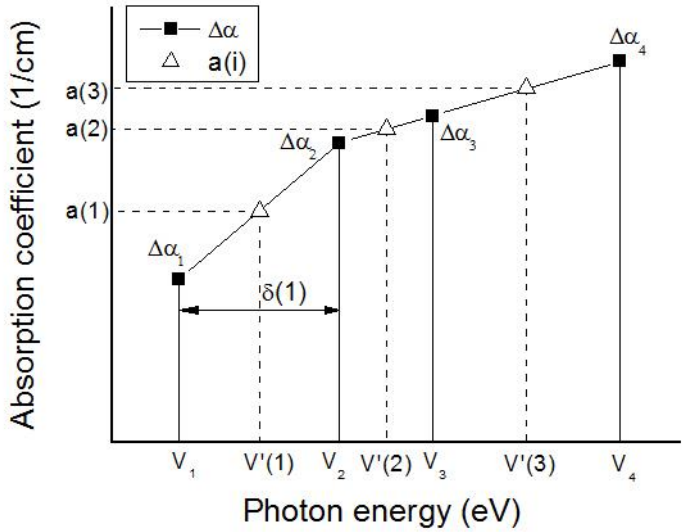

Fig. 7.2. Variable names used in the numerical Kramers-Kronig integration.

IV. The Kramers-Kronig integral is calculated for each $(\Delta\alpha_m\ ,\ V_m)$ point to find the change in refractive index, Δn_m, at each point, as given in equation 7.3:

$$\Delta n_m(V_m) = 6.3 \times 10^{-6} \sum_{i=1}^{M-1} \frac{\delta[i]a[i]}{V'[i]^2 - V_m^2} \qquad \text{Eq. 7.3}$$

The result is change in refractive index spectra.

7.2 Extending the Soref and Bennett equations into the MIR

Since the publication of the SB paper new data has become available for the far-infrared absorption saturation levels for heavily doped p-type silicon [11]. The spectra of fig. 7.1b have been adjusted to incorporate the new data. The above process has been performed using the above steps, and the initial results can be seen in fig. 7.3 and fig. 7.4, which show the change in absorption coefficient index spectra for electrons and holes respectively with varying charge carrier concentrations, over the 1.3-14µm wavelength range, and in fig. 7.5 and fig. 7.6, which show the change in refractive index spectra over the same wavelength range.

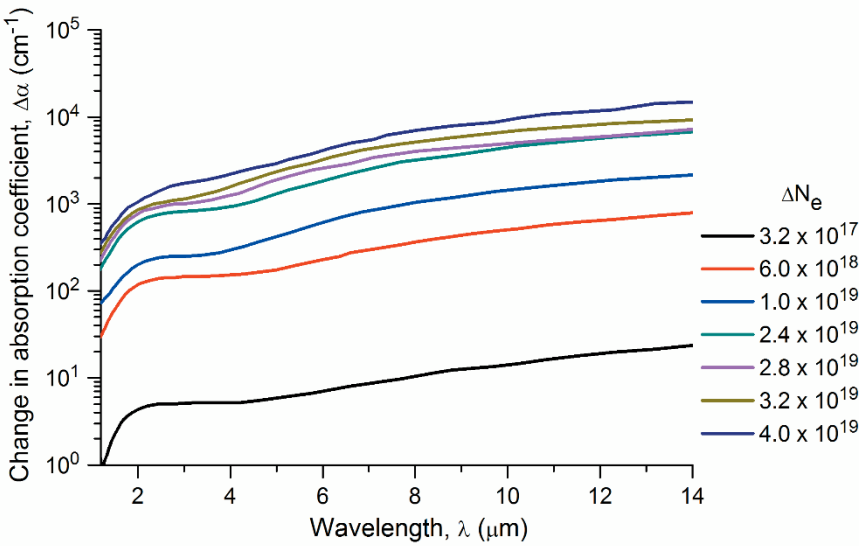

Fig. 7.3. Change in absorption coefficient, Δα (cm^{-1}), for different electron concentrations in the 1.3-14μm wavelength range.

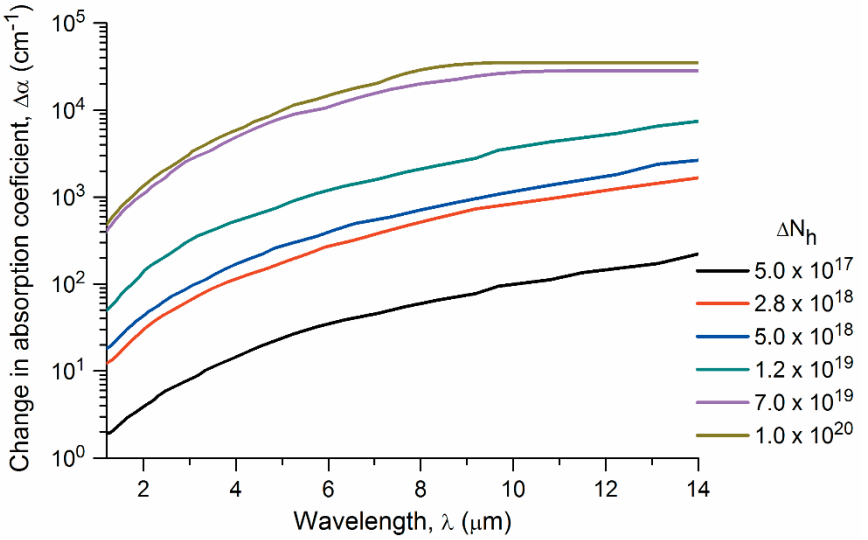

Fig. 7.4. Change in absorption coefficient, Δα (cm^{-1}), for different hole concentrations in the 1.3-14μm wavelength range.

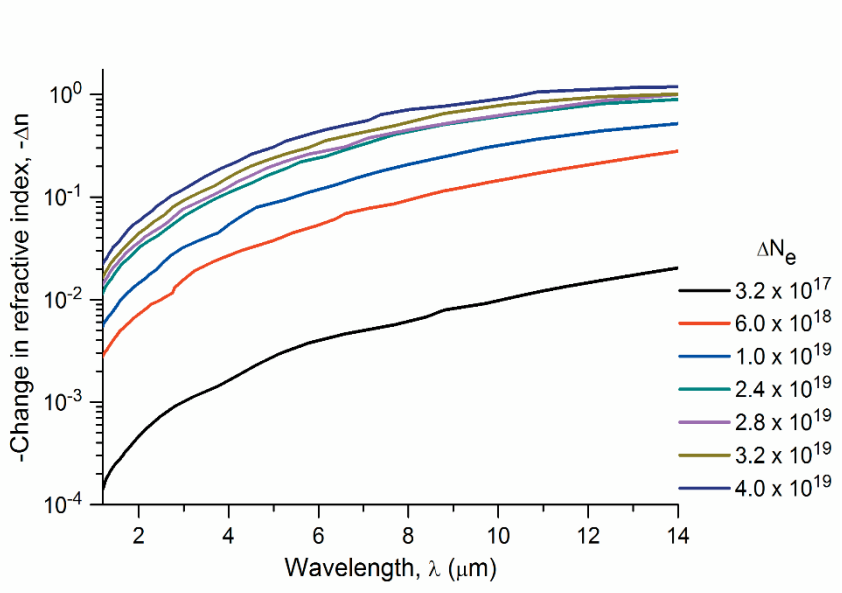

Fig. 7.5. Change in refractive index, -Δn, for different electron concentrations in the 1.3-14μm wavelength range.

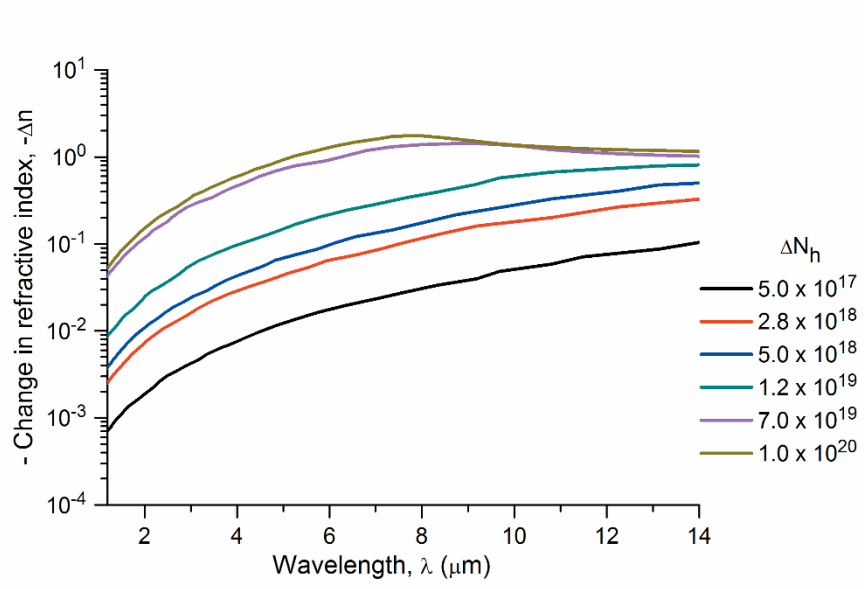

Fig. 7.6. Change in refractive index, -Δn, for different hole concentrations in the 1.3-14μm wavelength range.

The spectra of figures 7.3-7.6 have been used to calculate relationships for $\Delta\alpha$ vs. ΔN and $-\Delta n$ vs. ΔN at specific wavelengths throughout the plotted ranges. Figs. 7.7 and 7.8 show examples of such plots for the absorption coefficients for electrons and holes respectively. Curves of least squares fits to the data have been plotted in the same figures. Due to saturation of the change in absorption in the far-infrared, the two highest

carrier concentration points in figures. 7.8c and 7.10c sit below the fitted line, as do the four highest point in fig. 7.9c. These high concentration points have been omitted from the fits of $\lambda \geq 11\mu m$ for -Δn vs. ΔN_e, $\lambda \geq 9\mu m$ for Δα vs. ΔN_h and $\lambda \geq 8\mu m$ for -Δn vs. ΔN_h. Therefore the fitted lines are only valid above these wavelengths at $\Delta N_h \leq 1.2E19$ for Δα vs. ΔN_h, at $\Delta Ne \leq 1E19$ for -Δn vs. ΔN_e, and $\Delta N_h \leq 1.2E19$ for -Δn vs. ΔN_h.

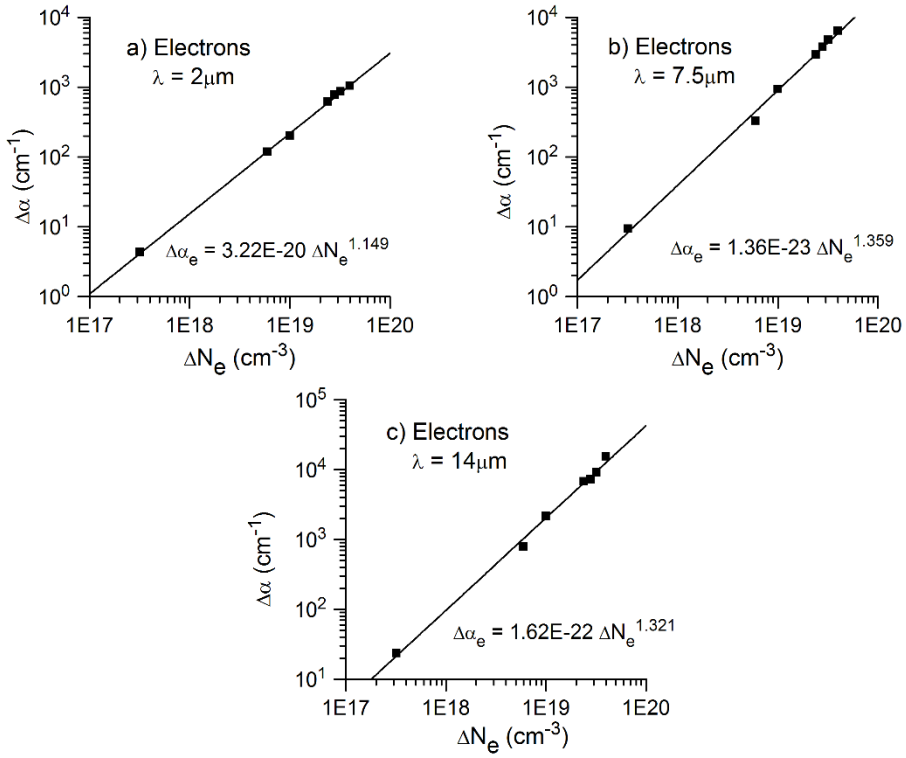

Fig. 7.7. Absorption coefficient in silicon plotted as a function of electron concentration for a) λ=2μm, b) λ=7.5μm and c) λ=14μm.

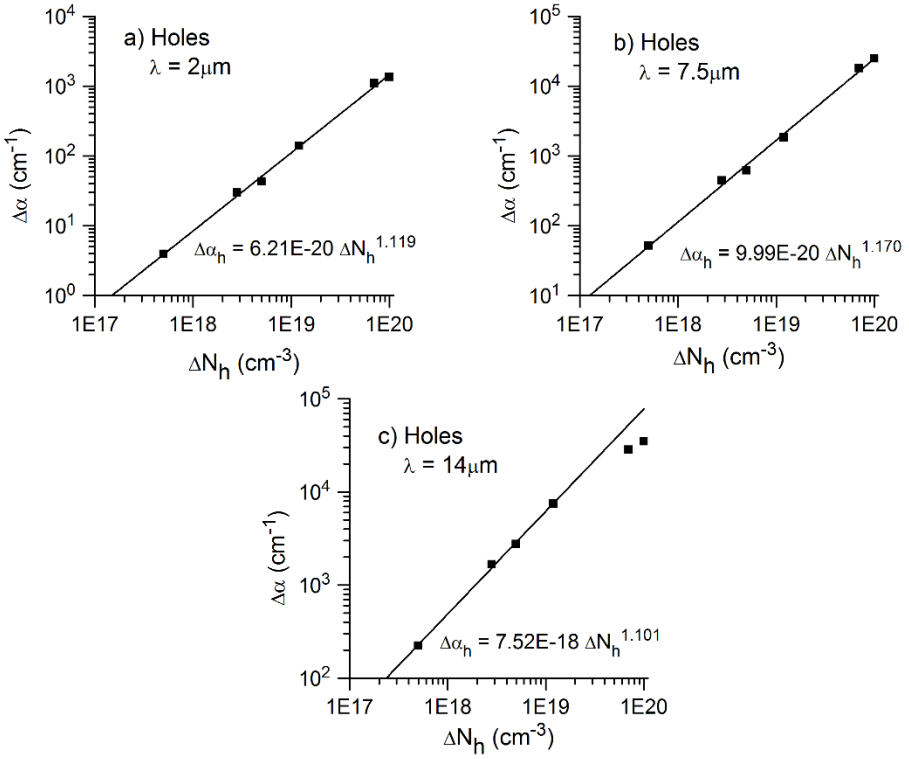

Fig. 7.8. Absorption coefficient in silicon plotted as a function of hole concentration for a) λ=2μm, b) λ=7.5μm and c) λ=14μm.

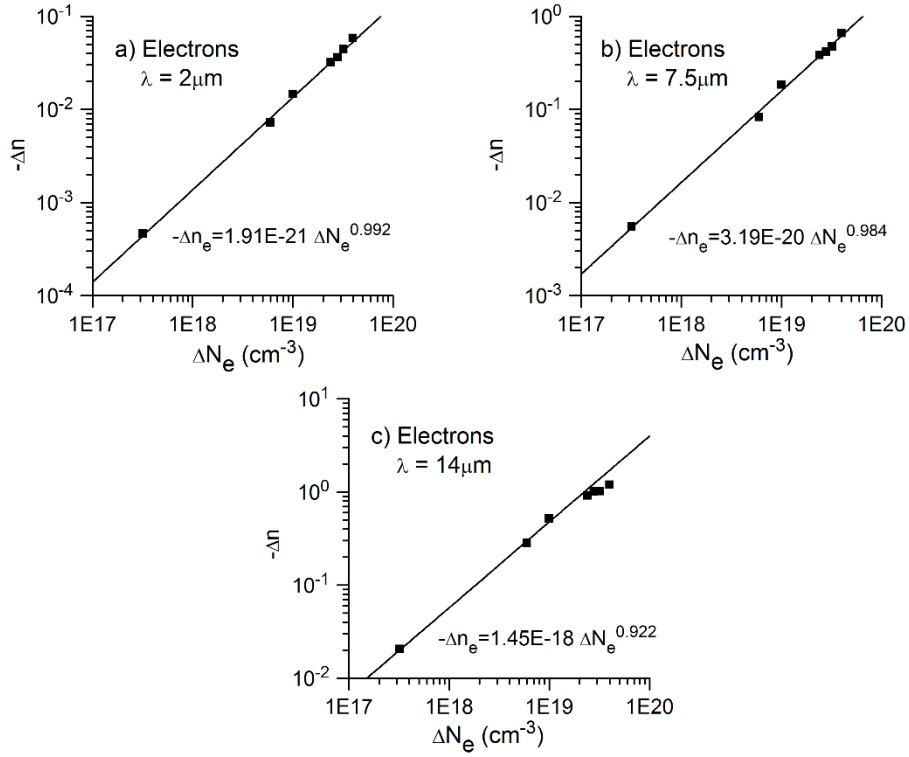

Fig. 7.9. Refractive index change in silicon plotted as a function of change in electron concentration for a) λ=2μm, b) λ=7.5μm and c) λ=14μm.

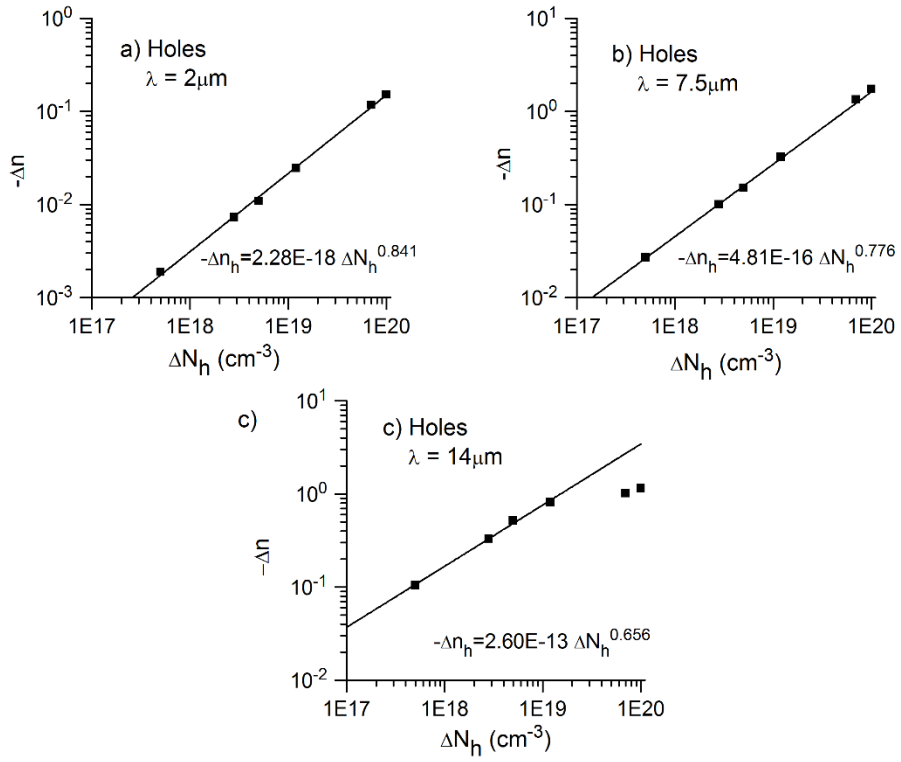

Fig. 7.10. Refractive index change in silicon plotted as a function of change in hole concentration for a) λ=2μm, b) λ=7.5μm and c) λ=14μm.

From the fitting parameters of the lines of best fit the coefficients for equations for equations for Δα vs. ΔN and -Δn vs. ΔN have been found. The generalised equations are of the form:

$$\Delta\alpha(\lambda) = \Delta\alpha_e(\lambda) + \Delta\alpha_h(\lambda) = a(\lambda)\Delta N_e^{b(\lambda)} + c(\lambda)\Delta N_h^{d(\lambda)} \quad \text{Eq. 7.4}$$

$$-\Delta n(\lambda) = \Delta n_e(\lambda) + \Delta n_h(\lambda) = p(\lambda)\Delta N_e^{q(\lambda)} + r(\lambda)\Delta N_h^{s(\lambda)} \quad \text{Eq. 7.5}$$

Where *a*, *b*, *c*, *d*, *p*, *q*, *r* and *s* are the fitted coefficients, whose values can be found in table 7.2 for wavelengths between 1.3μm and 14μm.

Table 7.2. Coefficients of eq. 7.4 and eq. 7.5 for wavelengths between 1.3μm and 14μm, which relate Δα and –Δn to ΔN_e and ΔN_h.

Wavelength,	Δα (cm^{-1})				-Δn			
λ (μm)	*a* (cm^2)	*b*	*c* (cm^2)	*d*	*p* (cm^3)	*q*	*r* (cm^3)	*s*
1.3	3.48E-22	1.229	1.02E-19	1.089	2.98E-22	1.016	1.25E-18	0.835
1.55	8.88E-21	1.167	5.84E-20	1.109	5.40E-22	1.011	1.53E-18	0.838
2.0	3.22E-20	1.149	6.21E-20	1.119	1.91E-21	0.992	2.28E-18	0.841
2.5	1.67E-20	1.169	8.08E-20	1.123	5.70E-21	0.976	5.19E-18	0.832
3.0	6.29E-21	1.193	3.40E-20	1.151	6.57E-21	0.981	3.62E-18	0.849
3.5	3.10E-21	1.210	6.05E-20	1.145	6.95E-21	0.986	9.28E-18	0.834
4.0	7.45E-22	1.245	5.43E-20	1.153	7.25E-21	0.991	9.99E-18	0.839
4.5	2.16E-22	1.277	5.58E-20	1.158	1.19E-20	0.985	1.29E-17	0.838
5.0	9.28E-23	1.299	6.65E-20	1.160	2.46E-20	0.973	2.03E-17	0.833
5.5	4.58E-23	1.319	8.53E-20	1.159	3.64E-20	0.968	3.31E-17	0.826
6.0	3.26E-23	1.330	1.53E-19	1.149	4.96E-20	0.965	6.92E-17	0.812
6.5	2.70E-23	1.338	1.22E-19	1.158	5.91E-20	0.964	8.23E-17	0.812
7.0	2.25E-23	1.345	1.29E-19	1.160	5.52E-20	0.969	1.15E-16	0.807
7.5	1.36E-23	1.359	9.99E-20	1.170	3.19E-20	0.984	4.81E-16	0.776
8.0	1.85E-23	1.354	1.32E-19	1.167	3.56E-20	0.984	7.44E-16	0.769
8.5	3.05E-23	1.345	1.57E-18	1.111	8.65E-20	0.966	7.11E-16	0.774
9.0	4.08E-23	1.340	1.45E-18	1.115	2.09E-19	0.948	5.29E-16	0.783
9.5	4.14E-23	1.341	1.70E-18	1.115	2.07E-19	0.951	9.72E-16	0.772
10.0	3.81E-23	1.344	1.25E-18	1.125	3.01E-19	0.944	1.22E-15	0.769
10.5	4.23E-23	1.344	8.14E-19	1.137	5.07E-19	0.934	1.16E-15	0.772
11.0	5.81E-23	1.338	1.55E-18	1.124	1.51E-19	0.965	3.16E-15	0.750
11.5	8.20E-23	1.331	4.81E-18	1.100	2.19E-19	0.958	1.51E-14	0.716
12.0	1.13E-22	1.325	4.72E-18	1.102	3.04E-19	0.953	2.71E-14	0.704
12.5	1.22E-22	1.324	2.09E-18	1.124	4.44E-19	0.945	2.65E-14	0.706
13.0	1.09E-22	1.328	1.16E-18	1.140	6.96E-19	0.936	2.94E-14	0.705
13.5	1.20E-22	1.327	2.01E-18	1.130	1.05E-18	0.928	6.85E-14	0.686
14.0	1.62E-22	1.321	7.52E-18	1.101	1.45E-18	0.922	2.60E-13	0.656

There are clearly significant variations of all of these coefficients across the wavelength range, and from simple Drude theory a, c, p and r would be expected to increase as wavelength increase. However, under Drude theory the power dependence (i.e. b, d, q and s) would equal 1. In fact the power dependence of electron absorption varies from

approximately 1.15 to 1.35, and for holes from 1.09 to 1.17. The power dependence of change in refractive index decreases with increasing wavelength for both electrons (1.02-0.92) and holes (0.84-0.66). In general, holes are more effective than electrons at altering the refractive index for low ΔN. The new data for the far-infrared absorption of p-type silicon result in only modestly different equations for the change in refractive index at telecommunications wavelengths compared to those from [2] that are widely used.

An important inconsistency arises between the data at telecommunications wavelengths for change in absorption coefficient, and equations for Δα vs. ΔN_e and ΔN_h that have appeared in numerous literature sources, i.e. [12-15], among others, which cite [2] as the source of the absorption equations, although the equations in fact do not appear there. These equations are:

For λ=1.3μm: $\Delta\alpha = \Delta\alpha_e + \Delta\alpha_h = 6.0 \times 10^{-18}\Delta N_e + 4.0 \times 10^{-18}\Delta N_h$ Eq. 7.6

For λ=1.55μm: $\Delta\alpha = \Delta\alpha_e + \Delta\alpha_h = 8.5 \times 10^{-18}\Delta N_e + 6.0 \times 10^{-18}\Delta N_h$ Eq. 7.7

Figs. 7.11a-d show the absorption data plotted at 1.3μm and 1.55μm for electrons and holes, alongside the lines described by eq. 7.6 and eq. 7.7, and alongside the lines calculated from eq. 7.4 and the appropriate coefficients from table 7.1 of this work.

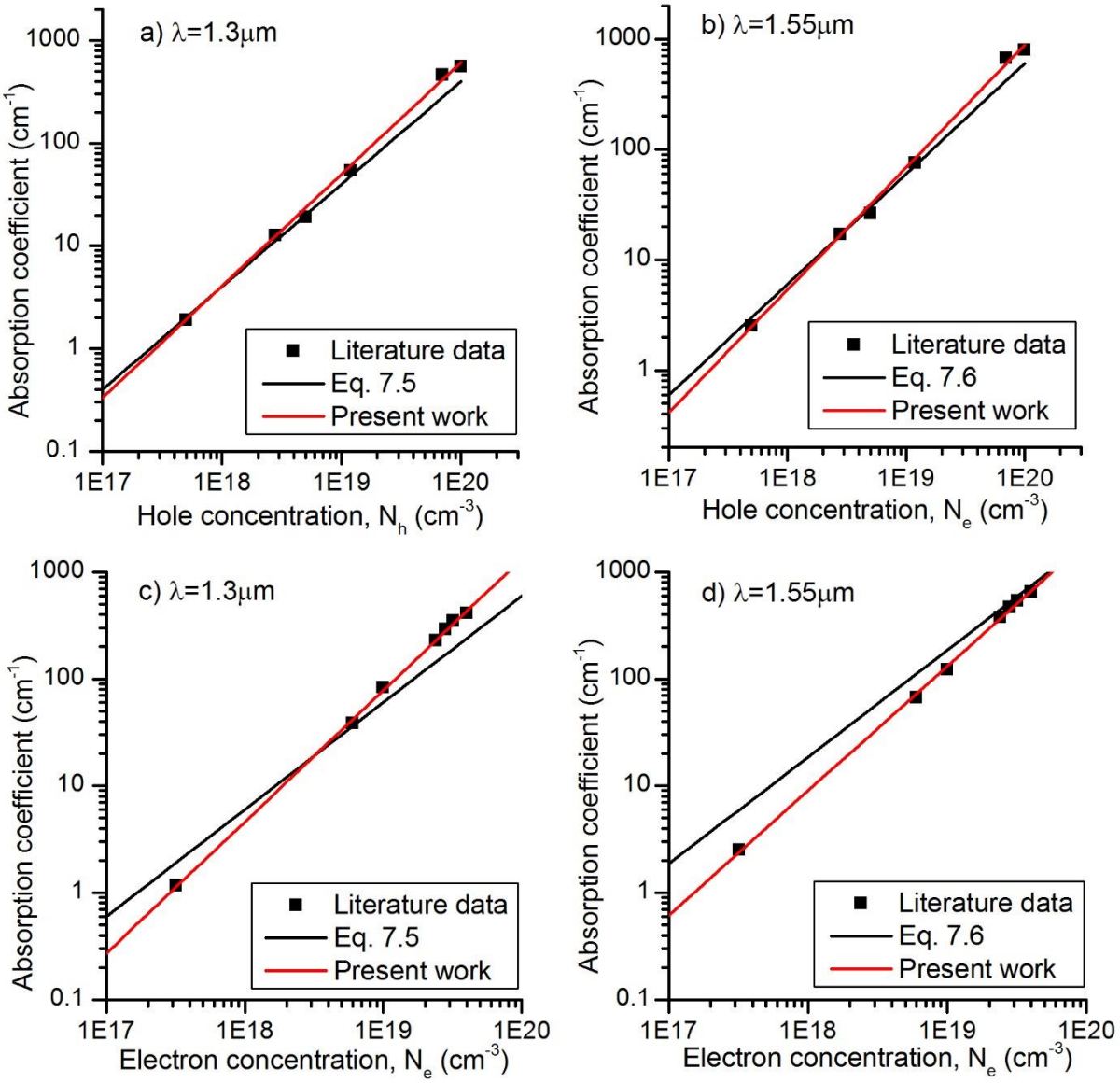

Fig. 7.11. Comparison of literature data from [2], equations 7.5 and 7.6, and the fitted curves presented in this work from equation 7.3 and table 7.1, for a) holes at 1.3μm, b) holes at 1.55μm, c) electrons at 1.3μm, and d) electrons at 1.55μm.

Fig. 7.11 makes clear that the power dependence of the absorption data is not equal to 1, and that equations 7.6 and 7.7 only very approximately match the literature data to which they are supposed to be lines of best fit.

7.3 Discussion: implications for MIR modulators

The design of Si modulators for the MIR will in many cases be different to those in the NIR. At telecoms wavelengths electrorefraction is the dominant mechanism, and modulators are built around structures that convert the phase change resulting from a change in carrier concentration to an intensity change. This can be called a "phase-dominant" approach. In such structures the accompanying absorption coefficient change, Δα, is unwanted, as in a MZI based modulator it introduces excess insertion loss and reduces the device extinction ratio. Longer wavelength structures may operate best in an electroabsorption dominant mode, due to a change in the ratio of Δn to Δα. Both Δn and Δα increase rapidly with increasing wavelength, and when both electro-absorption and electro-refraction increase, the electro-absorption component usually dominates. This point is illustrated in table 7.3, which shows the refractive index change for an injected hole concentration of 10^{17} at λ=1.55μm, 4μm and 10μm, as well as the required length for a waveguide to induce a π-phase shift for that carrier concentration, and the resultant loss in the waveguide.

Table 7.3: Wavelength dependent change in refractive index, π-phase shift length, and absorption loss in waveguide of π-phase shift length, for a change in hole concentration $\Delta N_h = 10^{17}$.

λ (μm)	$-\Delta n$	L_π (cm)	$\Delta\alpha$ (cm^{-1})	Absorption loss in waveguide with length L_π (dB)
1.55	1.70×10^{-4}	0.287	0.416	0.552
4	1.83×10^{-3}	0.109	2.17	1.17
10	1.44×10^{-2}	0.0347	16.7	3.72

The large increase in refractive index change absorption coefficient change at longer wavelengths means that very short modulators are possible at longer wavelengths. However, in a MZI where there is carrier-injection into one arm, the optical loss in that arm degrades the extinction ratio. At 1.55μm this degradation is tolerable, but at 4μm becomes a major factor, and at 10μm becomes crippling. On the other hand, a useful intensity modulator could operate simply through carrier injection into a straight

waveguide. Therefore for approximately λ>3μm silicon plasma dispersion effect based modulators should be modified to operate as electroabsorption modulators.

As a result of the work in this chapter design equations necessary for modelling of silicon plasma dispersion effect based devices in the MIR have been made available. It is expected that devices based on this effect will be able to operate at MHz and GHz frequencies, and that the design of these devices will likely differ from those in the NIR.

Chapter 8: Conclusions and future work

Group-IV photonics looks likely to play a role in the realisation of compact, portable mid-infrared (MIR) sensors for applications such as chemical and biological sensing, environmental monitoring, and gas detection. For example, MIR Ge-on-Si waveguides have already been used as sensors for cocaine detection [1]. There is however a clear need to develop waveguides that are capable of operating with low losses throughout the MIR, because SOI waveguides that are used for conventional NIR silicon photonics are highly absorbing at wavelengths greater than 4µm. In the literature review (chapter 2) demonstrations of MIR waveguides to date were discussed, and it can be concluded that no standard material platforms have so far emerged for the mid-infrared, and that further work is needed to develop waveguides for all regions of the MIR.

MIR passive and active components that will form the building blocks of future integrated photonic sensing circuits also need to be developed, as their design in many cases changes as the operating wavelength is increased. Modulators are often a key optoelectronic component in photonic systems, and in mid-infrared sensors they could be used for improving the sensitivity of sensing systems, or they may find use for data communications in the short-wave infrared (SWIR, 2-3µm). However, until now there have been no demonstrations of waveguide integrated silicon based modulators at wavelengths above 3µm. Additionally, while most NIR silicon modulators utilise the plasma dispersion effect for modulation, accurate equations for predicting the effect in the MIR have not been available in the literature.

In this project waveguides based on silicon-on-insulator (SOI), poly-silicon on SOI, and germanium-on-silicon (Ge-on-Si) waveguides have been demonstrated at the 3.8µm wavelength. SOI single mode rib waveguides fabricated using SOI wafers with H=400nm, D=220nm, H_{BOX}=2000nm and W=1350nm were experimentally measured to have losses less than 2.0dB/cm, which is the lowest reported loss for SOI waveguides in the MIR. This result shows that SOI waveguides are likely to be the material platform of choice for most wavelengths up to 3.8µm, and maybe slightly beyond. The SOI waveguides

were based on used the same wafers and the same fabrication steps that are used for fabrication of standard NIR silicon photonic components, which provides a possible route to inexpensive chip fabrication, where fabrication runs can be shared between NIR and MIR photonics, and conceivably NIR and MIR silicon photonic components could be realised on the same chip. Analysis of the sources of loss of the SOI waveguides suggested that SiO_2 absorption, scattering due to sidewall roughness and leakage into the substrate all contribute to the loss. Mode simulations indicated that the substrate leakage could be almost completely reduced by increasing the thickness of the BOX layer to >2.5µm. SOI wafers with thicker BOX layers are commercially available, and their use would not adversely impact the performance of NIR components fabricated on the same wafer. Measurements of SOI waveguides at λ=1.55µm, which were fabricated using identical wafers and the same fabrication process, showed that the loss was smaller for the MIR waveguides than NIR waveguides (5.4dB/cm). This is thought to be due to the λ^{-4} dependence of Rayleigh scattering, which is usually the dominant scattering mechanism in waveguides. However, careful simulation of the loss due to scattering is required, and should be conducted in the future, as it is difficult to establish what proportion of the optical mode interacts with the sidewalls in each case. Measurements at more wavelengths in the MIR could help to establish what this wavelength dependence is in practice, and would assist the design of waveguides for other material platforms.

Poly-Si on SOI waveguides were fabricated using the *imec* Advanced Passives process, at *imec* (Leuven, Belgium). This is a commercially available platform for the fabrication of NIR silicon photonics that allows components with both 220nm and ~400nm Si thicknesses to be fabricated alongside each other. The overall dimensions of these waveguides, including all layers of the waveguide core material stack, were D=380nm, H=220nm, W=1100nm, and H_{BOX}=2µm. The measured loss at 3.8µm was 7.6dB/cm. Recent measurements of similar waveguides in the literature [2] suggest that the loss of these waveguides could be reduced by increasing their width to 1.3µm, which would still satisfy the single mode condition, and that scattering due to defects in the poly-Si layer contributes significantly to the total loss. Further experiments should be conducted to find out how much the loss could be reduced by increasing the waveguide width.

Substrate leakage and SiO_2 absorption in the BOX layer and top oxide cladding layers also contributed to the loss. The propagation loss of these waveguides would be expected to be greater than for equivalent crystalline silicon even if their width were to be increased. However, their successful demonstration in this material platform is important as a route to relatively cheap fabrication through this commercially available Multi Project Wafer service, without any adjustments for the production of MIR waveguides.

The transmission ranges of both SOI and poly-Si on SOI waveguides are ultimately limited by SiO_2 absorption to λ < ~4μm. Ge-on-Si waveguides however, are an exciting option for low loss waveguides throughout a large part of the MIR. Ge has low loss (<2dB/cm) throughout the 2-14μm wavelength range, and Si has losses <15dB throughout this wavelength region. With careful design the optical mode confinement in the Si lower cladding could be kept very small at those wavelengths where Si absorption is too large for Si to be used as the waveguide core material. In this project Ge-on-Si waveguides, which were designed and fabricated at the University of Gent, and which were based on Ge-on-Si wafers that were made at *imec*, were measured to have propagation losses as low as 6dB/cm at 3.8μm. The dimensions of the waveguides with this loss were H=1μm, D=0.7μm and W=2.25μm. Loss measurements of waveguides with different widths revealed a strong dependence of the loss on waveguide width, which is an indicator that a large part of the loss is due to sidewall scattering. Waveguides fabricated from the same material and using the same processes have been shown to have losses of only 2.3-3.5dB/cm at λ=5.15-5.45μm [3]. The reduction in loss at the longer wavelength is thought to be due to the λ^{-4} dependence of Rayleigh scattering. Further investigation is required to determine whether the Ge-on-Si waveguide loss can be reduced through optimisation of the etch process or through surface roughness reduction techniques. It will also be important to determine whether defects in the crystalline Ge waveguide core are responsible for a significant portion of the loss. An obvious next step for Ge-on-Si waveguides would be to characterise their performance at longer wavelengths; so far the longest wavelength demonstration of germanium waveguides has been at 5.8μm [4]. Their performance at wavelengths where Si absorption becomes significant (λ > ~7μm) would be particularly interesting.

In the literature review it was identified that for silicon modulators, whether those employing the thermo-optic effect or those using the plasma dispersion effect, a component that can convert a refractive index change to optical intensity change is required. Therefore, in order to demonstrate a modulator based on SOI, asymmetric 1×1 Mach-Zehnder interferometers, which used the SOI waveguides that were characterised in this project, were designed, fabricated and characterised. In order to split the input light to the MZI into its two arms, and then couple the two arms together at its output, a multimode interferometer were developed to serve as the coupler/splitter. The demonstrated SOI MMI, which was fabricated at the University of Southampton, was based on SOI with H=400nm, D=220nm, and H_{BOX}=2µm. It exhibited an insertion loss of only 0.10±0.01dB, which was similar to the expected loss from simulations (0.12dB). This very low loss rivals the lowest published losses in the NIR (0.20dB) [5]. A second SOI MMI was also demonstrated that had the same dimensions, but that had an etch depth of 350nm, and which was fabricated at the University of Glasgow. The measured loss was 0.25±0.02dB, which was only slightly higher than its simulated loss of 0.19dB. A third MMI was demonstrated for the poly-Si on SOI material platform, which also had the same dimensions. Its measured loss was 0.37±0.08dB, which was approximately 0.16dB larger than was expected from simulations. It is thought that this excess loss was due to scattering in the poly-Si material.

The MZIs that were demonstrated were designed in two different configurations: those with conventional straight arms, and those with spiral waveguides in each arm. Folding a waveguide into a spiral shape is an efficient way of placing a long waveguide into a small area of a chip. Spiral-arm MZIs have been used in the NIR for small footprint sensors [6] and for efficient thermo-optic modulators [7]. Straight-arm MZIs were characterised which were based both on SOI waveguides with a 220nm deep etch (fabricated at Southampton), and on waveguides with a 350nm etch (fabricated at Glasgow). The insertion loss of the Southampton devices was 1.3-2.2dB, and the largest measured extinction ratio was 28dB. For the Glasgow devices the insertion loss was 1.6-2.4dB, and the extinction ratio was up to 25dB. A comparison of the group index from simulations (n_g=4.03) and a group index value calculated from fits to experimental free spectral range measurements for the Glasgow MZIs (n_g=4.20), revealed a small

discrepancy between the two values. However, it is clear that the design techniques that have been used are valid for MIR wavelengths. Asymmetric spiral-arm MZIs were fabricated at the University of Southampton, which had varying numbers of spiral loops, and varying inner bend radii. Asymmetry was created by placing a spiral with one more loop in one of the arms than in the other. All of the measured spiral-arm MZIs exhibited greater insertion losses (3.1-9.2dB) and smaller maximum extinction ratios (7.9-21.0dB) than the straight-arm MZIs. This suggests that the bent waveguides in the spiral introduce excess loss, which degrades both the device extinction ratio and insertion loss (e.g. for R=30µm the bend loss was ~9dB/cm, compared to straight waveguide loss of 3.5dB/cm). Bend loss measurements for the same waveguides confirm that the bends introduce excess loss compared to straight waveguides. In comparison to the NIR, the MIR density of waveguides in the spiral is limited by the larger mode size, and therefore greater minimum bend radius. Using a deeper etch could reduce the minimum bend radius, and further work could include investigating whether smaller spirals with low insertion loss could be achieved using strip waveguides.

The MZIs that have been demonstrated can be used as the basis for either silicon modulators based on the thermo-optic effect or for modulators based on the free-carrier plasma dispersion effect. Thermo-optic modulators are devices in which a heater is used to produce a temperature change, which changes the refractive index in silicon. At 3.8µm the size of this effect is approximately 8% weaker than at 1.55µm, which is nevertheless strong enough to produce useful devices. The advantage of silicon thermo-optic modulators compared to plasma dispersion effect modulators is that their fabrication requires considerably fewer steps. Thermo-optic modulators have been fabricated by patterning metal heaters over one of the asymmetric MZI arms of both the straight-arm and spiral-arm MZIs that were made at the University of Southampton. The aluminium heaters were isolated from the waveguide modes by a layer of SiO_2. They were tested to determine their performance on application of both DC and AC electrical signals. The optical extinction ratios of the modulators when a DC current was applied to them were similar to the optical extinction ratios of the passive asymmetric MZIs (maximum ER of 31dB for straight-arm MZI, and maximum ER of 18dB for spiral-arm MZIs). The power required to create a π-phase shift and change the MZI output from a

“1” to a “0” was highly dependent on the MZI geometry. In general, the straight-arm MZIs required much greater switching powers than the spiral-arm MZI (minimum 245mW for straight-arm MZIs, minimum 47mW for spiral-arm MZIs). For the straight-arm MZIs heaters were placed with a lateral 1µm edge to edge separation away from the waveguide, and some of the devices had wider heating strips than others. Those with wider heating strips required greater switching powers, because the average position of the heaters was further away from the waveguide, therefore a smaller proportion of the thermal power was being used for heating the waveguide. The power efficiency of the straight-arm MZIs could be reduced by placing the heating strips directly above the waveguide, or by using a thinner SiO_2 isolating layer, or both. To achieve better optimised devices experimental investigation of the impact of the reduction of the SiO_2 thickness on waveguide loss would be necessary.

The power efficiency of spiral-arm MZIs was greater for devices with more spiral loops, and for those that had smaller inner bend radii, which increased waveguide density below the heater. The spiral arm MZIs were more efficient than straight-arm MZIs because when the arm length of a straight-arm MZI is increased, the heater length must be increased proportionally, which also increases the power required to heat the whole arm to the same temperature. In a spiral, when the arm length is increased the heater length is not required to increase by the same amount. The result is that there is a better overlap between the waveguides and the heated volume of the chip, and generated heat is used more efficiently. The efficiency of the spiral-armed modulators could still be improved further by altering the pattern of the heating strip, which in this case was folded above the spiral, but in a way such that the etched central region of the spiral was being heated unnecessarily. A heater pattern that more closely follows the waveguide spiral could be designed, and should be more efficient. It would also be beneficial to investigate more thoroughly the experimental relationship between propagation loss and bend radius for these waveguides, so that for future designs the trade-off between device insertion loss and spiral area, and therefore switching power, can be better understood. Ultimately, the power efficiency of MIR silicon thermo-optic modulators will always be smaller than for their NIR equivalents. The optical mode of a MIR waveguide will be less confined, therefore metal heaters will need to be placed

further away, and spirals will be larger. Additionally, the thermo-optic effect decreases slightly in the MIR.

The largest measured -3dB bandwidth of the measured modulators under AC modulation was 23.8kHz, which is similar to the speeds of similar modulators in the NIR. The modulation bandwidth did not vary much depending on waveguide and heater design, and suggests that lateral heat diffusion is not a limiting factor for the device speed. This agrees with NIR measurements of Densmore *et al.* [7], who also predict that using a thinner BOX layer would increase the device speed. Unfortunately, this is not an option for these MIR waveguides, as there is already some excess loss due to substrate leakage, and reducing the BOX thickness would only exacerbate the problem. Simulations of the heat transfer processes are needed to determine how and how much the modulation bandwidth could be reduced.

Thermo-optic modulators for the MIR will likely always be limited to speeds on the order of 10-100kHz. For greater bandwidths modulators utilizing the free-carrier plasma dispersion effect, which is commonly used for NIR modulation, are required. However, a major impediment to their use has been a lack of accurate design equations for predicting the size of the effect at mid-infrared wavelengths. In this project a semi-empirical approach was used, which was the same as that used to calculate equations for the size of the same effect at NIR wavelengths [8]. The resulting NIR equations have become a standard tool for designers of NIR silicon modulators. The aim was to produce equations that could predict the change in absorption coefficient ($\Delta\alpha$), and the change in refractive index ($-\Delta n$), for a given change in electron and hole concentration (ΔN_e and ΔN_h respectively), at wavelengths throughout the mid-IR. To calculate the equations, absorption spectra for doped silicon wafers were gathered from the literature, which allowed the $\Delta\alpha$ vs. ΔN relationships to be extracted at the desired wavelengths. To find the refractive index change, Kramers-Kronig integration was applied to the absorption spectra at each doping density, which resulted in a set of refractive index change spectra. From these spectra Δn vs. ΔN relationships were extracted. More recent absorption spectra for p-type Si were included in the data set, and were used to update the NIR expressions of [8]. The result of this work is a set of simple equations that can

be applied at wavelengths between 1.3μm and 14μm, and it is hoped will enable future demonstrations of silicon plasma dispersion effect modulators at wavelengths >4μm.

The results of these calculations show clearly that the size of the plasma dispersion effect increases strongly with increasing wavelength, and is approximately proportional to λ^2. Some conclusions can be drawn concerning the consequences of these results. One is that much shorter modulators should be possible at longer wavelengths. A second is that as both electroabsorption ($\Delta\alpha$) and electrorefraction (Δn) increase, the electroabsorption will begin to dominate. This is because, in a modulator that relies on using the refractive index change to produce a phase-shift in one arm of a MZI, the increased electrorefraction will mean that only a short phase shifter is required, but the accompanying absorption increase will be detrimental to the device insertion loss and extinction ratio. However, the device design could be changed to rely on the electroabsorption, for example carrier injection into a straight waveguide would produce a useful intensity modulator. It could be expected that at wavelengths greater than 3μm electroabsorption modulators would be more effective than electrorefraction modulators. The clear next step for this direction of research is experimental demonstration of MIR plasma dispersion effect modulators, either operating by carrier injection or carrier depletion. The equations calculated in this work must be verified experimentally before they can be considered to be accurate. There are also likely to be significant differences between the NIR and MIR design of structures for both carrier injection and carrier depletion that require consideration. For example, in a MIR carrier injection modulator based around a PIN junction, where the silicon waveguide core is the intrinsic region and heavily doped P and N contact regions are placed to its side, the heavily doped contact areas would have to be further away from the waveguide core to ensure low insertion loss. The resulting device would therefore have a smaller modulation bandwidth than its NIR equivalent, due to the longer time required to inject carriers into the waveguide core.

Overall, mid-infrared group-IV photonics is a rich area for future research. Several possible directions for future work are listed here.

- *Group-IV material waveguide platforms:* In the literature review published results to date for group-IV material waveguides were discussed. Waveguides have been demonstrated in silicon-on-insulator, silicon-on-sapphire, silicon membrane (with an air lower cladding), silicon on silicon nitride, silicon nitride on silica, and germanium on silicon. However, there are clear problems with all of the demonstrated waveguides, many of which are related to limited material transmission ranges. Ge-on-Si is expected to have the widest transmission ranges, but the longest wavelength at which it has so far been demonstrated is 5.6μm [3], and silicon has high absorption for λ>7μm. SiGe-on-Si, GeSn-on-Si, and germanium membrane waveguides are just a few of the other material platforms that could be investigated. The suspended Ge platform is particularly interesting as it would utilise the full transparency range of Ge. In addition, the Ge on chalcogenide platform would have the same transparency range with the advantage of having a solid bottom cladding. Ge on porous Ge is another potential candidate for the fingerprint region.

- *Germanium photonics:* Germanium is part of all of the material platforms suggested above, and is likely to be a key material for MIR group-IV photonics. However, many of its material properties are not yet well known. For example, the plasma dispersion effect is likely to be very useful for modulation, but as with silicon, accurate equations for the plasma dispersion effect in Ge are not available. There are also many areas relating to the fabrication of Ge devices that need to be investigated, for example relating to its growth and etching. Even when problems such as these have been mastered, design of both passive and active components operating in Ge will in many cases be different to those in Si.

- *Photonic components for the 8-14μm "fingerprint region":* Group-IV photonics has not yet addressed the 8-14μm wavelength "fingerprint region", which is of particular importance for biomedical applications, as it contains absorption bands unique to particular biomolecular compounds. Other applications for this wavelength range include toxic chemical detection for homeland security.

However, it will be a non-trivial task to assemble a setup for characterisation of components in this wavelength range.

- *Integrated sources and detectors:* In chapter 1 schematic diagrams of ideas for integrated photonic sensing systems were presented. To produce a complete "lab-on-a-chip" system, integrated sources and detectors would be needed, or at the very least, inexpensive, power efficient and compact sources and detectors, which could be integrated into the same packaging. Bonding of III-V material sources and detectors onto a group-IV chip is a possibility, as is using a broadband source and using filters or demultiplexers to select the wavelengths that are of interest for sensing.

- *Integrated sensing systems:* When there are sufficient discrete components to form a complete system, integration of these components will still be a big challenge, and an even bigger one lies in creating viable, reliable sensing systems. For example, methods for manipulation of an analyte, such as microfluidics, will be required.

In this thesis the field of mid-infrared group-IV photonics has been advanced through the development of low loss silicon waveguides for the 3.8µm wavelength, and demonstration of poly-Si and Ge-on-Si waveguides at a new wavelength. The passives components required to create modulators, namely multimode interferometers, were fabricated and characterisation revealed device performance that rivals NIR devices of the same type. The first waveguide integrated group-IV modulator for wavelengths greater than 3µm was achieved, which was based on the thermo-optic effect. Finally, design equations for prediction of the free-carrier plasma dispersion effect in silicon were calculated, which will enable demonstrations of much faster silicon modulators in the future.

Appendix: Group-IV material platforms data

Table 1: Materials and wavelength ranges of operation for group-IV material platforms proposed in [a].

Waveguide type	Core material		Lower cladding		Upper cladding		Wavelength range of operation (μm) (1-20μm limits)
	Material	Ref. Index[1]	Material	Ref. Index[1]	Material	Ref. Index[1]	
$Si/SiO_2/Si$ (SOI)	Si	3.4	a-SiO2	1.4	Air	1.0	1.2-2.6; 2.9-3.7
$Si/Al_2O_3/Si$ (SOS)	Si	3.4	Sapphire	1.74	Air	1.0	1.2-4.4
$Si/Si_3N_4/Si$ (SON)	Si	3.4	a-Silicon nitride[2]	1.6-2.8	Air	1.0	1.2-6.7
Si Membrane	Si	3.4	Air	1.0	Air	1.0	1.2-8
SiGe/Si	$Si_{0.5}Ge_{0.5}$	3.7	Si	3.4	Air	1.0	1.6-12
Ge/Si	Ge	4.0	Si	3.4	Air	1.0	1.9-16.8
GeSn/Si	$Ge_{0.8}Sn_{0.2}$	4.388[4]	Si	3.4	Air	1.0	2.2-19[5]

1. Refractive index values for all materials, where possible, are taken at λ=1.55μm, and should be used with caution in the mid-infrared; some of these materials, e.g. sapphire [b], have high dispersion across the MIR.
2. Silicon Nitride refractive index varies significantly depending on deposition conditions, and Si to N ratio in the deposited material [c].
3. The refractive index of $Si_{0.5}Ge_{0.5}$ has been calculated from the mean of the c-Si and c-Ge refractive indices.
4. The refractive index of $Ge_{0.8}Sn_{0.2}$ [d] is based on theoretical data which is only available for λ > 7.7μm.
5. Transmission range of GeSn has been predicted in [a], and is not based on absorption spectra data.

References:

a) R. A. Soref and B. R. Bennett, "Electrooptical effects in silicon," IEEE Jour. of. Quant. Elec., vol. 23, no. 1, 123-129 (1987).
b) I. H. Malitson, F. V. Murphy Jr., and W. Rodney, "Refractive index of synthetic sapphire," J. Opt. Sci. Am., vol. 48, no. 1, 72-73 (1958).
c) D. H. Yoon, S. G. Yoon, Y. T. Kim, "Refractive index and etched structure of silicon nitride waveguides fabricated by PECVD," Thin Solid Films, 515, 5004-5007 (2007).

d) M. Sahnoun, R. Khenata, H. Baltache, M. Rerat, M. Driz, B. Bouhafs, B. Abbar, “First-principles calculations of optical properties of GeC, SnC and GeSn under hydrostatic pressure,” Physica B, 355, 392-400 (2005).

References

Chapter 1

1. G. T. Reed, G. Z. Mashanovich, F. Y. Gardes, and D. J. Thomson, “Silicon optical modulators,” Nature photonics, vol. 4, 518–526 (2010).
2. G. T. Reed, “Silicon Photonics: The state of the art,” Wiley, 2008.
3. D. A. B. Miller, “Device Requirements for optical interconnects to silicon chips,” Proceedings of the IEEE, vol. 97, no.9, 1166-1185 (2009).
4. F. K. Tittel, D. Richter, and A. Fried, “Mid-infrared laser applications in spectroscopy,” in Solid-State Mid-Infrared Laser Sources, Topics Appl. Phys. 89, 445–510 (2003).
5. R. W. Waynant, I. K. Ilev and I. Gannot, “Mid-infrared laser applications in medicine and biology,” Phil. Trans. R. Soc. Lond. A , 359, 635–644 (2001).
6. B. Mizaikoff, “Mid-infrared evanescent wave sensors – a novel approach for subsea momitoring,” Meas. Sci. Technol., vol. 10, 1185–1194 (1999).
7. S.Aleksandrov, G.Gavrilov, A.Kapralov, S.Karandashov, B.Matveev, G.Sothikova, and N. Stus, “Portable optoelectronic gas sensors operating in the mid-IR spectral range (λ=3-5μm),” 2nd International Conference on Lasers for Measurements and Information Transfer, Proceedings of SPIE Vol. 4680, 188-194 (2002).
8. P. Werle, F. Slemr, K. Maurer, R. Kormann, R. Mucke, B. Janker, “Near- and mid-infrared laser-optical sensors for gas analysis,” Optics and Lasers in Engineering, vol. 37, 101-114 (2002) .
9. R. A. Soref, S. J. Emelett, and W. R. Buchwald, “Silicon waveguided components for the long-wave infrared region,” J. Opt. A: Pure Appl. Opt., vol. 8, 840848 (2006).
10. R. A. Soref and B. R. Bennett, “Electrooptical effects in silicon,” IEEE Jour. of. Quant. Elec., vol. 23, no. 1, 123-129 (1987).
11. N. K. Hon, R. Soref, and B. Jalali, “The third-order nonlinear optical coefficients of Si, Ge, and $Si_{1-x}Ge_x$ in the midwave and longwave infrared,” J. Appl. Phys., vol. 110, 011301 (2011).
12. Xiaoping Liu, Richard M. Osgood, Jr, Yurii A. Vlasov & William M. J. Green, “Mid-infrared optical parametric amplifier using silicon nanophotonic waveguides,” Nature Photonics, vol. 4, 557 - 560 (2010).
13. Thorlabs, http://www.thorlabs.de/.

14. IRflex corporation, http://www.irflex.com/.
15. R. A. Soref, “Towards silicon-based longwave integrated optoelectronics (LIO),” J. Opt. A: Pre Appl. Opt., vol. 8, 840-848 (2006).
16. R. A. Soref, “Mid-infrared photonics in silicon and germanium,” Nature Photonics, vol. 4, 495-497 (2010).
17. R. A. Soref, “Group IV photonics for the mid-infrared,” SPIE Photonics West, (2013).

Chapter 2

1. X. Xia, Q. Chen, C. B. Arnold, and C. K. Madsen, “Low-loss chalcogenide waveguides on lithium niobate for the mid-infrared,” Opt. Letters, vol. 35, no. 19, 3228-3230 (2010).
2. C. Tsay, E. Mujagic, C. K. Madsen, C. F. Gmachl, and C. B. Arnold, “Mid-infrared characterization of solution-processed As_2S_3 chalcogenide glass waveguides,” Opt. Express, vol. 18, no. 15, 15523-15530 (2010).
3. C. Vigreux-Bercovici, L. Labadie, J.E. Broquin, P. Kern, and A. Pradel, “Selenide and telluride thick films for mid and thermal infrared applications,” Jour. of Optoelec. and Adv. Mat.,vol. 7, no. 5, 2625-2634 (2005).
4. O. Eyal, V. Scharf, S. Shalem, and A. Katzir, “Single-mode mid-infrared silver halide planar waveguides,” Opt. Letters, vol. 21, no. 5, (1996).
5. G. T. Reed, “Silicon Photonics: The state of the art,” Wiley, 2008.
6. G. T. Reed and A. P. Knights, “Silicon photonics: an introduction” Wiley, 2004.
7. S. K. Selvaraja, W. Bogaerts, P. Absil, D. V. Thourhout, and R. Baets, “Record low-loss hybrid rib/wire waveguides for silicon photonic circuits,” Group IV Photonics, 7th International conference, Proceedings, Beijing, China (2010).
8. D. J. Thomson, F. Y. Gardes, Y. Hu, G. Mashanovich, M. Fournier, P. Grosse, J-M. Fedeli, and G. T. Reed, “High contrast 40Gbit/s optical modulation in silicon,” Opt. Express, vol. 19, no. 12, 11507-11516 (2011).
9. P. Dumon, W. Bogaerts, V. Wiaux, J. Wouters, S. Beckx, J. Van Campenhout, D. Taillert, B. Luyssaerts, P. Bientsman, D. Van Thourhout, and R. Baets, “Low-loss SOI photonic wires and ring resonators fabricated with deep UV Lithography,” IEEE Phot. Tech. Letters, vol. 16, no. 5, 1328-1330 (2004).

10. R. Kitamura, L. Pilon, and M. Jonasz, “Optical constants of silica glass from extreme ultraviolet to far infrared at near room temperature,” Appl. Optics, vol. 46, no. 33, 8118-8133 (2007).
11. R. A. Soref, S. J. Emelett, and W. R. Buchwald, “Silicon waveguided components for the long-wave infrared region,” J. Opt. A: Pure Appl. Opt 8, 840848 (2006).
12. M. A. Green, “Self-consistent optical parameters of intrinsic silicon at 300 K including temperature coefficients,” Solar Energy Materials & Solar Cells, vol. 92, no. 11, 1305–1310 (2008).
13. G. Z. Mashanovich, M. M. Milošević, M. Nedeljkovic, N. Owens, B. Xiong, E. J. Teo, and Y. Hu, “Low loss silicon waveguides for the mid-infrared,” Opt. Express, vol. 19, no. 8, 7112-7119 (2011).
14. M. M. Milošević, M. Nedeljkovic, T. M. Ben Masaud, E. Jaberansary, H. M. H. Chong, N. G. Emerson, G. T. Reed, and G. Z. Mashanovich, “Silicon waveguides and devices for the mid-infrared,” Appl. Phys. Letters, 101, 121105 (2012).
15. M. Muneeb, X. Chen, P. Verheyen, G. Lepage, S. Pathak, E. Ryckeboer, A. Malik, B. Kuyken, M. Nedeljkovic, J. Van Campenhout, G. Z. Mashanovich, and G. Roelkens, “Demonstration of Silicon-on-insulator mid-infrared spectrometers operating at 3.8μm,” Opt. Express, vo. 21, no. 10, 11659-11669 (2013).
16. T. Baehr-Jones, A. Spott, R. Ilic, A. Spott, B. Penkov, W. Asher, and M. Hochberg, “Silicon-on-sapphire integrated waveguides for the mid-infrared,” Opt. Express, vol. 18, no. 12, 12127-12135 (2010).
17. F. Li, S. D. Jackson, C. Grillet, E. Magi, D. Hudson, S. J. Madden, Y. Moghe, C. O’Brien, A. Read, S. G. Duvall, P. Atanackovic, B. J. Eggleton, and D. J. Moss, “Low propagation loss silicon-on-sapphire waveguides for the mid-infrared,” Opt. Express, vo. 19, no. 16, 15212-15220 (2011).
18. A. Spott, Y. Liu, T. Baehr-Jones, R. Ilic, and M. Hochberg, “Silicon waveguides and ring resonators at 5.5μm,” Appl. Phys. Lett., 97, 213501 (2010).
19. D. J. Thomson, M. Milosevic, D. C. Cox, F. Y. Gardes, M. Nedeljkovic, J.-M. Fedeli, G. Z. Mashanovich, and G. T. Reed, “Focused ion beam processing of active and passive silicon photonic devices,” ECIO 2012, Barcelona, Spain, (2012).
20. P. Y. Yang, G. Z. Mashanovich, I. Gomez-Morilla, W. R. Headley, G. T. Reed, E. J. Teo, D. J. Blackwood, M. B. H. Breese, and A. A. Bettiol, "Free standing waveguides in silicon," Appl. Phys. Lett., 90, 241109, (2007).

21. Z. Cheng, X. Chen, C. Y. Wong, K. Xu, and H. K. Tsang, “Mid-infrared suspended membrane waveguide and ring resonator on silicon-on-Insulator,” IEEE. Phot. Journal, vol. 4, no. 5 (2012).
22. Y. Wei, G. Li, Y. Hao, Y. Li, J. Yang, M. Wang, and X. Jiang, “Long-wave infrared 1 × 2 MMI based on air-gap beneath silicon rib waveguides,” Opt. Express, vol. 19, no. 17, 15803-15809 (2011).
23. D. H. Yoon, S. G. Yoon, Y. T. Kim, “Refractive index and etched structure of silicon nitride waveguides fabricated by PECVD,” Thin Solid Films, 515, 5004-5007 (2007).
24. S. Khan, J. Chiles, J. Ma, and S. Fathpour, “Silicon-on-nitride waveguides for mid- and near-infrared integrated photonics,” Appl. Phys. Lett., 102, 121104 (2013).
25. P. T. Lin, V. Singh, L. Kimerling, A. M. Agarwal, “Planar silicon nitride mid-infrared devices,” Appl. Phys. Lett. 102, 251121 (2013).
26. Y-C. Chang, V. Paeder, L. Hvozdara, J-M. Hartmann, and H. P. Herzig, “Low-loss germanium strip waveguides on silicon for the mid-infrared,” Opt. Letters, vol. 37, no. 14, 2883-2885 (2012).
27. J. M. Hartmann, A. Abbadie, N. Cherkashin, H. Grampeix, and L. Clavelier, “Epitaxial growth of Ge thick layers on nominal and 6° off Si(0 0 1); Ge surface passivation by Si,” Semicond. Sci. Technol., 24, 055002 (2009).
28. G. Roelkens, U. Dave, A. Gassenq, N. Hattasan, C. Hu, B. Kuyken, F. Leo, A. Malik, M. Muneeb, E. Ryckeboer, S. Uvin, Z. Hens, R. Baets, Y. Shimura, F. Gencarelli, B. Vincent, R. Loo, J. Van Campenhout, L. Cerutti, J. Rodriguez, E. Tournié, X. Chen, M. Nedeljkovic, G. Mashanovich, L. Shen, N. Healy, A. Peacock, X. Liu, R. Osgood, and W. Green, "Silicon-based heterogeneous photonic integrated circuits for the mid-infrared," Opt. Mater. Express, vol. 3, no. 9, 1523-1536 (2013).
29. A. Malik, M. Muneeb, S. Pathak, Y. Shimura, J. Van Campenhout, R. Loo, G. Roelkens, "Germanium-on-Silicon Mid-Infrared Arrayed Waveguide Grating Multiplexers," Photonics Technology Letters, vol.25, no.18, 1805-1808 (2013).
30. W. C. Dash and R. Newman, “Intrinsic Optical Absorption in Single-Crystal Germanium and Silicon at 77°K and 300°K,” Phys. Review, vol. 99, no. 4, 1151-1155 (1955).
31. A. Malik, M. Muneeb, Y. Shimura, J. Van Campenhout, R. Loo, G. Roelkens, “Germanium-on-silicon planar concave grating wavelength (de)multiplexers in the mid-infrared,” Applied Physics Letters, vol. 103, 161119 (2013).
32. G. Roelkens, U. Dave, A. Gassenq, N. Hattasan, C. Hu, B. Kuyken, F. Leo, A. Malik, M. Muneeb, E. Ryckeboer, S. Uvin, Z. Hens, R. Baets, Y. Shimura, F. Gencarelli, B. Vincent,

R. Loo, J. Van Campenhout, L. Cerutti, J. Rodriguez, E. Tournié, X. Chen, M. Nedeljkovic, G. Mashanovich, L. Shen, N. Healy, A. Peacock, X. Liu, R. Osgood, and W. Green, "Silicon-based heterogeneous photonic integrated circuits for the mid-infrared," Opt. Mater. Express, vol. 3, 1523-1536 (2013).

33. L. B. Soldano and E. C. M. Pennings, “Optical multi-mode interference devices based on self-imaging: principles and applications,” Jour. of Lightwave Tech., vol. 13, no. 4, 615-625 (1995).
34. P.D. Trinh, S. Yegnanarayanan, and B. Jalali, “Integrated optical directional couplers in silicon-on-insulator,” Electronics Letters, vol. 31, no. 24, 2097-2098 (2007).
35. P. Dumon, G. Roelkens, W. Bogaerts, D. Van Thourhout, J. Wouters, S. Beckx, P. Jaenen, and R. Baets, “Basic photonic wire components in silicon-on-insulator,” 2nd IEEE International Conference on Group IV Photonics, 189-191 (2005).
36. D. J. Thomson, Y. Hu, G. T. Reed, and Jean-Marc Fedeli, “Low loss MMI couplers for high performance MZI modulators,” IEEE Phot. Tech. Letters, vol. 22, no. 20, 1485-1487 (2010).
37. W. Bogaerts, J. Brouckaert, D. Van Thourhout, and R. Baets, “Silicon-on-Insulator spectral filters fabricated with CMOS technology,” IEEE Jour. of Sel. Top. Quant. Elec., vol. 16, no. 1, 33-44 (2010).
38. M. A. Van Camp, S. Assefa, D. M. Gill, T. Barwicz, S. M. Shank, P. M. Rice, T. Topuria, and W. M. J. Green, “Demonstration of electrooptic modulation at 2165nm using a silicon Mach-Zehnder interferometer,” Opt. Express, vol. 20, no. 27, 28009-28016 (2012).
39. C. Reimer, M. Nedeljkovic, D. J. M. Stothard, M. O. S. Esnault, C. Reardon, L. O’Faolain, M. Dunn, G. Z. Mashanovich, and T. F. Krauss, “Mid-infrared photonic crystal waveguides in SOI,” Opt. Express, vol. 20, no. 28, 29361-29368 (2012).
40. G. T. Reed, G. Z. Mashanovich, F. Y. Gardes, and D. J. Thomson, “Silicon optical modulators,” Nature photonics, vol. 4, 518–526 (2010).
41. R. A. Soref and B. R. Bennett, “Electrooptical effects in silicon,” IEEE Jour. of. Quant. Elec., vol. 23, no. 1, 123-129 (1987).
42. B. J. Frey, D. B. Leviton, T. J. Madison, “Temperature-dependent refractive index of silicon and germanium,” Proc. Of SPIE, Orlando, USA (2006).
43. H. N. Rutt, S. Uppal and C. Y. Lee, “Ane electrically driven mid-infrared solid state modulator,” Joint 30th Intl. Conf. on Infrared and Millimeter Waves & 13th Intl. Conf. on Terahertz Electronics, TB3-5 (2005).

44. M. A. Richardson and J. A. Coath, “Infrared optical modulators for missile testing,” Optics & Laser Technology, vol. 30, 137-140 (1998).
45. Quantum Technology, Inc., www.quantumtech.com.
46. J. Teissier, S. Laurent, C. Manquest, C. Sirtori, A. Bousseksou, J. R. Coudevylle, R. Colombelli, G. Beaudoin, and I. Sagnes, “Electrical modulation of the complex refractive index in mid-infrared quantum cascade lasers,” Opt. Express, vo. 20, no. 2, 1172-1183 (2012).
47. R. Martini, C. Bethea, E Capasso, C. Gmachl, R. Paiella, E.A. Whittaker, H.Y. Hwang, D.L. Sivco, J.N. Baillargeon and A.Y. Cho, “Free-space optical transmission of multimedia satellite data streams using mid-infrared quantum cascade lasers,” Electronics Letters, vol. 38, no.4, 181-183 (2002).
48. W. M. J. Green, M. J. Rooks, L. Sekaric, and Y. A. Vlasov, “Ultra-compact, low RF power, 10Gb/s silicon Mach-Zehnder modulator,” Opt. Express, vol. 15, no. 25, 17106-17113 (2007).
49. S. Manipatruni, Q. Xu, B. Schmidt, J. Shakya and M. Lipson, “High speed carrier injection 18 Gb/s silicon micro-ring electro-optic modulator,” LEOS 2007, 537-538, Lake Buena Vista, Fl, USA (2007).
50. A. Liu, R. Jones, L. Liao, D. Samara-Rubio, D. Rubin, O. Cohen, R. Nicolaescu, and M. Paniccia, “A high-speed silicon optical modulator based on a metal–oxide–semiconductor capacitor,” Nature, 427, 615-618 (2004).
51. L. Liao, D. Samara-Rubio, M. Morse, A. Liu, D. Hodge, “High speed silicon Mach-Zehnder modulator,” Opt. Express, vol. 13, no. 8, 3129-3135 (2005).
52. F. Y. Gardes, G. T. Reed, and N. G. Emerson, “A sub-micron depletion-type photonic modulator in Silicon On Insulator,” Opt. Express, vol. 13, no. 22, 8845-8854 (2005).
53. A. Liu, L. Liao, D. Rubin, H. Nguyen, B. Ciftcioglu, Y. Chetrit, N. Izhaky, and M. Paniccia, “High-speed optical modulation based on carrier depletion in a silicon waveguide,” Opt. Express, vo. 15, no. 2, 660-668 (2007).
54. D. J. Thomson, F. Y. Gardes, J-M. Fedeli, S. Zlatanovic, Y. Hu, B. P. P. Kuo, E. Myslivets, N. Alic, S. Radic, G. Z. Mashanovich, and G. T. Reed, “50-Gb/s Silicon Optical Modulator,” IEEE Phot. Tech. Letters, vol. 24, no. 4, 234-236 (2012).
55. A. Densmore, S. Janz, R. Ma, J. H. Schmid, D-X. Xu, A. Delâge, J. Lapointe, M. Vachon, and P. Cheben, “Compact and low power thermo-optic switch using folded silicon waveguides,” Opt. Express, vol. 17, no. 13, 10457-10465 (2009).

56. X. Wang, J. A. Martinez, M. S. Nawrocka, and R. R. Panepucci, “Compact Thermally Tunable Silicon Wavelength Switch: Modeling and Characterization,” IEEE Phot. Tech. Letters, vol. 20, no. 11, 936-938 (2008).
57. H. C. Huang, S. Yee and M. Soma, “Quantum calculations of the change in refractive index due to free carriers in silicon with nonparabolic band structure,” J. Appl. Phys., vol. 67 no. 4, 2033-2039 (1990).
58. R. A. Smith, “Semicondutors”, Cambridge University Press, 294-300 (1978).
59. H. B. Briggs and R. C. Fletcher, “New infrared absorption bands in p-type germanium,” Phys. Rev., 76, 1130-1131 (1952).
60. W. Spitzer and H. Y. Fan, “Infrared absorption in n-type Silicon,” Phys. Rev., vol. 108, no. 2, 268-271 (1957).
61. S. J. Collocott and G.J. Troup, “Adaptation: numerical solution of the Kramers-Kronig transforms by trapezoidal summation as compared to a Fourier method,” Computer Physics Communications, 17, 393-395 (1979).

Chapter 3

1. Daylight Solutions, http://www.daylightsolutions.com/.
2. National Instruments LabView, http://www.ni.com/labview/.
3. Infrared Associates, Inc. , http://www.irassociates.com/.
4. IR Photonics, http://www.irphotonics.com/.
5. Thorlabs, http://www.thorlabs.de/.
6. Altechna, http://www.altechna.com/.

Chapter 4

1. R. A. Soref, S. J. Emelett, and W. R. Buchwald, “Silicon waveguided components for the long-wave infrared region,” J. Opt. A: Pure Appl. Opt 8, 840848 (2006).
2. G. T. Reed and A. P. Knights, “Silicon photonics: an introduction” Wiley, 2004.
3. Synopsys RSoft, http://optics.synopsys.com/rsoft/.
4. Photon Design Fimmwave, http://www.photond.com/products/fimmwave.htm.

5. P. Bienstman, S. Selleri, L. Rosa, H. P. Uranus, W. C. L. Hopman, R. Costa, A. Melloni, L. C. Andreani, J. P. Hugoni, P. Lalanne, D. Pinto, S. S. A. Obayya, M. Dems and K. Panajotov, “Modelling leaky photonic wires: A mode solver comparison,” Optical and Quantum Electronics, vol. 38, 731-759 (2006).
6. E. Dulkeith, F. Xia, L. Schares, W. Green, and Y. Vlasov, "Group index and group velocity dispersion in silicon-on-insulator photonic wires," Opt. Express, vol. 14, no. 9, 3853-3863 (2006).
7. F. Xia, M. Rooks, L. Sekaric, and Y. Vlasov, “Ultra-compact high order ring resonator filters using submicron silicon photonic wires for on-chip optical interconnects,” Opt. Express, vol. 15, no. 19, 11934-11941 (2007).
8. M. J. R. Heck, C. Hui-Wen; A. W. Fang, B. R. Koch, L. Di; P. Hyundai, M. N. Sysak and J. E. Bowers, "Hybrid Silicon Photonics for Optical Interconnects," IEEE Journal of Selected Topics in Quantum Electronics, vol.17, no.2, 333-346 (2011).
9. F. Gardes, G. Reed, N. Emerson, and C. Png, "A sub-micron depletion-type photonic modulator in Silicon On Insulator," Opt. Express, vol. 13, no. 22, 8845-8854 (2005).
10. S. Jungling and J. C. Chen, “A study and optimization of eigenmode calculations using the Imaginary Distance Beam-Propagation Method,” IEEE Journal of Quantum Electronics, vol. 30, no. 9, 2098-2105 (1994).
11. RSoft Beamprop manual.
12. A. S. Sudbo, “Film mode matching: a versatile numerical method for vector mode field calculations in dielectric waveguides,” Pure Appl. Opt., vol. 2, 211-233 (1993).
13. Photon Design Fimmwave manual.
14. Soitec, http://www.soitec.com.
15. Tanner EDA L-edit, http://www.tannereda.com/products/l-edit-pro.
16. GenISys BEAMER, http://genisys-gmbh.com/web/products/beamer.html.
17. A. M. Zheltikov, “Non λ-4 wavelength dependence of Rayleigh-scattering loss in waveguides,” Laser Physics, vol. 16, no. 6, 960-964 (2006).
18. E. Jaberansary, T. M. B. Masaud, M. M. Milosevic, M. Nedeljkovic, G. Z. Mashanovich, and H. M. H. Chong, “Scattering Loss Estimation Using 2-D Fourier Analysis and Modeling of Sidewall Roughness on Optical Waveguides,” IEEE Photonics Journal, vol. 5, no. 3, 6601010 (2013).
19. D-X. Xu, J. Schmid, G. T. Reed, G. Z. Mashanovich, D. J. Thomson, M. Nedeljkovic, X. Chen, D. Van Thourhout and S. Keyvaninia, “Silicon photonic integration platform –

Have we found the sweet spot?," Journal of Selected Topics in Quantum Electronics, vol. 24, no. 4 (2013).

20. M. Muneeb, X. Chen, P. Verheyen, G. Lepage, S. Pathak, E. Ryckeboer, A. Malik, B. Kuyken, M. Nedeljkovic, J. Van Campenhout, G. Mashanovich, and G. Roelkens, "Demonstration of Silicon-on-insulator mid-infrared spectrometers operating at 3.8μm," Opt. Express 21, no. 10, 11659-11669 (2013).
21. Y-C. Chang, V. Paeder, L. Hvozdara, J-M. Hartmann, and H. P. Herzig, "Low-loss germanium strip waveguides on silicon for the mid-infrared," Opt. Letters, vol. 37, no. 14, 2883-2885 (2012).
22. R. Loo, G. Wang, L. Souriau, J. C. Lin, S. Takeuchi, G. Brammertz, and M. Caymax, "High Quality Ge Virtual Substrates on Si Wafers with Standard STI Patterning," J. Electrochem. Soc., vol. 157, no. 1, H13-H21 (2010).
23. A. Malik, M. Muneeb, Y. Shimura, J. Van Campenhout, R. Loo and G. Roelkens, "Germanium-on-silicon mid-infrared waveguides and Mach-Zehnder interferometers," IEEE Photonics Conference 2013 (IPC), Seattle, US, MF 1.4 (2013).
24. A. Malik, M. Muneeb, S. Pathak, Y. Shimura, J. Van Campenhout, R. Loo, G. Roelkens, "Germanium-on-Silicon Mid-Infrared Arrayed Waveguide Grating Multiplexers," Photonics Technology Letters, vol.25, no.18, 1805-1808 (2013).

Chapter 5

1. M. M. Milošević, M. Nedeljkovic, T. M. Ben Masaud, E. Jaberansary, H. M. H. Chong, N. G. Emerson, G. T. Reed, and G. Z. Mashanovich, "Silicon waveguides and devices for the mid-infrared," Appl. Phys. Letters, 101, 121105 (2012).
2. Photon Design Fimmwave, http://www.photond.com/products/fimmwave.htm.
3. D. J. Thomson, Y. Hu, G. T. Reed, and Jean-Marc Fedeli, "Low loss MMI couplers for high performance MZI modulators," IEEE Phot. Tech. Letters, vol. 22, no. 20, 1485-1487 (2010).
4. W. Bogaerts, J. Brouckaert, D. Van Thourhout, and R. Baets, "Silicon-on-Insulator spectral filters fabricated with CMOS technology," IEEE Jour. of Sel. Top. Quant. Elec., vol. 16, no. 1, 33-44 (2010).

5. A. Densmore, S. Janz, R. Ma, J. H. Schmid, D-X. Xu, A. Delâge, J. Lapointe, M. Vachon, and P. Cheben, “Compact and low power thermo-optic switch using folded silicon waveguides,” Opt. Express, vol. 17, no. 13, 10457-10465 (2009).
6. A. Densmore, D. Xu, S. Janz, P. Waldron, T. Mischki, G. Lopinski, A. Delâge, J. Lapointe, P. Cheben, B. Lamontagne, and J. Schmid, "Spiral-path high-sensitivity silicon photonic wire molecular sensor with temperature-independent response," Opt. Lett., vol. 33, no. 6, 596-598 (2008).
7. M. Florjańczyk, P. Cheben, S. Janz, A. Scott, B. Solheim, and D-X. Xu, “Multiaperture planar waveguide spectrometer formed by arrayed Mach-Zehnder interferometers,” Opt. Express, vol. 15, no. 26, 18176-18189 (2007).

Chapter 6

1. E.D.Palik, “Handbook of optical constants of solids”, vol1, p.390, San Diego, Academic Press, (1997).
2. A. Densmore, S. Janz, R. Ma, J. H. Schmid, D-X. Xu, A. Delâge, J. Lapointe, M. Vachon, and P. Cheben, “Compact and low power thermo-optic switch using folded silicon waveguides,” Opt. Express, vol. 17, no. 13, 10457-10465 (2009).
3. G. T. Reed, “Silicon Photonics: The state of the art,” Wiley, 2008.
4. B. J. Frey, D. B. Leviton, T. J. Madison, “Temperature-dependent refractive index of silicon and germanium,” Proc. Of SPIE, Orlando, USA (2006).

Chapter 7

1. M.M. Pradhan, R.K. Garg, M. Arora, “Multiphonon infrared absorption in silicon,” Infrared Physics, vol. 27, no. 1, 25-30 (1987).
2. R. A. Soref and B. R. Bennett, “Electrooptical effects in silicon,” IEEE Jour. of. Quant. Elec., vol. 23, no. 1, 123-129 (1987).
3. P. A. Schumann and R. P. Phillips, “Comparisons of classical approximations to free carrier absorption in semiconductors,” Solid state electronics, vol. 10, 943-948 (1967).
4. S. Walles and S. Boija, “Transmittance of doped silicon between 40 and 100µm,” Jour. of Opt. Soc. Amer., vol. 54, 122-134 (1964).

5. M. Balkanski and J. M. Besson, “Optical properties of degenerate silicon,” Tech Note 2, Contract AF61(052)-789, Defense Tech. Inform. Cen., AD619581 (1965).
6. C. M. Randall and R. D. Rawcliffe, “Refractive indices of germanium, silicon and fused quartz in the far infrared,” Applied Optics, vol. 6, 1889 (1967).
7. W. Spitzer and H. Y. Fan, “Infrared absorption in n-type silicon,” Physical Review, vol. 108, no. 2, 268-271 (1957).
8. P. E. Schmid, “Optical absorption in heavily doped silicon,” Physical Review B, vol. 23, no.10, 5531-5536 (1981).
9. W. C. Dash and R. Newman, “Intrinsic optical absorption in single-crystal gemanium and silicon,” Physical Review, vol. 99, 1151-1155 (1955).
10. S. J. Collocott and G. K. Troup, “Adaptation: numerical soultion of the Kramers-Kronig transforms by trapezoidal summation as compared to a Fourier method,” Computer Physics Communications, vol. 17, 393-395 (1979).
11. S. K. Ray, T. N. Adam, R. T. Troeger, J. Kolodzey, G. Looney, and A. Rosen, “Characteristics of THz waves and carrier scattering in boron-doped epitaxial Si and $Si_{1-x}Ge_x$ films,” Jour. Appl. Phys., vol. 95, no. 10, 5301-5304 (2004).
12. D. Marris-Morini, X. Le-Roux, L. Vivien, E. Cassan, D. Pascal, M. Halbwax, S. Maine and S. Laval, “Optical modulation by carrier depletion in a silicon PIN diode,” Opt. Express, vo. 14, no.22, 10838-10843 (2006).
13. A. Cutolo, M. Iodice, P. Spirito and L. Zeni, “Silicon electro-optic modulator based on a three terminal device integrated in a low-loss single-mode SOI waveguide,” Jour. of Lightwave Tech., col. 15, no.3, 505-518 (1997).
14. C. Angulo Barrios, V. R. Almeida, R. Panepucci and M. Lipson, “Electrooptic modulation of submicrometer-size waveguide devices,” Jour. of Lightwave Tech., vol. 21, no.10, 2232-2239 (2003).
15. G. T. Reed, G. Z. Mashanovich, F. Y. Gardes, and D. J. Thomson, “Silicon optical modulators,” Nature photonics, vol. 4, 518–526 (2010).

Chapter 8

1. Y. C. Chang, P. Wagli, V. Paeder, A. Homsy, L. Hvozdar, P. van der Wal, J. Di Francesco, N. F. de Rooij, H. Peter Herzig, “Cocaine detection by a mid-infrared waveguide integrated with a microfluidic chip.” Lab Chip. Vol. 12, no. 17, 3020-3023 (2012).

2. M. Muneeb, X. Chen, P. Verheyen, G. Lepage, S. Pathak, E. Ryckeboer, A. Malik, B. Kuyken, M. Nedeljkovic, J. Van Campenhout, G. Z. Mashanovich, and G. Roelkens, “Demonstration of Silicon-on-insulator mid-infrared spectrometers operating at 3.8μm,” Opt. Express, vo. 21, no. 10, 11659-11669 (2013).
3. A. Malik, M. Muneeb, S. Pathak, Y. Shimura, J. Van Campenhout, R. Loo, G. Roelkens, "Germanium-on-Silicon Mid-Infrared Arrayed Waveguide Grating Multiplexers," Photonics Technology Letters, vol.25, no.18, 1805-1808 (2013).
4. Y-C. Chang, V. Paeder, L. Hvozdara, J-M. Hartmann, and H. P. Herzig, “Low-loss germanium strip waveguides on silicon for the mid-infrared,” Opt. Letters, vol. 37, no. 14, 2883-2885 (2012).
5. W. Bogaerts, J. Brouckaert, D. Van Thourhout, and R. Baets, “Silicon-on-Insulator spectral filters fabricated with CMOS technology,” IEEE Jour. of Sel. Top. Quant. Elec., vol. 16, no. 1, 33-44 (2010).
6. A. Densmore, D. Xu, S. Janz, P. Waldron, T. Mischki, G. Lopinski, A. Delâge, J. Lapointe, P. Cheben, B. Lamontagne, and J. Schmid, "Spiral-path high-sensitivity silicon photonic wire molecular sensor with temperature-independent response," Opt. Lett., vol. 33, no. 6, 596-598 (2008).
7. A. Densmore, S. Janz, R. Ma, J. H. Schmid, D-X. Xu, A. Delâge, J. Lapointe, M. Vachon, and P. Cheben, “Compact and low power thermo-optic switch using folded silicon waveguides,” Opt. Express, vol. 17, no. 13, 10457-10465 (2009).
8. R. A. Soref and B. R. Bennett, “Electrooptical effects in silicon,” IEEE Jour. of. Quant. Elec., vol. 23, no. 1, 123-129 (1987).